Mon. Not. R. Astron. Soc. **355,** 641–681 (2004) doi:10.1111/j.1365-2966.2004.08368.x

Infrared mergers and infrared quasi-stellar objects with galactic winds – II. NGC 5514: two extranuclear starbursts with LINER properties and a supergiant bubble in the rupture phase

S. Lípari,[1]★† E. Mediavilla,[2] B. Garcia-Lorenzo,[2]† R. J. Díaz,[1] J. Acosta-Pulido,[2] M. P. Agüero,[1] Y. Taniguchi,[3] H. Dottori[4] and R. Terlevich[5,6]

[1]*Córdoba Observatory and CONICET, Laprida 854, 5000 Córdoba, Argentina*
[2]*Instituto de Astrofísica de Canarias, 38205 La Laguna, Tenerife, Canary Islands, Spain*
[3]*Astronomical Institute, Tohoku University, Aoba, Senday 980-8578, Japan*
[4]*Instituto de Fisica, Univ. Fed. Rio Grande do Sul, CP 15051, Porto Alegre, Brazil*
[5]*Institute of Astronomy, Madingley Road, Cambridge CB3 0HA*
[6]*Instituto Nacional de Astrofísica, Óptica y Electrónica (INAOE), Puebla, Mexico*

Accepted 2004 August 31. Received 2004 August 26; in original form 2004 April 25

ABSTRACT

A study of the morphology, kinematics and ionization structure of the infrared (IR) merger NGC 5514 is presented. This study is based mainly on INTEGRAL two-dimensional (2D) spectroscopy (obtained at the 4.2-m William Herschel Telescope, WHT), plus optical and near-IR images. Clear evidence of two extranuclear starbursts with young outflows (OFs) and low-ionization nuclear emission region (LINER) activity are reported. One of these OFs has generated a supergiant bubble and the other is associated with an extended complex of H II regions.

In the galactic bubble it was found that: (i) the [S II], Hα, [N II], [O I] and [O III] emission-line maps show a bubble with a distorted ellipsoidal shape, with major and minor axes of ∼6.5 kpc [13.6 arcsec; at position angle (PA) = 120° ± 10°] and ∼4.5 kpc (9.6 arcsec); (ii) these maps depict four main knots, a very strong one and three others more compact and located at the border; (iii) the centre of the bubble is located at ∼4.1 kpc (8.5 arcsec) to the west of the main nucleus; (iv) the WHT spectra show, in this area, two strong components: blue and red emission-line systems, probably associated with emission from the near and far side of the external shell, for which the mean OF velocities were measured as $V_{\rm OF\,blue}$ = (−320 ± 20) km s^{-1} and $V_{\rm OF\,red}$ = (+265 ± 25) km s^{-1}; (v) these two components depict LINER properties, probably associated with large-scale OF + shocks; (vi) at the east border, the kinematics of the ionized gas and the [S II] emission-line maps show an extended ejection of 4 kpc aligned with the PA of the major axis; (vii) three other ejections were found, two of them perpendicular to the extended one. Each ejection starts in one of the knots. These results suggest that the bubble is in the rupture phase.

For the complex of giant H II regions it was found that: (i) the Hα, [N II] and [S II] emission-line maps show a compact strong emission area (peaking at ∼810 pc ∼1.7 arcsec, to the east of the second nucleus) and faint extended emission with an elongated shape, and major and minor axes of ∼5.1 kpc (10.8 arcsec; at PA ∼20°) and ∼2.9 kpc (6.0 arcsec); (ii) inside this complex, the spectra show H II region and transition LINER/H II characteristics; (iii) at the border of this extended H II area the spectra have outflow components and LINER properties.

INTEGRAL 2D [N II], Hα, [S II] and [O III] velocity fields (VFs) are presented. These VF maps show results consistent with an expansion of the bubble, plus four ejections of ionized gas. The U, B, V, I, J, H and K_S images show a pre-merger morphology, from which faint filaments

★E-mail: lipari@mail.oac.uncor.edu
†Visiting astronomer at La Palma, CASLEO and CTIO Observatories.

of emission emerge, centred on the bubble. The ionization structure and the physical conditions were analysed using the following 2D emission-line ratio and width maps: [S II]/Hα, [N II]/Hα, [O I]/Hα, [O III]/Hβ and FWHM–[N II]. In the region of the bubble, 100 per cent of the [N II]/Hα and [S II]/Hα ratios show very high values (>0.8) consistent with LINER processes associated with high-velocity shocks. These new results support the previous proposition that extreme nuclear and 'extranuclear' starbursts with galactic winds + shocks play an important role in the evolution of IR mergers/quasi-stellar objects.

Key words: ISM: bubbles – galaxies: individual: NGC 5514 – galaxies: interactions – galaxies: kinematics and dynamics – quasars: general – galaxies: starburst.

1 INTRODUCTION

A current key issue in astrophysics is to explore the evolution of the star formation process, especially at high redshift, when the galaxies/quasi-stellar objects (QSOs) formed, and where it is expected that the star formation rate is very high. An important step, in order to improve our understanding of this issue, is to study extreme star formation and associated galactic wind processes in nearby galaxies, since we can obtain more detailed and unambiguous data (Lípari et al. 2003, 2004a; Taniguchi et al., in preparation). Mainly for this purpose we have conducted a study of infrared (IR) mergers and IR QSOs with galactic winds (Lípari, Colina & Macchetto 1994; Lípari 1994; Lípari et al. 2000, 2003, 2004a); these IR systems are excellent laboratories at low redshift for the study of extreme star formation and galactic wind processes.

1.1 IR mergers and IR QSOs

One of the most exciting populations of objects identified over the last two decades is the group of IR-bright galaxies, which emit most of their energy in the IR ($L_{\rm IR[8-1000\ \mu m]}/L_B \sim 5$ –300; Rieke et al. 1980; Soifer et al. 1984). In particular, luminous and ultraluminous IR galaxies (LIRGs: $L_{\rm IR} \geqslant 10^{11}$ L$_\odot$ and ULIRGs: $L_{\rm IR} \geqslant 10^{12}$ L$_\odot$, respectively) are dusty, strong IR emitters where frequently a strong enhancement of star formation is taking place (for references see Lípari et al. 2003, 2004a). In addition, imaging surveys of LIRGs and ULIRGs show that a very high proportion (∼70–95 per cent) are mergers or interacting systems (Joseph & Wright 1985; Rieke et al. 1985; Sanders et al. 1988a; Melnick & Mirabel 1990; Clements et al. 1996). These IR galaxies also contain large amounts of centrally concentrated molecular gas (Sanders, Scoville & Soifer 1991; Scoville et al. 1991). There is observational evidence and theoretical work suggesting that in IR mergers/QSOs tidal torque and loss of angular momentum drive large amounts of interstellar gas into the central regions, leading to *extreme starburst processes* and probably fuelling a supermassive black hole (see Joseph & Wright 1985; Rieke et al. 1985; Heckman, Armus & Miley 1987, 1990; Sanders et al. 1988a,b; Scoville & Soifer 1991; Barnes & Hernquist 1992, 1996; Mihos & Hernquist 1994a,b, 1996; Taniguchi & Wada 1996; Canalizo & Stockton 2001).

At the highest IR luminosities, the presence of active galactic nuclei (AGN) in LIRGs becomes important, and LIRGs probably represent an important stage in the formation of QSOs and elliptical galaxies. In particular, several possible links among mergers, starbursts, ellipticals and QSOs have been proposed (e.g. Joseph & Wright 1985; Sanders et al. 1988a; Lípari 1994). The discovery and study of IR QSOs (see Lípari et al. 2003, 2004a; Zheng et al. 2002) raises several interesting questions, in particular whether they are a special class of QSOs. We found, or confirmed, that a high percentage of IR QSOs show extreme galactic winds with giant galactic arcs, merger features, broad absorption line (BAL) systems, and extreme Fe II emission, and are radio quiet (Lípari, Macchetto & Golombeck 1991a; Lípari, Terlevich & Macchetto 1993; Lípari et al. 2003, 2004a). We suggested that these objects could be young IR-active galaxies at the end phase of a strong starburst, i.e. composite and transition QSOs.

1.2 Galactic winds and galactic bubbles

Galactic winds (GWs) and outflows (OF) have been detected mainly in starburst and Seyfert galaxies (see Heckman et al. 1990, 2000; Veilleux et al. 2002a; Veilleux, Kim & Sanders 2002b). IR mergers/QSOs often show strong and extreme starbursts, with very powerful galactic winds (Lípari et al. 2003, 2004a). In addition, galactic shells, arcs and bubbles generated by multiple supernova (SN) explosions and massive star winds have been found in the Milky Way, the Magellanic Clouds, M31, M33 and other nearby galaxies. However, there are few examples of GWs associated with extreme starbursts detected in their early phases, i.e. in the 'supergiant' galactic bubble stage. Furthermore, mainly broken supergiant bubbles/shells in the blowout or post-blowout (free wind) phases have been detected, e.g. from the nuclei of NGC 3079, Arp 220, Mrk 231, IRAS 19254–7245, NGC 2623, NGC 2782, etc. (Hodge & Kennicutt 1983; Hummel, van Gorkom & Kotanyi 1983; Ford et al. 1986; Heckman et al. 1987; Duric & Seaquist 1988; Heckman et al. 1990; Lípari et al. 1994, 2003, 2004a; Jogee, Kenney & Smith 1998, and others), from the extranuclear regions of NGC 6946, NGC 1620, etc. (Hodge 1967; Vader & Chaboyer 1995; Efremov et al. 2002, etc.), and also from both the nucleus and extranuclear areas of M82 (Lynds & Sandage 1963; Axon & Taylor 1978; Bland & Tully 1988; Wills et al. 1999; Garcia-Burillo et al. 2001). Thus, young extreme GWs with supergiant galactic bubbles (even in the blowout phase) are difficult to detect because of their short time-scale of $\leqslant 10^7$ yr (Suchkov et al. 1994).

Our understanding of the main phases of galactic winds associated with starbursts was improved significantly by the use of theoretical and numerical models (see Tomisaka & Ikeuchi 1988; Mac Low, McCray & Norman 1989; Suchkov et al. 1994; Strickland & Stevens 2000). In general, good agreement has been found between these models and the observations (Lípari et al. 2004a). Theory suggests four main stages for GWs associated with starbursts, following the reviews presented by Heckman et al. (1990) and Lehnert & Heckman (1995, 1996):

(i) *Phase I.* A GW results when the kinetic energy of the ejecta supplied by multiple supernovae and winds from massive stars is

high enough to excavate a cavity in the centre of a starburst. At this point the kinetic energy is converted into thermal energy. This conversion means that the collision of intersecting SN/stellar winds transforms the kinetic energy of the ejecta into thermal energy via *shocks*. In this cavity the host fluid (10^8 K) has a sound speed much greater than that of the local escape velocity and a pressure much higher than the interstellar medium (ISM) and thus will expand as a *galactic bubble*.

(ii) *Phase II.* As the bubble expands and sweeps up the ambient gas, it will enter the 'radiative phase' (Castor, McCray & Weaver 1975). The bubble will then collapse, due to radiative cooling, into a *thin shell*.

At this phase there are different radial components in the GW: (1) the inner starburst region where the energy is injected and thermalized; (2) a region of supersonic wind; (3) a hot region ($T \sim 10^8$ K) where the wind gas has been decelerated and heated by internal shocks; and (4) the thin shell, which is the source of optical emission lines (with velocities of several hundred km s^{-1}).

(iii) *Phase III.* After the shell has formed its evolution is strongly dependent on the input physics. If the cooling rate in the interior is high, then the expanding bubble can stop expanding (Tomisaka & Ikeuchi 1988).

(iv) *Phase IV.* If other probable dynamical and thermal conditions are considered (e.g. Suchkov et al. 1994; Mac Low et al. 1989), the shell can *break up*. After this break-up, the host interior become a freely expanding wind, and the bubble then *blows out*. In the blowout phase the optical emission comes from obstacles, such as clouds and shell fragments, which are immersed and shock-heated by the OF. In addition, in this phase of free expansion, the velocity, pressure, temperature and density of the wind are a function of the radius.

On the other hand, for galactic winds associated with AGN the situation is less clear, and very different models are proposed in order to explain the observed data. In these models the OF could be generated by jet-driven thermal winds, accretion disc winds, X-ray-heated torus winds, etc. (see Veilleux et al. 2002a; Morganti et al. 2003).

In addition, it is important to note that in recent years the development of new technology has allowed the study of GWs and outflow processes for almost all the main components of the ISM, including ionized warm gas, hot gas (10^7 K), cold neutral H I, molecular gas and dust (e.g. Heckman et al. 1996; Alton, Davies & Bianchi 1999; Wills et al. 1999; Heckman et al. 2000; Lípari et al. 2000, 2003, 2004a; Oosterloo et al. 2000; Seaquist & Clark 2001; Morganti et al. 2003).

2 THE PROGRAMME AND OBSERVATIONS

2.1 The programme

To improve our understanding of the formation and evolution of galaxies, it is necessary to study: (i) objects with strong star formation and galactic wind processes at low redshift (Lípari et al. 1994, 2000, 2003, 2004a); (ii) well-defined samples of star-forming + GW galaxies at high redshift and then investigate their nature (e.g. Taniguchi & Shioya 2000; Ajiki et al. 2002, 2003; Taniguchi et al. 2003). With these aims in mind we began an international project to study nearby star-forming + GW galaxies and distant Lyα emitters (see Ajiki et al. 2002, 2003; Taniguchi et al. 2003; Lípari et al. 2004a,b,c).

In the present paper we show new results from the study of the morphology, kinematics and ionization structure of 'nearby' IR mergers/QSOs with galactic winds. This study is based mainly on two-dimensional spectroscopy, obtained at the European Northern Observatory (ENO, La Palma, Spain), the European Southern Observatory (ESO, Chile), the Complejo Astronomico El Leoncito (CASLEO, Argentina), and Bosque Alegre (BALEGRE, Argentina) observatories, with the 4.2-m, 3.6-m, 2.15-m and 1.5-m telescopes, respectively. The characteristics and goals of the programme have been described in detail by Lípari et al. (2004a). The first ∼10 objects, observed with 2D spectroscopy, include nearby IR systems selected from our previous surveys and from the literature. Our original data base of IR mergers/QSOs with outflow and candidates contains a total of 43 objects (see table 1 of Lípari et al. 2004a).

The main goal of this programme (at low redshift) is to analyse in detail the properties of the different stages of extreme starbursts, galactic winds, mergers, QSOs and elliptical galaxies (and their interrelation). NGC 5514 is one of the 10 nearby IR systems of our first 2D spectroscopic study (and it was also included in the data base of 43 IR mergers/QSOs with outflow; Lípari et al. 2004a). This object was originally selected from the Survey of Warm *IRAS* Galaxy Candidates (Lípari, Bonatto & Pastoriza 1991b; Lípari et al. 1991a; Lípari & Macchetto 1992a,b). This Survey is based on observations of AGN/QSOs and starburst candidates, from the Catalogue of Warm *IRAS* Sources (de Grijp et al. 1987). In this pre-merger system (NGC 5514) we found two strong 'extranuclear' starbursts, with two associated early outflows. This object therefore gives important clues about the early phases of the processes that we enumerated as the main goals of this programme at low redshift. Furthermore, NGC 5514 shows two new examples of young GWs with low-ionization nuclear emission region (LINER) properties, and probably the first GW observed in the 'pre-blowout phase' of a supergiant extranuclear galactic bubble. We note that this OF structure shows properties similar to those observed in the supergiant galactic bubble of NGC 3079. In NGC 5515, however, this OF bubble is located far from the nuclear region (and hence far from a possible AGN) and is just in the rupture process.

NGC 5514 (UGC 9102, IRAS 14111+0753, de Grijp et al. Catalogue N–342) is a nearby IR galaxy at $z_{\rm sys} = 0.024\,527$, which is the result of a merger probably between two disc galaxies of unequal mass ($M_1/M_2 \sim 2$; Fried & Lutz 1988, hereafter FL88). This system shows two compact nuclei, and a bright tidal tail (see Section 3.1). The total IR luminosity of NGC 5514 is $L_{\rm IR[8-1000\,\mu m]} \sim 0.5 \times 10^{11}$ L$_\odot$. Throughout this paper, a Hubble constant of $H_0 = 75$ km s^{-1} Mpc^{-1} will be assumed. For NGC 5514 a distance of ∼98.1 Mpc ($cz_{\rm sys} = 7358 \pm 25$ km s^{-1}; Section 3.5) was adopted, and thus the angular scale is 1 arcsec ≈476 pc.

2.2 WHT + INTEGRAL 2D spectroscopy

In general, the observations were obtained at ENO, CASLEO and CTIO with the 4.2-m, 2.15-m and 1.0-m telescopes, respectively. Two-dimensional (2D) optical spectroscopy of NGC 5514 was obtained during two photometric nights in 2001 April at the 4.2-m William Herschel Telescope (WHT) at the Roque de los Muchachos Observatory on the island of La Palma, Spain (Table 1). The WHT was used with the INTEGRAL fibre system (Arribas et al. 1998) and the WYFFOS spectrograph (Bingham et al. 1994). The seeing was typically 1.0 arcsec.

INTEGRAL links the $f/11$ Nasmyth focus of the WHT with the slit of WYFFOS via three optical fibre bundles. A detailed technical description of INTEGRAL is provided by Arribas et al. (1998); here we recall only its main characteristics. The three bundles have different spatial configurations on the focal plane and can be

Table 1. Journal of observations.

Date	Telescope/ instrument	Type	Spectral region	Exposure time seconds	Comments
1989 Jun 29	2.15-m CASLEO/Z-machine	Aperture Sp	λλ4700–7200	1500×3	Aperture: 3 × 6 arcsec^2
1990 March 9	1.0-m CTIO/2D FRUTTI	Long-slit Sp	λλ3600–7000	1800×3	PA 90° slit width = 1.5 arcsec
1993 Jul 13	2.15-m CASLEO/UCS	Long-slit Sp	λλ6500–7000	1800×2	PA 90° slit width = 2.0 arcsec
1997 Mar 12	2.15-m CASLEO/CCD Cam	Images	*B*	240×2	Seeing ∼2.0 arcsec (FWHM)
1997 Mar 12	2.15-m CASLEO/CCD Cam	Images	*V*	300×2	Seeing ∼2.0 arcsec (FWHM)
1997 Mar 12	2.15-m CASLEO/CCD Cam	Images	*I*	300×2	Seeing ∼2.0 arcsec (FWHM)
1997 Mar 13	2.15-m CASLEO/UCS	Long-slit Sp	λλ4000–7500	1800×2	PA 90° slit width = 2.5 arcsec
2000 May 11	2.15-m CASLEO/CCD Cam	Images	*U*	180×2	Seeing ∼1.7 arcsec (FWHM)
2000 May 11	2.15-m CASLEO/CCD Cam	Images	*I*	180×2	Seeing ∼1.7 arcsec (FWHM)
2000 May 25	2.15-m CASLEO/UCS	Long-slit Sp	λλ6100–7200	2700×2	PA 90° slit width = 2.0 arcsec
2000 May 25	2.15-m CASLEO/UCS	Long-slit Sp	λλ4700–5800	2700×2	PA 90° slit width = 2.0 arcsec
2000 May 26	2.15-m CASLEO/UCS	Long-slit Sp	λλ3800–7300	1800×2	PA 90° slit width = 1.5 arcsec
2001 Apr 11	4.2-m WHT/INTEGRAL	2D Spect.	λλ6000–7400	1800×3	Position 1 (centred in the bubble)
2001 Apr 11	4.2-m WHT/INTEGRAL	2D Spect.	λλ6000–7400	1800×3	Position 2 (centred in the nuclei area)
2001 Apr 12	4.2-m WHT/INTEGRAL	2D Spect.	λλ6000–7400	1500×3	Position 3 (centred in the H II complex)
2001 Apr 12	4.2-m WHT/INTEGRAL	2D Spect.	λλ4500–5900	1800×3	Position 3
2001 Apr 12	4.2-m WHT/INTEGRAL	2D Spect.	λλ4500–5900	1800×3	Position 1

interchanged depending on the scientific programme. At the focal plane the fibres of each bundle are arranged in two groups, one forming a rectangle and the other an outer ring (for collecting background light, in the case of small objects).

The data analysed in this paper were obtained with the standard bundle 2 of 219 fibres, each 0.9 arcsec in diameter projected on the sky. The central rectangle is formed by 189 fibres, covering a field of view of 16.4 × 12.3 arcsec^2; and the other 30 fibres form a ring 90 arcsec in diameter.

The WYFOS spectrograph was equipped with two gratings of 1200 line mm^{-1}, covering the λλ6000–7400 and λλ4500–5900 ranges. A TEK CCD array of 1124 × 1124 pixel of 24-μm side was used, giving a linear dispersion of about ∼1.4 Å pixel^{-1} (∼2.8 Å effective resolution, ∼100 km s^{-1}). Using the red grating, three different positions of the central region of this merger were observed (called positions 1, 2 and 3; see Section 3.2 and Table 1) in order to obtain large spatial coverage. These three observed regions were overlapped, forming a mosaic and covering a total area of approximately 30 × 20 arcsec^2. We note that the main nucleus of the merger was observed in all the positions, in order to perform a simple overlapping process. Positions 1 and 3 were also observed using the blue grating.

It is important to note that for this mosaic of 2D observations, our aim was to cover the three main central regions of the merger: two extranuclear areas with strong optical emission lines and the nuclear area (for details see Sections 3.2 and 3.3). Thus, in the present work (using INTEGRAL 2D spectroscopy), our aim was not to cover the entire main body of NGC 5514.

2.3 CASLEO long-slit + aperture spectroscopy and broad-band images

Spectrophotometric observations and images of NGC 5514 were taken at CASLEO (San Juan, Argentina) with the 2.15-m Ritchey–Chrétien telescope. Optical long-slit + aperture spectroscopy and broad-band CCD imaging observations were obtained during seven photometric nights in 1989 June, 1993 July, 1997 March and 2000 May (see Table 1). Long-slit spectroscopic observations with medium and high resolution were obtained with the University of Columbia spectrograph (UCS; e.g. Lípari, Tsvetanov & Macchetto 1997). The medium-resolution spectra were made using a 600 line mm^{-1} grating, a slit width of 2.5 arcsec, which gives an effective resolution of ∼6 Å (∼290 km s^{-1}), and a dispersion of 120 Å mm^{-1}, covering the wavelength range λλ4000–7500. The high-resolution spectra were made using a 1200 line mm^{-1} grating, and a slit width of 2.0 arcsec, which gives an effective resolution of ∼1.5 Å (∼50 km s^{-1}) covering the wavelength ranges λλ4700–5800 and 6100–7200. Aperture spectroscopic data were obtained with the 'Z-machine' (e.g. Lípari et al. 1991a,b). These aperture spectra were made using a 600 line mm^{-1} grating, giving a dispersion of 130 Å mm^{-1} and an effective resolution of ∼8 Å (∼300 km s^{-1}) covering the wavelength range λλ4700–7200. *U*, *B*, *V* and *I* images were obtained. A TEK 1K chip with a scale of 1.01 arcsec pixel^{-1} was used. The seeing was in the range 1.5–2.5 arcsec (FWHM).

2.4 CTIO long-slit spectroscopy

Spectrophotometric observations were taken at the Cerro Tololo Inter-American Observatory (CTIO, Chile) with the two-dimensional photon-counting detector (2D FRUTTI) attached to the Cassegrain focus of the 1.0-m telescope. The observations were obtained during one photometric night in 1990 March (see Table 1). The medium-resolution long-slit spectra were taken with a slit width of 1.5 arcsec. The wavelength range was λλ3600–7000. From a comparison lamp and sky lines an effective resolution of ∼6–7 Å (∼300 km s^{-1}) was estimated. The seeing was in the range 1.3–1.8 arcsec (FWHM).

2.5 NED archive data

From the NASA Extragalactic Data Base (NED, California Institute of Technology) we obtained a copy of a Palomar 48-inch Schmidt

telescope image of NGC 5514. This deep photographic image was observed using a plate 103a-O (broad-band ∼B).

In addition, at NED and from the Two-Micron All-Sky Survey (2MASS; Jarret et al. 2000) near-IR images J (1.2 μm), H (1.6 μm) and K_S (2.2 μm) were obtained. These images were observed using the 2MASS dedicated 1.3-m telescope, giving an angular resolution of ∼2 arcsec.

The California Institute of Technology gave us authorization to use and show these NED archive public domain data.

2.6 Reduction

The IRAF[1] software packages were used to reduce and analyse the data (obtained at the ENO-ORM, CASLEO and CTIO). The long-slit spectra and broad-band images – obtained at CASLEO and CTIO – were reduced in the standard way. Bias and dark-subtraction and flat-fielding were performed. Wavelength calibration of the long-slit spectra was done by fitting two-dimensional polynomials to the positions of lines in the arc frame. The spectra were corrected for atmospheric extinction, galactic reddening and redshift. The images and the long-slit spectra were flux-calibrated using observations of standard stars from the samples of Stone & Baldwin (1983), Oke (1990) and Landolt (1992).

The reduction of the 2D spectroscopic observations consists of two mains steps: (i) reduction of the spectra for each of the 219 fibres, and (ii) the generation of 2D maps by interpolating the selected parameter (e.g. emission-line intensity, continuum intensity, radial velocity, etc.) from the grid values defined by the fibre bundle. Step (i) was basically done in the same way as for long-slit spectroscopy, including bias subtraction, aperture definition and trace, stray-light subtraction, the extraction of the spectra, wavelength calibration, throughput correction and cosmic-ray rejection. We obtained typical wavelength calibration errors of 0.1 Å, which give velocity uncertainties of 5 km s^{-1}. For step (ii) the INTEGRAL[2] software package was used with 2D interpolation routines. In particular, ASCII files, with the positions of the fibres and the corresponding spectral features, were transformed into regularly spaced standard FITS files.

To generate two-dimensional maps of any spectral feature (intensity, velocity, width, etc.) the INT-MAP script of the INTEGRAL reduction package and the IDA tool (Garcia-Lorenzo, Acosta-Pulido & Mejias-Fernandez 2002) were used. We have found that the IDA package gets better results recovering 2D maps from low signal-to-noise data. The IDA interpolation is performed using the IDL standard routine TRIGRID, which uses a method of bivariate interpolation and smooth surface fitting for irregularly distributed data points (Akima 1978). Maps generated in this way are presented in the following sections.

The emission-line components were measured and decomposed using Gaussian profiles by means of a non-linear least-squares algorithm described in Bevington (1969). In particular, we used the software SPECFIT,[3] and SPLOT from the STSDAS,[4] and IRAF packages, respectively. An example of SPECFIT deblending, using three components for each emission line in IRAS 01003−2238, was shown in fig. 2 of Lípari et al. (2003). We note that in each WHT spectrum the presence of OF components and multiple emission-line systems were confirmed by detecting these systems in at least two or three different emission lines ([N II] λ6583, Hα, [N II] λ6548, [S II] λλ6717+31, [O I] λ6300, [O III] λ5007 and Hβ). For the study of the kinematics, the ADHOC[5] software package was also used.

[1] IRAF is a reduction and analysis software facility developed by NOAO.

[2] INTEGRAL is an imaging and spectroscopic analysis software facility developed by the Instituto de Astrofísica de Canarias (IAC).

[3] SPECFIT was developed and is kindly provided by Gerard A. Kriss.

[4] STSDAS is the reduction and analysis software facility developed by the Space Telescope Science Institute.

3 RESULTS

This section focuses on presenting (i) optical and near-IR images of NGC 5514; (ii) 2D spectroscopic evidence for two extranuclear starbursts with OFs and LINER activity; (iii) a supergiant galactic bubble generated by one of these starbursts, and an extended complex of H II regions associated with the other extranuclear star formation area; and (iv) detailed studies of the 2D kinematics and ionized structure.

3.1 The broad-band morphology of NGC 5514 (optical and near-IR images)

The CASLEO optical V image (Fig. 1) shows the whole merger. This system consists of a main body with a radius $r \sim 35$ arcsec (∼17 kpc), a bright tidal tail with a projected extension of ∼104.8 arcsec (∼50 kpc) located to the east of the main body and a very faint second tail of ∼114.4 arcsec (∼55 kpc) to the west. We note that both tidal tails depict a clear or relatively strong continuum emission mainly in the V and B images.

For the main body, optical and near-IR contour images (in U, B, V, I, J, H and K_S; Figs 2 and 3) show the following main structures (at a resolution of ∼1.5–2.0 arcsec; FWHM): a main nucleus which is bright in all the observed optical and near-IR broad-band images, plus a second nucleus to the south-east of the main nucleus and at a distance of ∼ 5.4 kpc (∼11.7 arcsec), which is bright in U, I, and in the near-IR bands. In general, these optical and near-IR images depict the typical features of a pre-merger system.

In addition, several interesting and unusual features were also detected in these images. The following were of particular note:

(i) The Palomar deep 103a-O image (broad-band B; Fig. 4) shows several faint 'radial' filaments in the outer regions. More specifically, on the north-west side of the main body at least three radial filaments were found, each one with an extension of 5.8 arcsec (∼2.8 kpc; Fig. 4). Similar types of filaments in emission (and/or in absorption) were detected in the OF external regions of NGC 3256, NGC 2623, M82, NGC 3079 and other galaxies (e.g. Lípari et al. 2000, 2004a; Cecil et al. 2001).

(ii) An interesting feature was found in the $(B - I)$ colour image. Fig. 5 shows one or two very extended bands through almost the entire main body of the merger. These bands depict strong emission in V and B images.

Since these two bands or structures show similar photometric properties as the tidal tails, and they are aligned with the bright east tail, a simple explanation, for these structures, is that they are the beginning of the east tidal tail, which probably emerges from the distorted spiral disc of the main galaxy that collided. Thus, the total projected extension of the east tails is ∼175 arcsec (∼83 kpc).

A second explanation for these structures is that they are associated with the presence of a very extended disc or ring of dust around the main nucleus. This type of structure has been detected in several spiral galaxies (e.g. Feinstein et al. 1990).

[5] ADHOC is a 2D/3D kinematics analysis software package developed by Marseille Observatory.

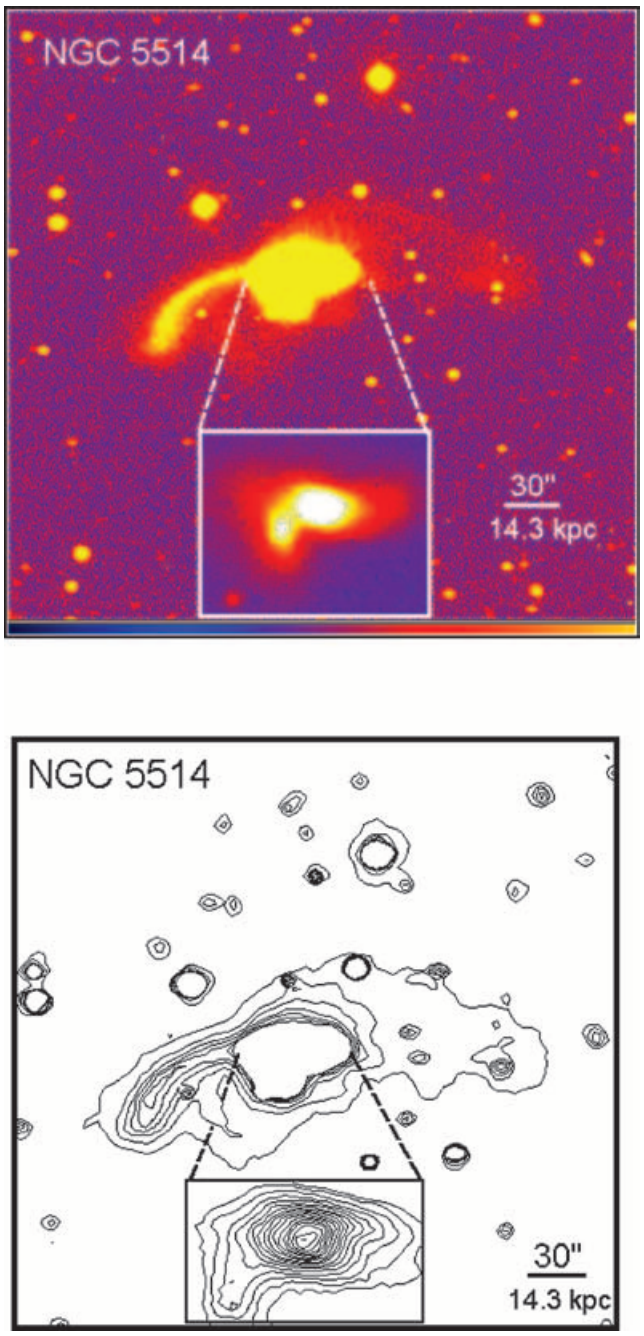

Figure 1. CASLEO *V* image and contour of the whole IR pre-merger NGC 5514. North is to the top, east is to the left.

(iii) In addition, the *V* and *B* broad-band images show for the second nucleus very weak continuum emission. However, in the *U*, *I* and near-IR bands this nucleus depicts a bright and compact shape (Figs 2 and 3). A simple explanation for these observed properties is that they could be due to the absorption of the emission in the beginning of the tidal tail or in the possible ring/disc of dust.

(iv) An interesting structure in the bright eastern tail is a faint filament extending at right angles, to the south (already detected by FL88, in their *B* image: fig. 2a). It is not easy to find a simple explanation for this structure.

The main galaxy shows the major photometric axis aligned approximately with the east–west direction. This galaxy, in the broad-bands *I* and *H*, shows a projected diameter $d \sim 50$ arcsec ($\sim$24 kpc). The position of the near-IR photometric major axis was analysed in detail by fitting ellipses to the 2MASS *H* image. We found the following position angle (PA) for the photometric major axis: $\mathrm{PA}_H = 80^\circ \pm 7^\circ$ for $2 \leqslant r \leqslant 6$ kpc. This radial range of radius corresponds to the regions where the major-axis PAs show relatively constant values. Variations of the photometric major-axis PA in the nuclear and circumnuclear regions (for $r \leqslant 2$ kpc) were detected, which could be due mainly to the presence of dust and blue structures.

A second detailed study of the *H* luminosity profile was performed for the northern galaxy. We fitted ellipses 1 pixel (1.0 arcsec) wide, and the surface brightness along the ellipse major axis at each radius was extracted. The obtained profile then corresponds to the surface brightness across the photometric major axis. A good fit of the *H* surface brightness with the $r^{1/4}$ law was obtained in the radial range $1 \leqslant r \leqslant 12$ kpc (see Fig. 6a). If we combine the $r^{1/4}$ and an exponential law, a small improvement of the fit is obtained. Therefore, for the main galaxy of NGC 5514, the near-IR (*H* band) photometric profile corresponds mainly to a bulge-dominant disc system; i.e. Sa or Sb galaxy.

The projected diameter of the south-east galaxy is $d \sim 30$ arcsec ($\sim$15 kpc), in the *I* and *H* broad-bands. A similar study to that performed for the main galaxy was carried out for the south-eastern galaxy. We found for the near-IR photometric major axis (fitting ellipses to the *H* image) a $\mathrm{PA}_H = 11^\circ \pm 8^\circ$ for $2 \leqslant r \leqslant 4$ kpc. A good fit of the *H* surface brightness with the $r^{1/4}$ law was obtained in the radial range $1 \leqslant r \leqslant 7$ kpc (see Fig. 6b). For this galaxy the signal-to-noise ratio (S/N) of the *H* image allows us to fit only the main component (i.e. the $r^{1/4}$ law). However, a disc component could be present but at the level of the noise. Therefore, for the south-eastern galaxy of NGC 5514 the near-IR photometric profile corresponds mainly to a bulge-dominant system (Sa, Sb or S0 galaxy).

A detailed study of the *H* and *I* luminosity profiles in the overlapping area of the two galaxies suggests that the eastern part of the main system is positioned (from our point of view) behind the second galaxy.

3.2 Long-slit spectrophotometry

Long-slit spectra of NGC 5514 were obtained from our Survey of Warm *IRAS* Galaxy Candidates. Using these spectra, we detected (and 'rediscovered'; see FL88) two extended regions with strong 'extranuclear' emission lines. This set of 1D data was the basis for the next 2D spectroscopic study. In addition, these long-slit observations allowed us to study a wide wavelength range (λλ3800–7500) and to analyse part of this wavelength range at high resolution (50 km s^{-1}).

On the other hand, it is useful to compare 1D and 2D data, since this analysis will help us to understand observations of more distant IR mergers/QSOs, where only 1D observations are available and it is not possible to separate spatially the different galactic components.

3.2.1 Moderate-resolution spectra

In this section we shall study the following three regions: (a) the main nucleus; (b) a strong extranuclear Hα + [N II] emission area, located to the west of the main nucleus; and (c) the second nucleus plus the close extended H II region area, positioned to the south-east of the main body.

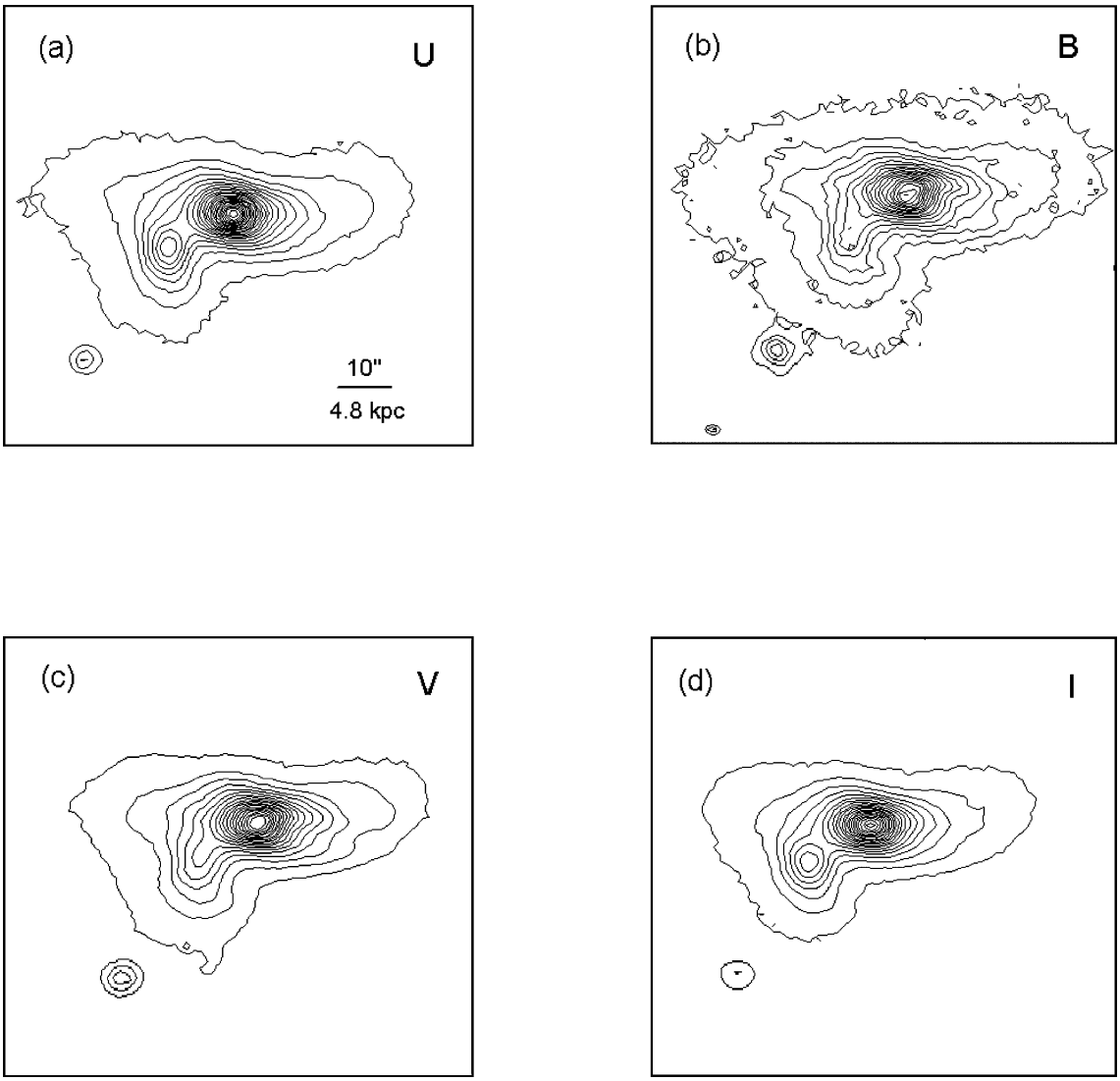

Figure 2. CASLEO optical broad-band contour map images of NGC 5514 (through the filters *U*, *B*, *V* and *I*). North is up, and east to the left.

Fig. 7 shows the 1D long-slit spectra obtained with moderate resolution (∼290–300 km s^{-1} FWHM) for these three main regions. Tables 2 and 3 show the calibrated fluxes and emission-line ratios of these spectra.

The main conclusions from these data are the following: (i) the emission-line ratios of the main nucleus are consistent with a weak LINER; (ii) the spectrum of the western area shows properties of a strong LINER system, with a faint continuum; (iii) the second nucleus and the extended H II complex depict emission-line ratios typical of H II regions and 'transition' LINER/H II objects.

In addition, the main nucleus shows the typical absorption lines of an old stellar population. In particular, for Mg I λ5175 (using the λλ5156–5196 window) an equivalent width EW ∼7.0 Å was measured.

For the western area with strong emission, the values of the fluxes (presented in Table 2) show that this region is the most luminous in the [N II] emission line. For the second nucleus plus the H II regions, the CTIO and CASLEO spectra (which cover a wide wavelength range) depict a relatively intense blue continuum, probably associated with the presence of a hot young massive stellar population. In addition, Table 2 shows that this region is the more luminous in Hα emission.

3.2.2 High-resolution spectra

We also studied the three main regions of the main body of NGC 5514 with CASLEO high spectral resolution spectroscopy (of 50 km s^{-1}). Fig. 8 and Tables 2 and 3 present the spectra, the values of the fluxes and the emission-line ratios. At this resolution, the presence of multi-emission-line components (ELCs), in the west/LINER region, were clearly detected.

In addition, Table 2 reveals an interesting result: the two types of long-slit spectra (with moderate and high resolution) give a value of the excess $E(B-V)_I = 0.0$, for the western area.

Finally, it is important to note that the results obtained from these 1D spectroscopic observations and the optical and near-IR image data (obtained mainly at CASLEO) were used as the basis for the 2D spectroscopic study. This 2D study was performed mainly in order to clarify the nature of the two strong extranuclear emission-line regions; and the physical conditions in both nuclei.

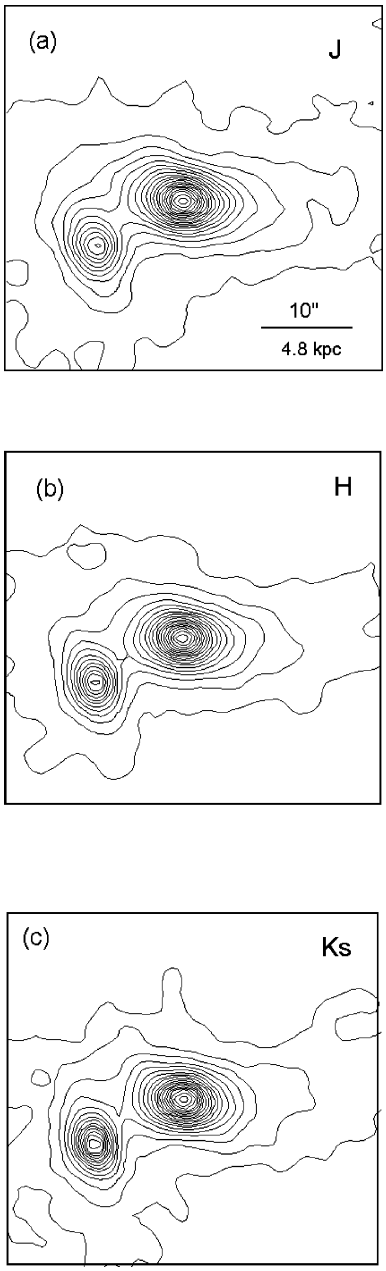

Figure 3. 2MASS near-IR contour map images of NGC 5514 (through the filters J, H and K_S). North is to the top, east is to the left.

3.3 Mapping two extranuclear starbursts and the nuclear region (2D spectroscopy)

Figs 9(a) and (b) show the red continuum and the Hα + [N II] emission-line maps for the central region of the main body of NGC 5514. These images are mosaics obtained by combining three individual WHT + INTEGRAL frames of 16.4 × 12.3 arcsec^2. Each mosaic covers a total area of ∼30 × 20 arcsec^2 (∼14.3 × 9.5 kpc^2).

FITS maps were obtained from the original ASCII data (following the procedure described in detail in Section 2.6), with a spatial sampling of 0.9 × 0.9 arcsec^2 and a typical seeing of ∼1 arcsec, FWHM.

Fig. 9(a) shows mainly the continuum emission from the two nuclei, whereas Fig. 9(b) depicts the strong Hα + [N II] emission line, mainly from the main nucleus and the two extranuclear extended structures located to the west and east of the main body. These regions are analysed in detail in the next subsections.

3.3.1 Mapping the supergiant galactic bubble

In order to study the strong extranuclear area where we previously detected extended LINER activity (with long-slit spectroscopy), the first WHT + INTEGRAL observation was centred on the west side of the main body of the merger. The main nucleus was thus positioned on the left border of this field (7.9 arcsec east and 1.2 arcsec north, from the centre of the fibre bundle).

Fig. 10 shows a supergiant galactic bubble, from the Hα + [N II] emission-line map, superposed on the individual fibre spectra (for this INTEGRAL position 1). Even in this figure alone the relation between the changes in the the profile of the lines and the structures in the bubbles is obvious. In particular, in the main knots the spectra show clear broad emission associated with the presence of multi-components (for details see Section 3.4), plus very strong [N II]/Hα ratios.

Fig. 11 presents the red continuum (adjacent to Hα) plus the individual Hα, [N II] λ6583, [S II] λλ6717 + 31, [O I] λ6300 and [O III] λ5007 emission-line contour maps for the position 1 (obtained from the 2D spectroscopic data). The continuum contour map depicts emission only from the main nucleus. However, all the emission-line contour maps show strong extranuclear emission from a supergiant galactic bubble with four main knots. This bubble shows a distorted ellipsoidal morphology with an elongation at $PA_{bubble} = 120^\circ \pm 10^\circ$, with major and minor axes of 13.6 arcsec (∼6.5 kpc) and 9.6 arcsec (∼4.5 kpc), respectively. The centre of the galactic bubble is positioned at 8.5 arcsec (∼4.1 kpc) to the west of the main nucleus.

In general, the morphology is the same for the stronger optical emission lines (Hα, [N II] λ6583, [S II] λ6717 + 31). In addition, the weaker emission lines, [O I] λ6300 and [O III] λ5007, give maps with relatively similar structures, but at low S/N (Figs 11e and f). However, Fig. 11(c) depicts an interesting difference: the [S II] λλ6717 + 31 emission map shows wide filaments at the border of the bubble, probably associated with OF structures. Similar results were found in the mergers with OF NGC 2623 and 3256 (Lípari et al. 2004a, 2000). This point will be analysed in Section 4.4.

It is important to study in detail the four main knots detected in this supergiant galactic bubble with 2D spectroscopic data. In Fig. 11(b) the positions of these knots are depicted and labelled. We note that different emission-line maps show substructures in knots 2 and 3. In these knots we call the main substructure 'a' and the second one 'b'. Tables 4–7 present flux and emission-line ratio values for each main structure in NGC 5514 (including the knots in the bubble), and also for the fibres located at the centre of these structures. For the case of the bubble region, Fig. 10 shows the positions and numbers for all the fibres in an INTEGRAL field.

We shall first analyse the properties of the knots using the emission-line maps. In all these maps (Fig. 11) strong emission at the position of the knots was detected. In particular:

(i) Knot 1, with an elongated shape (at $PA_{K1} = 110^\circ \pm 10^\circ$) and a major axis of 4.6 arcsec ∼2.3 kpc, is the most extended and luminous structure in the bubble. This knot is the only one with similar strong and extended morphology in all the observed emission lines.

For this knot a value of Hα flux $F_{H\alpha} = 2.5 \times 10^{-14}$ erg cm^{-2} s^{-1} was measured, and the corresponding luminosity is $L_{H\alpha} = 3.0 \times 10^{40}$ erg s^{-1}. In addition, knot 1 is the main structure closer to the centre of the bubble. This extended knot is then a good candidate to

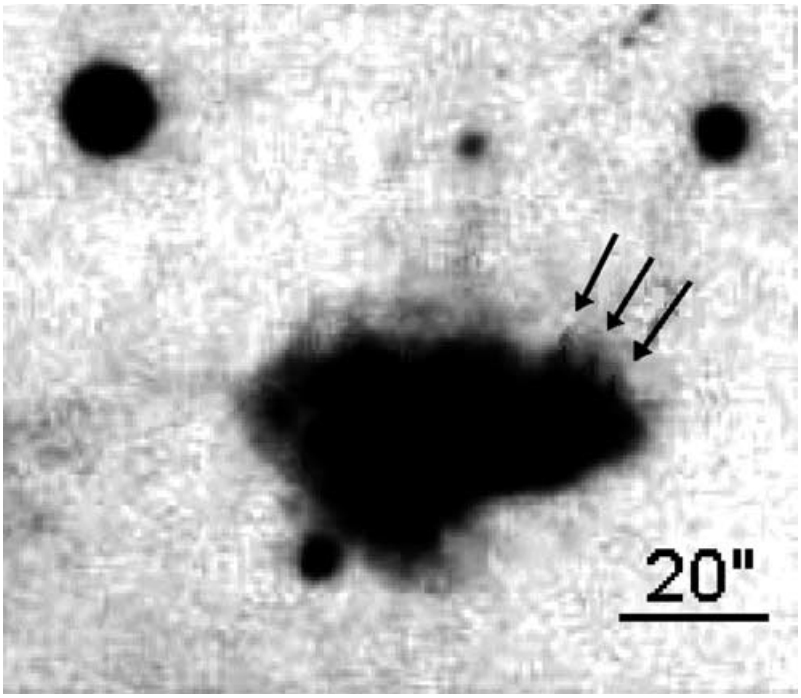

Figure 4. Palomar 103aO ($\sim B$) deep plate image of NGC 5514. The arrows show the position of three faint external filaments (see the text). North is up, and east to the left.

harbour an association of 'supermassive' star clusters (SSCs) that generate the OF process and the bubble.

(ii) Knots 2, 3 and 4 are less extended and more compact than knot 1, with diameters of ∼2.0 arcsec (∼1.0 kpc). These structures are located close to the border of the bubble.

We note that the emission-line contour maps depict substructures, especially inside knot 2. This knot 2 shows strong emission especially in the [S II] line, whereas knots 3 and 4 show strong emission in the [N II] and Hα lines, respectively.

(iii) The [S II] contour map (Fig. 11d) shows clearly at least four wide filaments emerging from the knots. Furthermore, in Section 3.5 we present kinematic evidence suggesting that these three 'external' knots are probably associated with the areas of ejection of the ionized gas and rupture of the external shell of the bubble.

The 2D WHT + INTEGRAL spectra of these knots will now be analysed. Fig. 12 depicts the blue and red 2D spectra of these four main knots. Tables 4–7 show the values of the fluxes, EW, FWHM and luminosities of the emission lines, and their ratios, for the bubble, the nuclei and selected areas of the complex of H II regions. In these tables the results of Section 3.4 (about the analysis of the multiple emission-line systems, in the 2D spectra) were used.

Tables 4–7 reveal an interesting fact: inside the bubble, the spectra for all the main knots depict LINER characteristics. These 'extranuclear' LINER properties could be associated mainly with the OF process. For a detailed study and discussion of this point see Sections 3.6 and 4.3.

Another interesting result obtained from these spectra (Fig. 12 and Table 4) is the detection in knots 1, 2a, 2b, 3a and 3b of Wolf–Rayet (WR) features at λ4560. It is interesting to note that the [N I] λ5199 emission line was also found in these knots (where we detected the WR bump). Similar behaviour (i.e. strong WR and [N I] emission) was observed in the spectra of the prototype WR galaxy NGC 6754 (Osterbrock & Cohen 1982). These clear WR features suggest the presence of a high number of massive stars (probably in 'young' SSCs), with ages $t < 6$ –8×10^6 yr in these knots.

For the main emission-line component of the bubble, a flux of $F_{\mathrm{H}\alpha} = 5.5 \times 10^{-14}$ erg cm^{-2} s^{-1} was measured and a total value of Hα luminosity, $L_{\mathrm{H}\alpha} = 6.3 \times 10^{40}$ erg s^{-1}, was derived. The dynamical and physical properties of this young OF in the bubble phase will be discussed in Section 4.4.

3.3.2 Mapping the nuclear region

The second position of the WHT + INTEGRAL fibre system was selected in order to study the two nuclear areas. The fibre system was centred midway between the two nuclei.

Fig. 13 shows the continuum adjacent to Hα, plus the individual Hα, [N II] λ6583 and [S II] λλ6717 + 31 emission-line contour maps (for position 2). The continuum contour map depicts mainly the emission from the nuclei. The emission-line maps show the main nucleus and the second nucleus superposed with the extended complex of giant H II regions.

Fig. 14 presents the blue and red 2D spectra for the two nuclei. These spectra exhibit the typical LINER features for the main nucleus and transition LINER/H II region properties for the second one.

For position 2, the INTEGRAL blue continuum map clearly shows the presence of extended bands/fringes and a faint continuum from the second nucleus, confirming the results obtained in Section 3.1.

3.3.3 Mapping the extended complex of giant H II regions

The INTEGRAL frame at position 3 was centred close to the complex of giant H II regions (and thus close to the second nucleus, which is located 3.7 arcsec east and 0.2 arcsec south of the centre of the fibre bundle). In this area and using long-slit spectroscopy, we

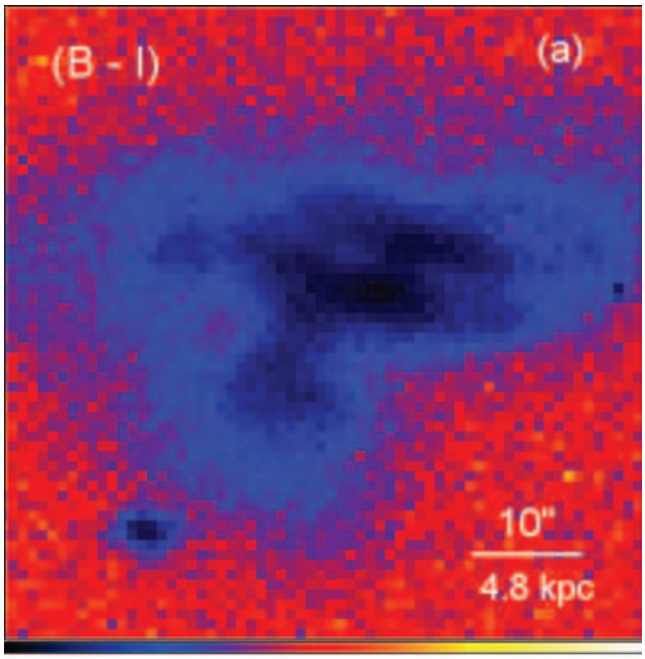

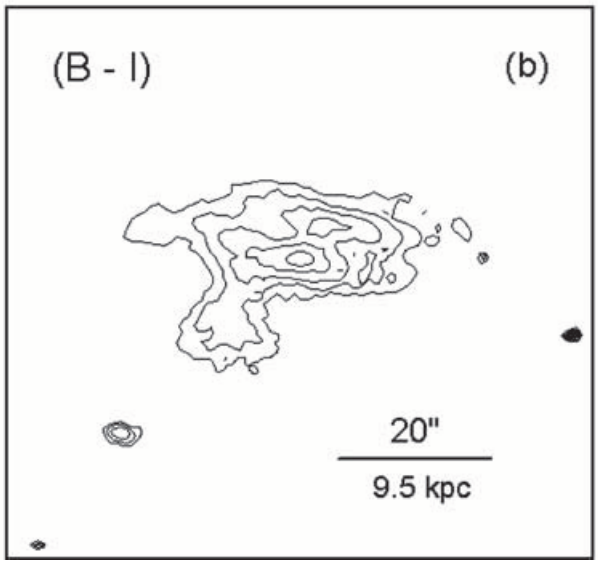

Figure 5. CASLEO colour ($B - I$) broad-band image and contour map of NGC 5514. North is up, and east to the left.

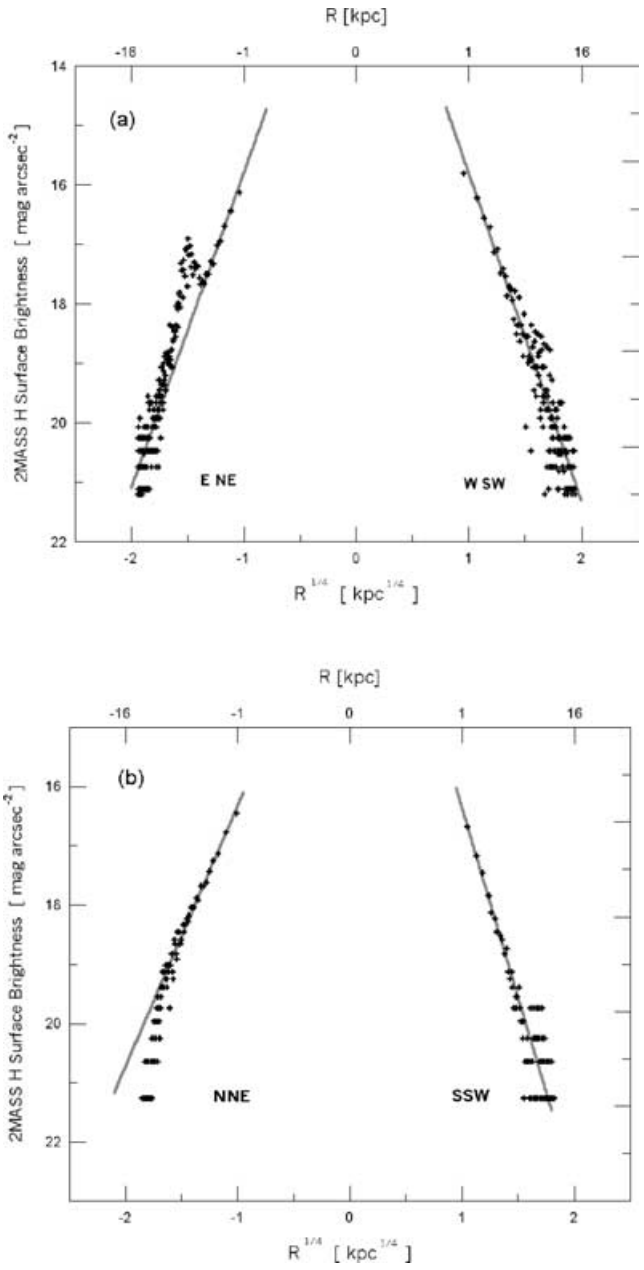

Figure 6. 2MASS H surface brightness (mag arcsec^{-2}) plotted against the fourth root of the radius, for the main (a) and the second (b) galaxies, of the original systems that collided.

had previously detected a very extended emission, with a composite or transition LINER/H II region spectrum. We note that objects with transition LINER/H II region properties are those with intermediate emission-line ratios, between pure LINERs and typical H II regions. These objects would be classified as LINERs except, mainly, that their [O I] λ6300 line strengths are too small in comparison with other lines to meet the formal LINER criteria. For more detailed definitions of these types of activity see Heckman (1980, 1987); Ho, Filippenko & Sargent (1993, 1997); Heckman (1996); Ho (1996) and Barth & Shields (2000).

Fig. 15 shows the continuum adjacent to Hα and the Hα, [N II] and [S II] emission-line contour maps for position 3. The continuum contour map shows mainly the emission from the second nucleus. The emission-line contour maps depict an extended H II region complex, which at Hα, [N II] λ6583 and [S II] λλ6717 + 31 shows a compact strong emission-line area, with the peak located at 1.7 arcsec ∼810 pc to the east of the second nucleus. In addition, this extended complex shows an elongated shape (at PA ∼ 20° ± 8°), with major and minor axes of 10.8 arcsec ∼5.1 kpc and 6.0 arcsec ∼2.9 kpc, respectively. The morphology is similar for these three main optical emission lines (Figs 15b–d).

Fig. 16 depicts the blue and red 2D spectra of selected areas of this H II region complex: the main central knot and two areas at the border. Tables 4–7 show the values of the fluxes, EW, FWHM, luminosities of the emission line and their ratios for these selected

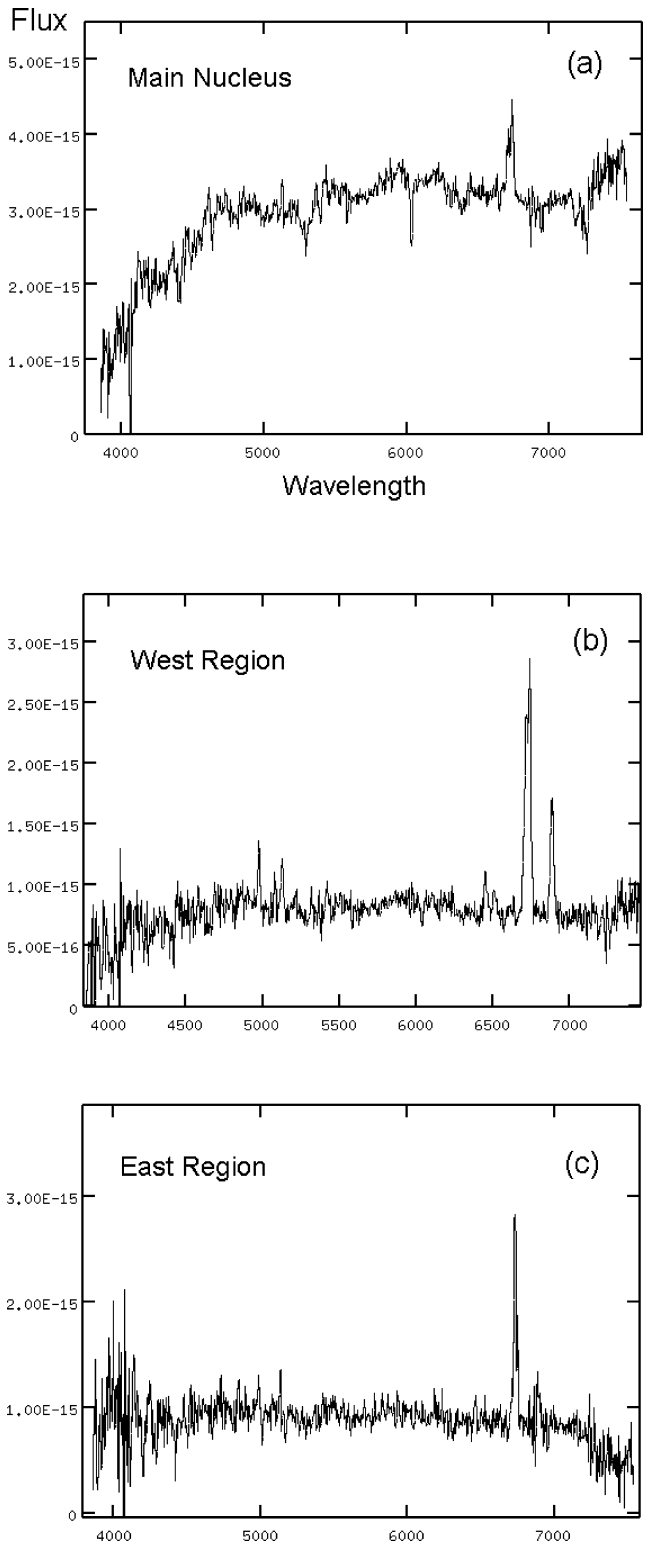

Figure 7. CASLEO long-slit spectra (of medium spectral resolution: 290 km s^{-1}) for the three main emission regions in NGC 5514. The scales of flux are given in units of [erg × cm^{-2} × s^{-1} × $Å^{-1}$] and wavelength in [Å].

regions. In particular, these plots and tables show: (i) inside of this complex, the values of the emission-line ratio (ELR) are consistent with gas ionized by hot stars (i.e. typical of H II regions); (ii) for the second nucleus, the values of the ELR (Table 5) are consistent with transition LINER/H II properties, for an area with radius $r \sim 2$ arcsec ~ 950 pc; however, the ELRs for the central fibre ($r \sim 1$ arcsec ~ 470 pc; Table 7) show LINER properties; (iii) at the border of this extended complex the spectra depict a weak but clear OF component (Figs 16c and d) and their values of the ELR are consistent with LINER properties (similar to those observed in the OF of the galactic bubble).

For this region, a 'total' Hα flux of $F_{H\alpha} = 5.9 \times 10^{-14}$ erg cm^{-2} s^{-1} was measured, and the corresponding luminosity is $L_{H\alpha} = 6.6 \times 10^{40}$ erg s^{-1}. This last value is also compatible with starburst areas (Kennicutt, Keel & Blaha 1989).

3.4 Multiple components in the emission lines (2D and 1D high-resolution spectroscopy)

An important point in the study of spectra obtained with relatively high spectral resolution is the analysis of multiple components (in each emission line, especially in the stronger lines [N II] λ6583 and Hα). This type of detailed study was performed for several nearby galaxies, including systems with GW, e.g. NGC 3079, 3256, 1052, 4550, 7332, Cen A, etc. (e.g. Bland, Taylor & Atherton 1987; Veilleux et al. 1994; Plana & Boulesteix 1996; Lípari et al. 2000).

For NGC 5514, 1D and 2D spectra with relatively high resolution (∼50 and 100 km s^{-1}) were obtained. From these data a detailed study of multiple ELCs was performed (especially in order to analyse OF motion), and the following main results were obtained:

(i) *Main component (MC).* In the two nuclei and in the H II region complex mainly a single strong emission-line component was detected, in ∼81 per cent of the observed field. This ELC was measured and deblended using the software SPLOT (see Section 2.6).

(ii) *Blue and red bubble component.* The presence of two strong components was observed, in the region of the bubble. These ELCs are blue- and redshifted, in relation to the systemic velocity (of the merger); and they were deblended using the software SPECFIT.

(a) *Blue bubble component (BBC).* The strong blue component was detected in almost the entire extension of the bubble (which is ∼12 per cent of the observed mosaic), while the red one was observed mainly in the central and in the knot areas.

Thus, in several regions this blue ELC was measured blended mainly with a weak red bubble ELC. However, in several areas (mainly in the knots) these blue and red bubble ELCs show similar strengths, so the deblending was more complex.

(b) *Red bubble component (RBC).* The red bubble ELC was detected in ∼90 per cent of the bubble with a very weak strength. Only in the knots of the bubble does this RBC show strong features. Thus, in order to measure this component a detailed analysis was required.

However, in the Hα + [N II] blend this red ELC was relatively easily measured, since the emission line [N II] λ6583 (from the red ELC) is located on the red boundary of this blend.

Fig. 17 shows examples of each component: MC, BBC and RBC, in the spectra obtained from the extraction of individual fibres (for different regions of the main body).

Fig. 18 depicts the emission-line map for the red bubble component, in the [N II] λ6583 line (at position 1). This plot shows: (1) two strong and compact peaks of emission with a diameter $d = 4$ arcsec (∼1.9 kpc), one located close to the position of knot 2 and the other

Table 2. Fluxes of emission lines of NGC 5514, from long-slit spectroscopy (medium and high resolution; from CASLEO).

Lines	Fluxes[a] (M.Res.[b])			Fluxes[a] (H.Res.[c])		
EW, FWHM, Lum	Main Nuc.	west area	Sec.Nuc.+H II Reg.	Main Nuc.	west area	Sec.Nuc.+H II Reg.
Hβ λ4861	absor.	1.8	1.4	(0.4)	1.8	1.0
[O III] λ5007	1.4	2.9	1.5	1.1	3.0	1.2
[O I] λ6300	1.2	2.0	1.4	0.8	2.4	1.1
Hα λ6563	1.6	5.2	6.3	1.4	5.2	4.8
[N II] λ6583	4.3	8.7	2.0	2.4	9.1	2.8
[S II] λ6717	1.2	3.6	2.5	0.5	4.1	1.5
[S II] λ6731	1.0	2.6	2.4	0.4	3.3	1.3
Hα/Hβ	–	2.9	4.5	(3.5)	2.9	4.8
$E(B-V)_I$	–	0.0	0.4	(0.2)	0.0	0.5
EW Hβ (Å)	–	32.0	23.0	(2.9)	33.0	29.0
EW [O III] (Å)	4.9	57.0	24.9	6.5	51.0	40.0
EW Hα (Å)	6.4	74.4	95.0	5.8	50.0	51.0
EW [N II] (Å)	13.3	126.0	45.0	10.5	93.0	25.0
FWHM Hα (km s^{-1})	365	550	230	340	480	190
FWHM [N II] (km s^{-1})	510	595	300	470	515	250
Lum Hα[d]	1.8	6.0	7.2	1.6	5.7	5.5
Lum [N II] λ6583	4.9	10.0	2.3	2.8	10.4	3.2

[a]The fluxes are given in units of 10^{-14} erg cm^{-2} s^{-1}.
[b]Flux values from CASLEO and CTIO data of moderate spectral resolution ($\sim$290–300 km s^{-1}).
[c]Flux values from CASLEO data of high spectral resolution ($\sim$50 km s^{-1}).
[d]The luminosities are given in units of 10^{40} erg s^{-1}.

Table 3. Emission-line ratios of NGC 5514, from long-slit spectroscopy (medium and high resolution; from CASLEO).

Regions	log[O III]/Hβ[a]	log[O I]/Hα[a]	log[N II]/Hα[a]	log[S IIs]/Hα[a]	[S II]/[S II][a]	Spectral type
Medium spectral resolution						
Main nucleus	–	−0.22	0.36	0.04	1.20	L
West area	0.34	−0.39	0.24	0.16	1.28	L
Sec. nucleus+H II reg	0.07	−0.81	−0.35	−0.13	1.04	L/H II
High spectral resolution						
Main nucleus	(0.4)	−0.25	0.35	−0.04	1.23	L
West area	0.3	−0.36	0.20	0.13	1.25	L
Sec. nucleus+H II reg	0.1	−0.63	−0.30	−0.15	1.12	L/H II

[a][O III] λ5007; [O I] λ6300; [N II] λ6583; [S IIs] $\lambda\lambda$6716+6731; [O II]λ3727; [S II]/[S II] λ6716/λ6731.
Column 7: for the spectral type, L and L/H II mean: LINERs, and transition objects, between LINERs and H II regions.
The spectral resolutions used were 290 and 50 km s^{-1}.
The values between parentheses are data with low S/N.

between knots 1 and 4; (2) a weak compact peak located to the north-west of knot 1; (3) a very interesting extended structure detected in the south-east region of the map (i.e. on the eastern border of the bubble), with a quadrupolar substructure close to knot 2a. This extended + quadrupolar structure is probably a main ejection from the bubble. This ejection is also suggested by four kinematic velocity field maps, and the [S II] emission image (see Sections 3.5 and 3.3). More specifically, this RBC in the extended ejection area shows: (1) an elongated shape with an extension of 8.3 arcsec $\sim$ 4.0 kpc; and (2) an alignment with the major axis of the bubble ($PA_{ejection} = 100^\circ \pm 10^\circ$). We note that in this ejection area the red bubble system is the only component detected.

(iii) *Weak outflow component (OF1).* In the complex of H II regions several areas show weak blue outflow components in addition to the main single systems. The plots of this OF component were presented in Section 3.3 (Figs 16c and d).

It is important to note that for the nearest supergiant galactic bubble in NGC 3079, Veilleux et al. (1994) already reported similar results: the presence of two clear emission-line systems, also blue- and redshifted from the V_{sys}. They suggested – for NGC 3079 – that these two ELCs are associated with the emission from the external shell of the bubble. Thus, following this last suggestion (Filippenko & Sargent 1992; Veilleux et al. 1994), we propose for the blue and

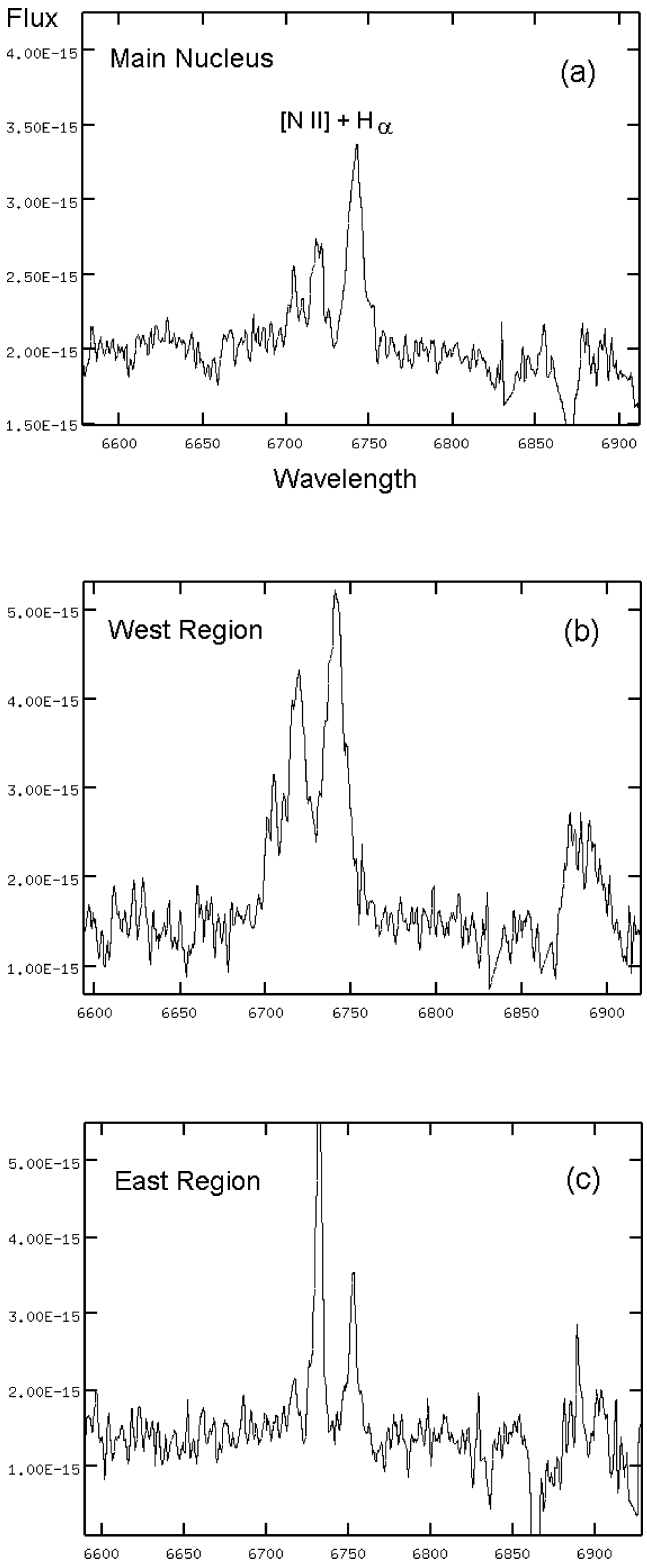

Figure 8. CASLEO long-slit spectra (of high spectral resolution: 50 km s^{-1}) for the three main emission regions of NGC 5514. The scales of flux are given in units of [erg × cm^{-2} × s^{-1} × $Å^{-1}$] and wavelength in [Å].

red ELCs (in the bubble of NGC 5514) a similar interpretation: that the BBC comes from the nearest side of the external shell, and probably for this reason this blue ELC was observed in almost all the extension of the bubble. Meanwhile, the RBC came from the far side, and thus it is partially obscured in several areas. Furthermore, we are probably looking at the red ELC through an optically thin bubble, which is consistent with the 1D and 2D spectroscopic results, in the sense that the internal reddening in the bubble shows mainly low values of the excess $E(B-V)_I$ (in the range 0.0–0.5, see Tables 2, 4 and 6).

In conclusion, with the spectral resolution of this study we can identify at least four different emission-line systems. These results are specially important for the generation and interpretation of the velocity fields and emission-line ratio maps.

3.5 Mapping the ionized gas kinematics (2D spectroscopy)

The ionized gas velocity field (VF) maps were constructed on the basis of the result of the previous analysis of multiple components in the emission lines (Section 3.4). Specifically, for each of the four main ELCs the centroid velocities, fluxes and FWHM were measured and deblended (for the lines [N II] λ6583, Hα, [S II] λ6731, [O I] λ6300, [O III] λ5007 and Hβ), using the SPECFIT and SPLOT software tasks.

Considering that more than 65 per cent of our emission-line measurements show values in the range $4 > [\mathrm{N\,II}]\,\lambda6583/\mathrm{H}\alpha > 1$, we present and discuss mainly the [N II] λ6583 velocity field map, which has lower uncertainties and a better resolution than the Hα radial velocity map.

Fig. 19 shows a mosaic of the three observed INTEGRAL [N II] λ6583 velocity fields for the main body of NGC 5514. This mosaic covers an area of ∼30 × 20 $arcsec^2$ (14.3 × 9.5 kpc^2). The uncertainties vary from approximately ±10 km s^{-1} in the regions where the emission lines are strong (mainly the nuclei and the two extranuclear starbursts), to ±30 km s^{-1} for the weakest lines away from the central area.

Following the procedure performed previously for NGC 3256 and 2623 (Lípari et al. 2000, 2004a), the kinematic maps were constructed mainly for the main/strong ELCs, i.e. the blue bubble system (inside the bubble), the red bubble component (in knots 2, 3 and 4, and in the south-east areas of the shell), and the single main-body component in the remaining areas.

In general, the colour [N II] λ6583 emission-line VF map (Fig. 19) shows:

(i) an extended lobe of blue/approaching velocities in the region of the bubble, from which an extended ejection emerges;

(ii) an extended area of strong red/recessing velocities to the eastern border of our mosaic, including the region of the second nucleus;

(iii) a circular lobe of blueshifted velocities, which is located between the extended blue and red lobes;

(iv) a small lobe of blueshifted velocities located in the north-east border of the mosaic field.

Using all the observed 2D [N II] λ6583 and Hα emission lines, a mean value of the systemic velocity $V_{\mathrm{Sys}} = 7358 \pm 20$ km s^{-1} was measured, while the main and secondary nucleus have radial velocities of $V_{\mathrm{MainNuc}} = 7280 \pm 20$ km s^{-1} and $V_{\mathrm{SecNuc}} = 7680 \pm 20$ km s^{-1}. This V_{Sys} was used as the zero value for all the velocity fields.

3.5.1 The kinematics of the supergiant galactic bubble

Fig. 20 displays detailed 2D kinematic contour maps for the position of the bubble (position 1; 16.4 × 12.3 $arcsec^2$), which were obtained from the measured emission lines [N II] λ6583, Hα and [O III] λ5007.

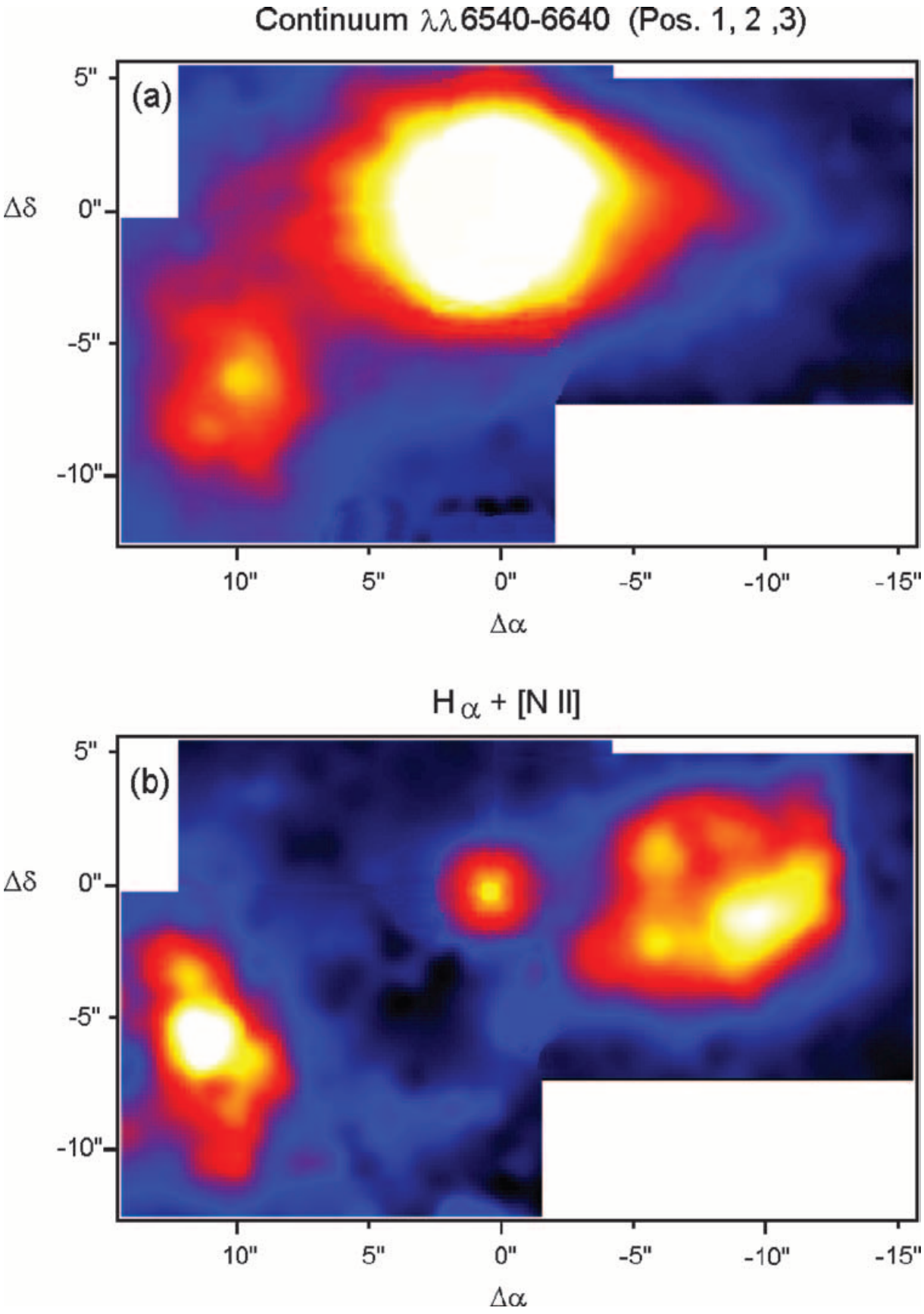

Figure 9. WHT + INTEGRAL mosaic maps of the continuum λλ6540–6640 (a) and Hα+[N II] emission (b). The position of the main nucleus was defined as the zero-point (0,0). North is up, and east to the left.

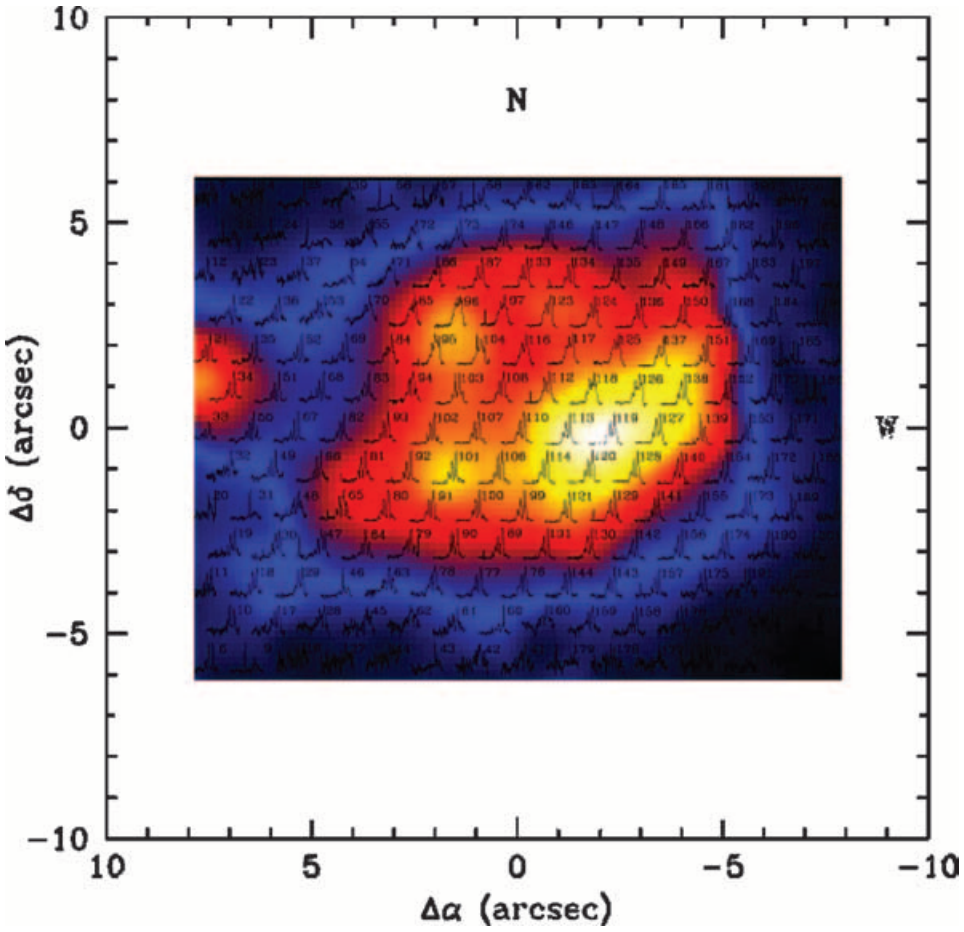

Figure 10. Superposition of the bubble Hα+[N II] map and 2D INTEGRAL spectra of NGC 5514 (the spectra are shown at the wavelength region of Hα + [N II]). The number on each spectrum indicates the fibre number. North is up, and east to the left.

In the study of the general properties of the VF (in the bubble region) the following main results were found:

(i) Probably, the most interesting feature for this area (and for all the VF) is the clear extended ejection of ∼4 kpc, in the east side of the bubble, which started in a position close to knot 2 and is aligned with the major axis of the bubble (at $PA_{ejection} = 100^\circ \pm 10^\circ$ and $PA_{bubble} = 120^\circ \pm 10^\circ$).

In this merger the [O III] λ5007 emission line is very weak (see Section 3.3). However, even in this case the VF map shows, in its south-east border, the feature associated with the main ejection process.

In addition, this ejection shows very interesting substructures inside. In particular, at small scale a quadrupolar OF/ejection was found (for details see the last paragraphs in this section).

(ii) In the west side of the bubble (relatively close to knot 1) there is an approaching/blueshifted velocity region, which is probably an ejection, also aligned with the PA of the major axis of the bubble. We note that two opposite ejections in the extreme of the ellipsoidal bubble are expected in the OF rupture phase.

This blueshifted ejection is clearly weaker than that observed in the east side. However, this feature is located close to the west border of our observed mosaic.

(iii) Another two weak ejections were found, associated with knots 3 and 4. We note that these features were observed in more detail in the [S II] VF (see the next subsection).

(iv) In this supergiant galactic bubble, close to the centre, the following mean OF velocities were measured, for the blue and red components: $V_{OF\,blue} = (-320 \pm 20)$ km s^{-1} and $V_{OF\,red} = (+265 \pm 25)$ km s^{-1}, relative to the systemic velocity.

Fig. 21 shows the [N II] λ6583 velocity profile, obtained from the velocity field and through the main ejection (at PA ∼ 100°). This plot exhibits a variation of velocity in the region of knot 2 (i.e. the beginning of the main ejection) of $\Delta V \sim 1000$ km s^{-1}. This high value in the variation of velocity could be explained as the wall/region of giant OF shocks. We note that the other possible process that could explain the detected ΔV in the VF of the merger (such as tidal disruption of a disc, etc.) shows mostly very low velocity values, as observed in the velocity field of nearby mergers ($\Delta V_{max} \leqslant 300$ km s^{-1}, e.g. Lípari et al. 2000, 2004a). It is important to note that in order to confirm this result an interesting test was performed: we derived a second [N II] velocity field (for this position 1) following the blue bubble component, even where this BBC is very weak. Thus, the red component was included only where the BBC disappears. Even in this case a similar plot to Fig. 20 was obtained and only the region of high ΔV shows a small shift in position.

In order to analyse in detail the substructures in the ejections and the knots, a basic study was performed, following the good result obtained using the filtering technique in the study of the VF in NGC 2623. We probably made the simplest approach to the mean motion,

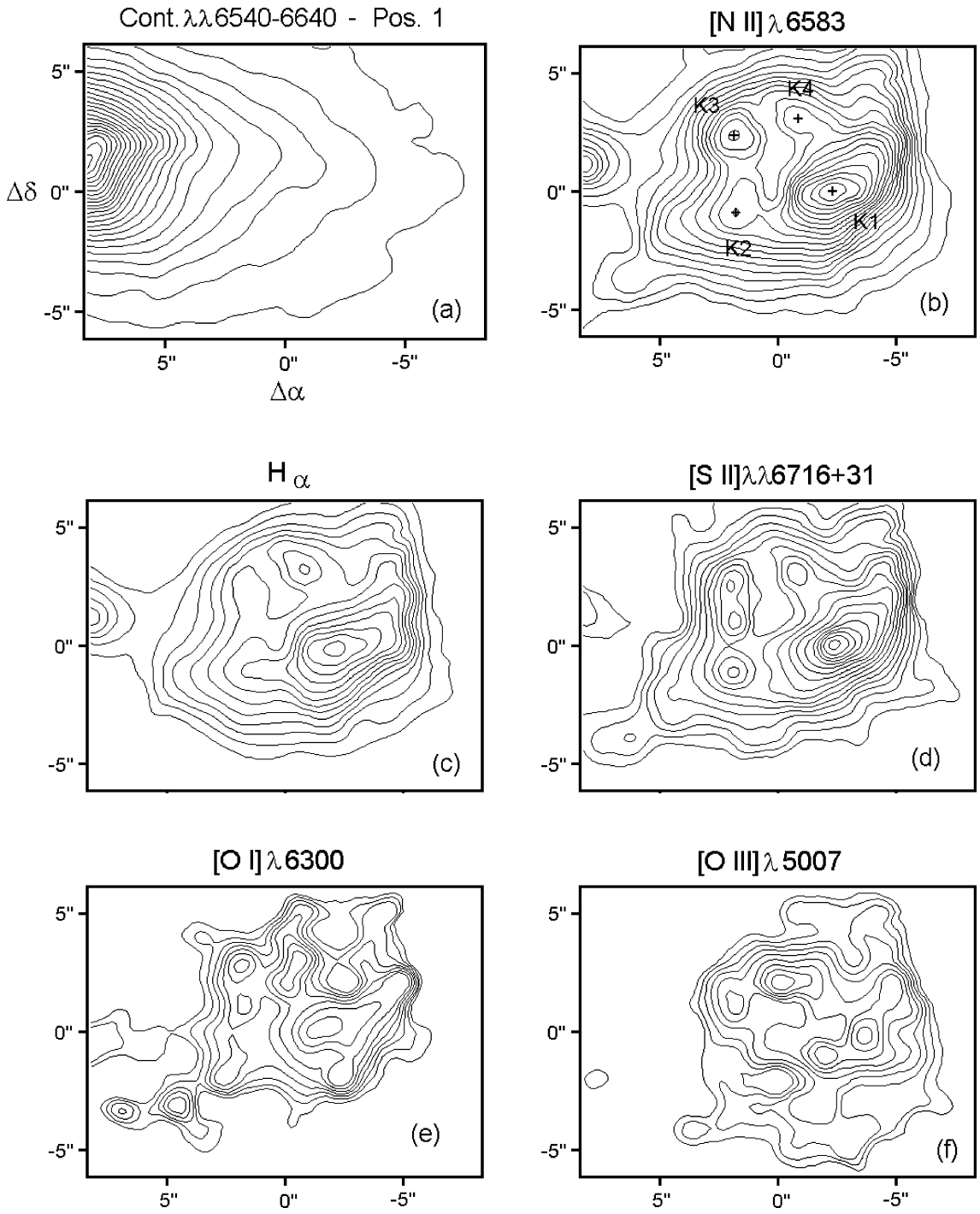

Figure 11. WHT + INTEGRAL maps of the supergiant bubble in NGC 5514 (position 1) for (a) a narrow continuum adjacent to Hα; (b), (c), (d), (e) and (f) pure [N II], Hα, [S II], [O I], [O III] emission line, respectively (the continuum was subtracted). The crosses show the position of the knots. The position of the centre of the fibre bundle was defined as the zero (0,0) value. North is up, and east to the left.

using Gaussian filtering, which gives a smooth [N II] λ6583 velocity field showing the four main ejections more clearly (Fig. 22a). Furthermore, at the beginning of these four ejections very interesting structures in the residuals map were found.

Specifically, after the subtraction of this smooth VF, the residuals show, first, a 'quadrupolar' structure (Fig. 22b), in the beginning of the main ejection, close to knot 2. This quadrupolar OF feature shows an 'X' shape with redshifted velocity values, plus three or four blueshifted symmetric lobes (inside of this red 'X' structure). The residual in this area reaches values close to $|V_{\rm max}| \sim 400$ km s^{-1}. We note that this OF quadrupolar structure is similar to those detected in the OF of some planetary nebulae (Manchado, Stanghellini & Guerrero 1996; Guerrero & Manchado 1998; Lopez et al. 1998; Muthu & Anandarao 2001).

Two similar residual OF structures were detected close to knots 3 and 4, also at the beginning of the other two ejections. However, in these cases the velocity residuals show 'bipolar' shape, with redshifted velocity values, plus two blueshifted symmetric lobes (in

Table 4. Fluxes of emission-lines of NGC 5514 (from WHT + INTEGRAL 2D spectroscopy, total values).

Lines EW FWHM, Lum	Comp	Fluxes[a] Knot 1	Knot 2a	Bubble Knot 2b	Knot 3a	Knot 3b	Knot 4	MNuc	SNuc	MKnot	H II reg EBorder	WBorder
Hβ λ4861	BBC	3.2	1.0	0.2	0.4	0.6	1.8	–	–	–	–	–
	RBC	0.3	0.1	0.3	0.6	0.1	–	–	–	–	–	–
	MC	–	–	–	–	–	–	0.7	1.0	1.0	0.4	0.6
	OF1	–	–	–	–	–	–	–	–	–	0.1	0.1
[O III] λ5007	BBC	4.4	1.0	0.2	0.9	0.8	2.5	–	–	–	–	–
	RBC	0.2	0.2	0.2	0.6	0.1	–	–	–	–	–	–
	MC		–	–	–	–	–	1.4	0.9	0.8	0.7	1.3
	OF1	–	–	–	–	–	–	–	–	–	(0.1)	(0.1)
[N I] λ5199	BBC	2.4	1.1	(0.3)	0.3	0.5	–	–	–	–	–	–
	RBC	–	–	0.6	–	–	–	–	–	–	–	–
	MC	–	–	–	–	–	–	–	–	–	–	–
	OF1	–	–	–	–	–	–	–	–	–	–	–
[O I] λ6300	BBC	7.5	2.7	0.5	0.9	0.8	3.0	–	–	–	–	–
	RBC	0.8	0.4	0.6	1.2	0.4	–	–	–	–	–	–
	MC	–	–	–	–	–	–	2.0	1.1	0.6	0.4	1.1
	OF1	–	–	–	–	–	–	–	–	–	0.2	0.1
Hα λ6563	BBC	23.3	5.6	0.7	1.1	2.1	5.5	–	–	–	–	–
	RBC	1.3	0.7	1.0	3.7	0.8	–	–	–	–	–	–
	MC	–	–	–	–	–	–	2.8	7.7	4.6	1.7	2.8
	OF1	–	–	–	–	–	–	–	–	–	1.1	0.2
[N II] λ6583	BBC	31.6	9.4	1.0	3.1	4.0	8.1	–	–	–	–	–
	RBC	1.7	1.1	1.4	3.1	1.3	–	–	–	–	–	–
	MC	–	–	–	–	–	–	4.8	4.1	2.4	1.8	2.7
	OF1	–	–	–	–	–	–	–	–	–	1.1	0.3
[S II] λ6717	BBC	9.8	2.0	0.4	0.5	1.9	3.5	–	–	–	–	–
	RBC	0.8	(0.2)	0.8	1.8	(0.4)	–	–	–	–	–	–
	MC	–	–	–	–	–	–	1.6	2.1	0.9	0.6	1.2
	OF1	–	–	–	–	–	–	–	–	–	(0.3)	0.1
[S II] λ6731	BBC	9.0	2.7	0.4	(0.5)	1.9	2.1	–	–	–	–	–
	RBC	0.8	0.2	0.7	1.7	0.4	–	–	–	–	–	–
	MC	–	–	–	–	–	–	1.1	1.6	0.8	0.5	1.0
	OF1	–	–	–	–	–	–	–	–	–	0.2	0.1
WR bump (λ4650)	MC	5.7	2.1	1.4	1.2	1.4	–	–	–	–	–	–
Hα/Hβ	BBC	7.2	9.4	3.5	2.8	3.5	3.1	–	–	–	–	–
	RBC	4.3	7.0	3.3	6.2	8.0	–	–	–	–	–	–
	MC	–	–	–	–	–	–	4.0	7.7	4.6	4.3	4.6
	OF1	–	–	–	–	–	–	–	–	–	11.0	3.0
EW Hα (Å)	BBC	152	47	11	10	25	85	–	–	–	–	–
	RBC	6	5	15	33	11	–	–	–	–	–	–
	MC	–	–	–	–	–	–	6	47	79	24	22
	OF1	–	–	–	–	–	–	–	–	–	15	2
FWHM Hα (km s^{-1})	BBC	350	270	200	250	270	360	–	–	–	–	–
	RBC	200	260	215	290	230	–	–	–	–	–	–
	MC	–	–	–	–	–	–	240	150	122	370	270
	OF1	–	–	–	–	–	–	–	–	–	330	190
Lum Hα[b]	BBC	26.7	6.4	0.8	1.3	2.4	6.3	–	–	–	–	–
	RBC	1.5	0.8	1.2	4.2	0.9	–	–	–	–	–	–
	MC	–	–	–	–	–	–	3.2	8.8	5.3	2.0	3.2
	OF1	–	–	–	–	–	–	–	–	–	1.3	0.3
Lum WR	MC	6.5	2.4	1.6	1.4	1.6	–	–	–	–	–	–

[a]The fluxes are given in units of 10^{-15} erg cm^{-2} s^{-1} (from 2D spectroscopy with a resolution of $\sim$100 km s^{-1}).
[b]The luminosities are given in units of 10^{39} erg s^{-1}.
Column 2: emission-line components (Comp), where BBC, RBC, MC and OF1 are the blue bubble component, red bubble component, main component and outflow system-1, respectively.
The values between parentheses are data with low S/N.
MNuc, SNuc, MKnot, EBorder and WBorder denote the main nucleus, second nucleus, main knot, east border and west border, respectively.

Table 5. Emission-line ratios of NGC 5514 (2D spectroscopy, total values).

Regions	Comp	log[O III]/Hβ^a	log[O I]/Hα^a	log[N II]/Hα^a	log[S IIs]/Hα^a	[S II]/[S II]^a	Spectral type
Bubble							
Knot 1	BBC	0.14	−0.49	0.13	−0.09	1.09	L
	RBC	−0.18	−0.21	0.12	−0.21	1.00	L
Knot 2a	BBC	0.00	−0.31	0.22	−0.05	0.85	L
	RBC	0.30	−0.24	0.20	−0.24	(1.0)	L
Knot 2b	BBC	0.00	−0.20	0.16	0.06	(1.0)	L
	RBC	−0.17	−0.22	0.15	0.18	1.14	L
Knot 3a	BBC	0.35	−0.09	0.45	0.00	1.00	L
	RBC	0.00	−0.49	−0.08	−0.02	1.06	L
Knot 3b	BBC	0.13	−0.34	0.30	0.24	1.11	L
	RBC	0.00	−0.30	0.24	0.00	1.00	L
Knot 4	BBC	0.14	−0.26	0.17	0.01	1.66	L
Main nucleus	MC	0.30	−0.15	0.23	−0.02	1.45	L
Second nucleus	MC	−0.05	−0.85	−0.27	−0.32	1.31	L/H II
H II region complex							
Main knot (H II reg)	MC	−0.10	−0.88	−0.28	−0.43	1.13	L/H II
East-border (H II reg)	MC	0.24	−0.63	0.03	−0.19	1.20	L
	OF1	0.00	−0.74	0.00	−0.34	1.50	L
West-border (H II reg)	MC	0.33	−0.40	−0.02	−0.11	1.20	L
	OF1	0.00	−0.30	0.18	0.00	1.00	L

^{a}[O III] λ5007; [O I] λ6300; [N II] λ6583; [S IIs] λλ6716+6731; [S II]/[S II] λ6716/λ6731.
Column 2: emission-line components (Comp), where BBC, RBC, MC and OF1 are the blue bubble component, red bubble component, main component and outflow system 1, respectively.
Column 8: for the spectral type, L and L/H II mean: LINERs, and transition objects, between LINERs and H II regions.
The values between parentheses are data with low S/N.

each area; Fig. 22b). The values of the residual, in these knot regions, reach $|V_{max}| \sim 300$ and 250 km s^{-1}, respectively.

Another residual structure of approaching/blueshifted velocity was detected, at the west side of the bubble and relatively close to knot 1 (Figs 22a and b). This structure is probably part of a blueshifted ejection, also aligned with the PA of the major axis of the bubble. The velocity values of these blueshifted residuals reach $V_{max} \sim -280$ km s^{-1} (which is also a very high value).

We note that only for this INTEGRAL position 1 do the values of the residuals (obtained from the subtraction of a smooth VF) show $|V| \geqslant 100$ km s^{-1}. The residual structures detected in the bubble/position-1 have velocity values $|V| \geqslant 250$ km s^{-1}, confirming the real nature of these features, which are also evident in the original VF map.

In general, these kinematics results are consistent with expansion of the shell and with the beginning of the blowout GW phase. A discussion of this process is presented in Section 4.4.

3.5.2 The kinematics of the bubble in [S II]

In Section 3.3 we found that in the bubble region the [S II] emission-line map shows clear extension/wide-filaments, which start in the three more external knots. Therefore it is important to study in detail the VF of this emission line. This blend of [S II] λλ6716 + 31 is strongly absorbed by our atmosphere, in the blue side. However, at the red border of this [S II] blend, the line [S II] λ6731 is located far from the absorption range; and thus this line was measured easily.

In addition, we note that for this [S II] λ6731 emission line, mainly the main component was measured, since this [S II] blend was absorbed in the blue side (which precludes a clear separation between the BBC and RBC). Fig. 20(b) shows the VF contour map for the main component of the line [S II] λ6731, which is practically a VF for the BBC in 90 per cent of the bubble, but in the area of the three external knots the RBC is the dominant component.

This plot probably shows the clearest features of the three main ejections:

(i) Two weak ejections were found, associated with knots 3 and 4. These ejections are almost perpendicular and less extended than the stronger one, reaching ∼1–2 kpc. We note that the main ejections start in one of the three 'external' knots. Probably, these results are consistent with the fact that the bubble is in the beginning of the rupture phase.

(ii) The main/strongest ejection was also clearly observed in this [S II] emission-line VF. This feature was detected to have similar characteristics to the previously presented VFs.

A possible explanation of the fact that [S II] is probably one of the best tracers of the OF process will be discussed in Section 4.4.

3.5.3 The kinematics of the region of the nuclei

Fig. 23(a) displays detailed 2D kinematic contour map, for the position of the nuclei (position 2), obtained from the measured [N II] λ6583 emission line. This map was constructed mainly for the main emission-line component.

From the study of the general properties of the VF in this region, we note the following main results: at the north-east border of the field, the isovelocity lines show strong stretching (probably associated with a high concentration of mass). In addition, almost all the area of the main extended ejection (of the bubble) is included in this field.

In the area of stretching isovelocity lines the B image shows a faint knot (which was also observed in the B contour image published by FL88: their fig. 2a). In Section 4.1 we will discuss the possibility

Table 6. Fluxes of emission lines of NGC 5514 (from WHT + INTEGRAL 2D spectroscopy, central fibre values).

Lines EW FWHM	Comp	Fluxes[a]										
		Knot 1 P1-f126	Knot 2a P1-f101	Bubble Knot 2b P1-f47	Knot 3a P1-f96	Knot 3b P1-f103	Knot 4 P1-f123	MNuc P2-f138	SNuc P3-f93	MKnot P3-f68	H II Reg EBorder P3-f48	WBorder P3-f101
Hβ λ4861	BBC	0.5	0.3	0.1	0.2	0.3	0.5	–	–	–	–	–
	RBC	0.1		0.1	0.2	–	–	–	–	–	–	–
	MC	–	–	–	–	–	–	0.3	0.3	0.4	0.2	0.2
	OF1	–	–	–	–	–	–	–	–	–	0.1	–
[O III] λ5007	BBC	0.6	0.4	0.1	0.3	0.5	0.7	–	–	–	–	–
	RBC	0.1		0.2	0.3	–	–	–	–	–	–	–
	MC	–	–	–	–	–	–	0.5	0.4	0.4	0.3	0.3
	OF1	–	–	–	–	–	–	–	–	–	(0.1)	–
[N I] λ5199	BBC	0.4	0.3	(0.2)	0.2	(0.2)	–	–	–	–	–	–
	RBC	(0.2)	–	(0.2)	–	–	–	–	–	–	–	–
	MC	–	–	–	–	–	–	–	–	–	–	–
	OF1	–	–	–	–	–	–	–	–	–	–	–
[O I] λ6300	BBC	0.6	0.7	0.1	0.3	0.4	1.0	–	–	–	–	–
	RBC	0.3	(0.1)	0.4	0.5	0.2	–	–	–	–	–	–
	MC	–	–	–	–	–	–	0.9	0.4	0.4	0.4	0.5
	OF1	–	–	–	–	–	–	–	–	–	0.1	–
Hα λ6563	BBC	2.3	1.7	0.3	1.4	1.0	1.7	–	–	–	–	–
	RBC	1.0	0.2	0.7	0.8	0.5	–	–	–	–	–	–
	MC	–	–	–	–	–	–	1.2	1.9	3.1	0.8	1.0
	OF1	–	–	–	–	–	–	–	–	–	0.3	–
[N II] λ6583	BBC	2.5	2.7	0.4	1.6	2.0	2.1	–	–	–	–	–
	RBC	1.4	0.3	0.9	0.7	0.6	–	–	–	–	–	–
	MC	–	–	–	–	–	–	1.8	1.4	1.6	0.7	0.8
	OF1	–	–	–	–	–	–	–	–	–	0.3	–
[S II] λ6717	BBC	0.7	0.7	(0.1)	0.8	0.9	1.1	–	–	–	–	–
	RBC	0.5	(0.1)	0.5	0.4	0.2	–	–	–	–	–	–
	MC	–	–	–	–	–	–	0.6	0.7	0.5	0.4	0.5
	OF1	–	–	–	–	–	–	–	–	–	0.2	–
[S II] λ6731	BBC	0.8	0.8	0.1	(0.8)	0.9	1.6	–	–	–	–	–
	RBC	0.4	0.2	0.4	0.3	0.2	–	–	–	–	–	–
	MC	–	–	–	–	–	–	0.5	0.5	0.5	0.4	0.4
	OF1	–	–	–	–	–	–	–	–	–	0.2	–
Hα/Hβ	BBC	4.6	5.7	3.0	7.0	3.3	3.4	–	–	–	–	–
	RBC	10.0	–	7.0	4.0	–	1.8	–	–	–	–	–
	MC	–	–	–	–	–	–	4.0	6.3	7.7	4.0	5.0
	OF1	–	–	–	–	–	–	–	–	–	3.0	–
EW Hα	BBC	400	66	8	47	29	81	–	–	–	–	–
(Å)	RBC	110	8	27	24	12	–	–	–	–	–	–
	MC	–	–	–	–	–	–	7	32	104	21	22
	OF1	–	–	–	–	–	–	–	–	–	5	–
FWHM Hα	BBC	325	240	200	380	210	400	–	–	–	–	–
(km s^{-1})	RBC	275	240	280	252	200	–	–	–	–	–	–
	MC	–	–	–	–	–	–	235	190	110	320	250
	OF1	–	–	–	–	–	–	–	–	–	180	–

[a]The fluxes are given in units of 10^{-15} erg cm^{-2} s^{-1} (from 2D spectroscopy with a resolution of $\sim$100 km s^{-1}).
Column 2: emission-line components (Comp), where BBC, RBC, MC and OF1 are the blue bubble component, red bubble component, main component and outflow system 1, respectively.
P1, P2 and P3 mean positions 1, 2 and 3, of the fibre bundle (and fNNN is fibre-NNN).
The values between parentheses are data with low S/N.
MNuc, SNuc, MKnot, EBorder and WBorder denote the main nucleus, second nucleus, main knot, east border and west border, respectively.

that the properties found in this region could be associated with the presence of a satellite of the original galaxies that collided.

3.5.4 The kinematics of the extended complex of giant H II regions

Fig. 23(b) displays detailed 2D kinematic contour map, centred in the giant H II region complex (position 3), for the measured [N II] λ6583 emission line. This map was constructed partly for the single main component and partly for the red 'bubble' system.

We note the following properties of the VF (in this area):

(i) The H II region complex shows mainly redshifted velocities. However, there is also a very interesting blue feature: a

Table 7. Emission-line ratios of NGC 5514 (2D spectroscopy, individual/central fibres values).

Regions	Comp	log[O III]/Hβ^a	log[O I]/Hα^a	log[N II]/Hα^a	log[S IIs]/Hα^a	[S II]/[S II]^a	Spectral type
Bubble							
Knot 1							
Pos.1-fibre 126	BBC	0.08	−0.58	0.04	−0.19	0.88	L
	RBC	0.00	−0.52	0.15	−0.05	1.25	L
Knot 2a							
Pos.1-fibre 101	BBC	0.12	−0.39	0.20	−0.05	0.88	L
	RBC	–-	−0.30	0.18	0.18	(0.5)	L
Knot 2b							
Pos.1-fibre 47	BBC	0.00	−0.30	0.17	0.00	1.00	L
	RBC	0.30	−0.20	0.11	0.11	1.25	L
Knot 3a							
Pos.1-fibre 096	BBC	0.30	−0.67	0.06	0.06	1.00	L
	RBC	0.18	−0.20	−0.06	−0.12	1.00	L
Knot 3b							
Pos.1-fibre 103	BBC	0.22	−0.40	0.30	0.25	1.00	L
	RBC	–	−0.40	0.08	−0.10	1.00	L
Knot 4							
Pos.1-fibre 123	BBC	0.15	−0.23	0.09	0.00	1.21	L
Main nucleus							
Pos. 2-fibre 138	MC	0.10	−0.13	0.18	−0.04	1.20	L
Second nucleus							
Pos. 3-fibre 093	MC	0.13	−0.70	−0.13	−0.20	1.40	L
H II region complex							
Main knot (H II reg)							
Pos. 3-fibre68	MC	0.00	−0.89	−0.29	−0.49	1.07	L/H II
East-border (H II reg)							
Pos.3-fibre 048	MC	0.18	−0.30	−0.06	0.00	1.00	L
	OF1	0.00	−0.30	0.14	0.15	1.00	L
West-border (H II reg)							
Pos.3-fibre 101	MC	0.30	−0.47	0.00	0.12	1.25	L

^{a}[O III] λ5007; [O I] λ6300; [N II] λ6583; [S IIs] λλ6716+6731; [S II]/[S II] λ6716/λ6731.
Column 2: emission-line components (Comp), where BBC, RBC, MC and OF1 are the blue bubble component, red bubble component, main component and outflow system-1, respectively.
Column 8: for the spectral type, L and L/H II mean: LINERs, and transition objects, between LINERs and H II regions.
Pos.1, 2 and 3 mean positions 1, 2 and 3, of the fibre bundle.
The values between parentheses are data with low S/N.

'circular' blue-shifted lobe, which is located close to the main ejection of the bubble. This circular lobe is probably associated with the interaction/superposition of the two main OF process (associated with the bubble and the H II complex).

We note that this 'circular' structure was also observed in the ELR map of [S II]λ 6717 + 31/Hα (see Section 3.6.3), however this feature was not detected in the [N II] λ6583/Hα ELR map. This result confirms that the [S II] emission line is one of the best tracers of OF + shock processes.

(ii) For the weak OF components detected at the border of this H II region complex, the following mean values of velocities were measured: $V_{\rm OF\,blue} = (-240 \pm 25)$ km s^{-1} and $V_{\rm OF\,red} = (+100 \pm 30)$ km s^{-1}, in relation to the main components.

3.6 Mapping the emission-line ratios and widths (2D spectroscopy)

From 2D spectroscopic data, which cover practically the main structures of the main body, we measured the fluxes and FWHM of the ELC in order to investigate the structure of ionization and physical conditions of the gas.

These emission-line ratio maps were constructed using the techniques described in Section 2.6, and using the main result of the study of multiple ELCs (Section 3.4). In particular, these maps were generated with the same components already included in the kinematic maps: mainly the blue bubble system (inside the bubble), the red bubble component (in the knots and the south-east area of the shell), and the single main-body component in the remaining regions.

A first and general study of the emission-line ratios in NGC 5514 was performed using the 'standard' diagnostic diagrams of Veilleux & Osterbrock (1987). Fig. 24 depicts the values of ELRs (obtained from Tables 5 and 7) for the bubble, the nuclei and selected areas of the complex of H II regions. These plots show, for these structures, mainly LINER and transition LINER/H II properties. These LINER characteristics will be studied in detail in the next subsections.

3.6.1 The emission-line ratios and widths of the supergiant galactic bubble region

Fig. 25 displays detailed 2D contour maps for position 1 (16.4 × 12.3 arcsec^2, with 0.9-arcsec spatial sampling) for the ELRs:

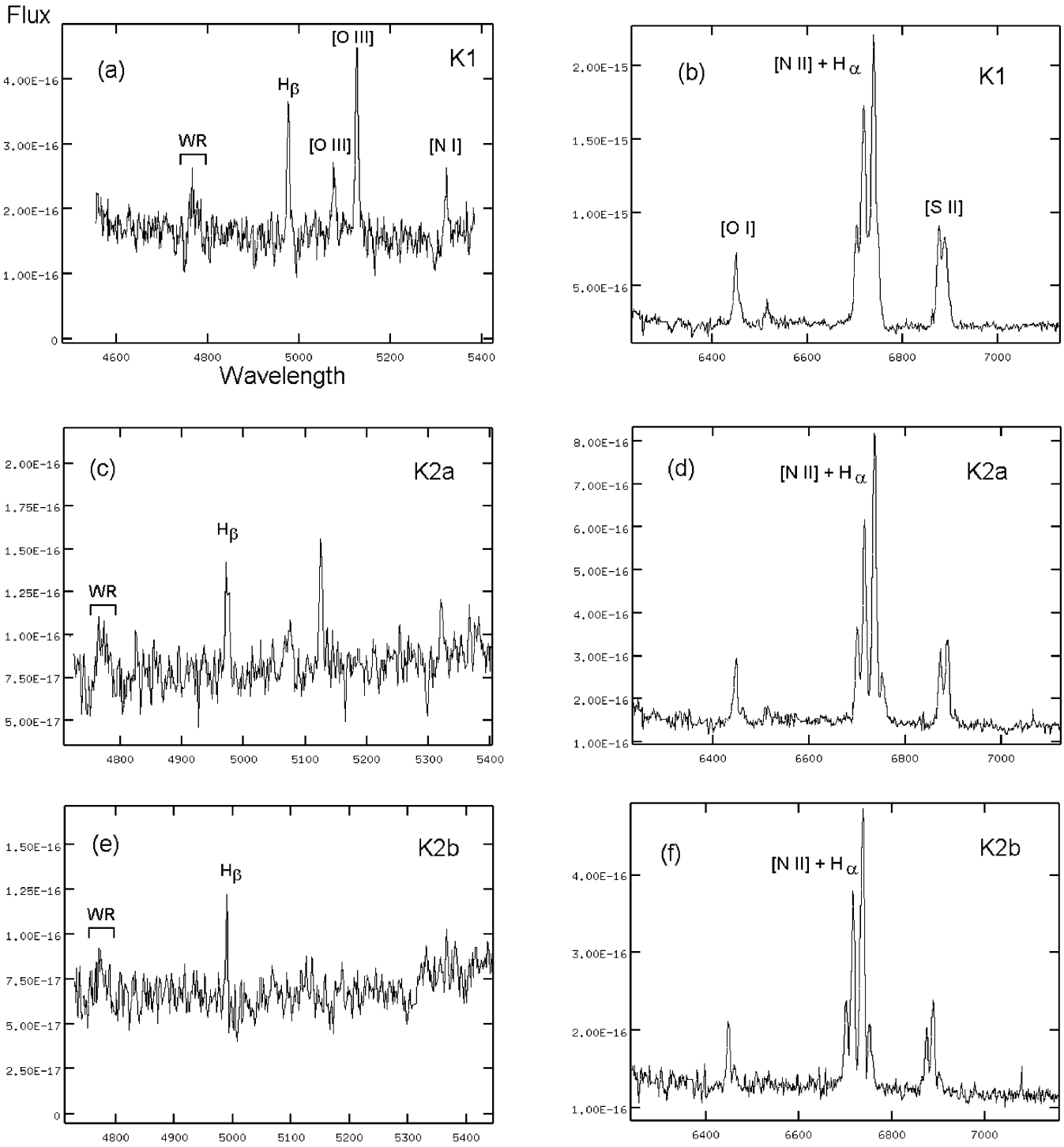

Figure 12. WHT + INTEGRAL 2D spectra of the main knots of the bubble in the blue and red wavelength regions.

[N II] λ6583/Hα, [S II] λ 6717 + 31/Hα, and the FWHM of the [N II] λ6583 emission line.

Fig. 25 and Tables 5 and 7 show interesting features and data. We note the following:

(i) The [N II] λ6583/Hα 2D map (Fig. 25a) shows, in 100 per cent of the galactic bubble, very high values, i.e. [N II] λ6583/Hα > 1. This result, obtained from the 2D map, was verified using the individual spectrum of each fibre.

(ii) The [S II] λ 6717 + 31/Hα 2D map (Fig. 25b) also shows, in ∼100 per cent of the galactic bubble, high values of the ratio [S II] λ6717 + 31/Hα > 0.8, thus confirming that these high values of the [S II]/Hα and [N II]/Hα ratios could be associated mainly with the effects of shock ionization in the outflowing gas (Heckman 1980;

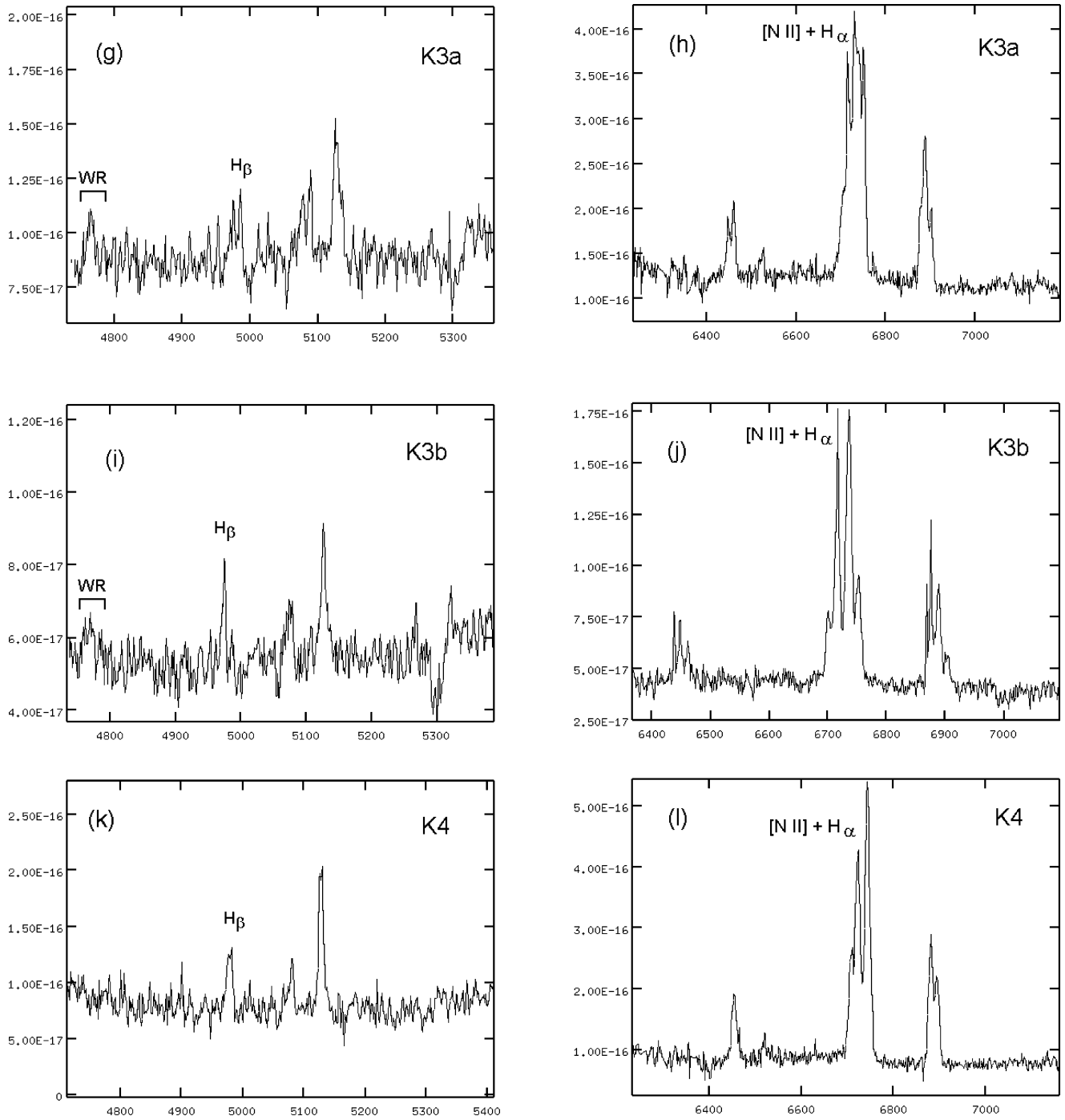

Figure 12 – *continued*

Heckman et al. 1987, 1990; Dopita 1994; Dopita & Sutherland 1995; Heckman 1996).

(iii) In the line diagnostic diagram [O I] λ6300/Hα versus [S II] λ6717 + 31/Hα (Heckman et al. 1990), these values are also consistent with ionization by shock heating.

We note that the [O I] λ6300/Hα and [O III] λ5007/Hβ maps depict a clear lobe located between the position of knots 1 and 4.

(iv) The FWHM–[N II] λ6583 2D map shows high values for the bubble area, in the range 300–600 km s^{-1}.

Therefore, in the galactic bubble of NGC 5514 these INTEGRAL 2D emission-line ratio maps show a very interesting result: mainly LINER properties associated with an ionization process produced mainly by shock heating in a large-scale OF event were detected (see Section 4.3).

3.6.2 The emission-line ratios and widths of the region of the nuclei

Fig. 26 displays detailed 2D maps (for position 2), for the emission-line ratios [N II] λ6583/Hα, [S II] λ 6717 + 31/Hα, and the FWHM of the [N II] λ6583 emission line. These maps were constructed mostly for the main component and for the red bubble component (in the ejection area).

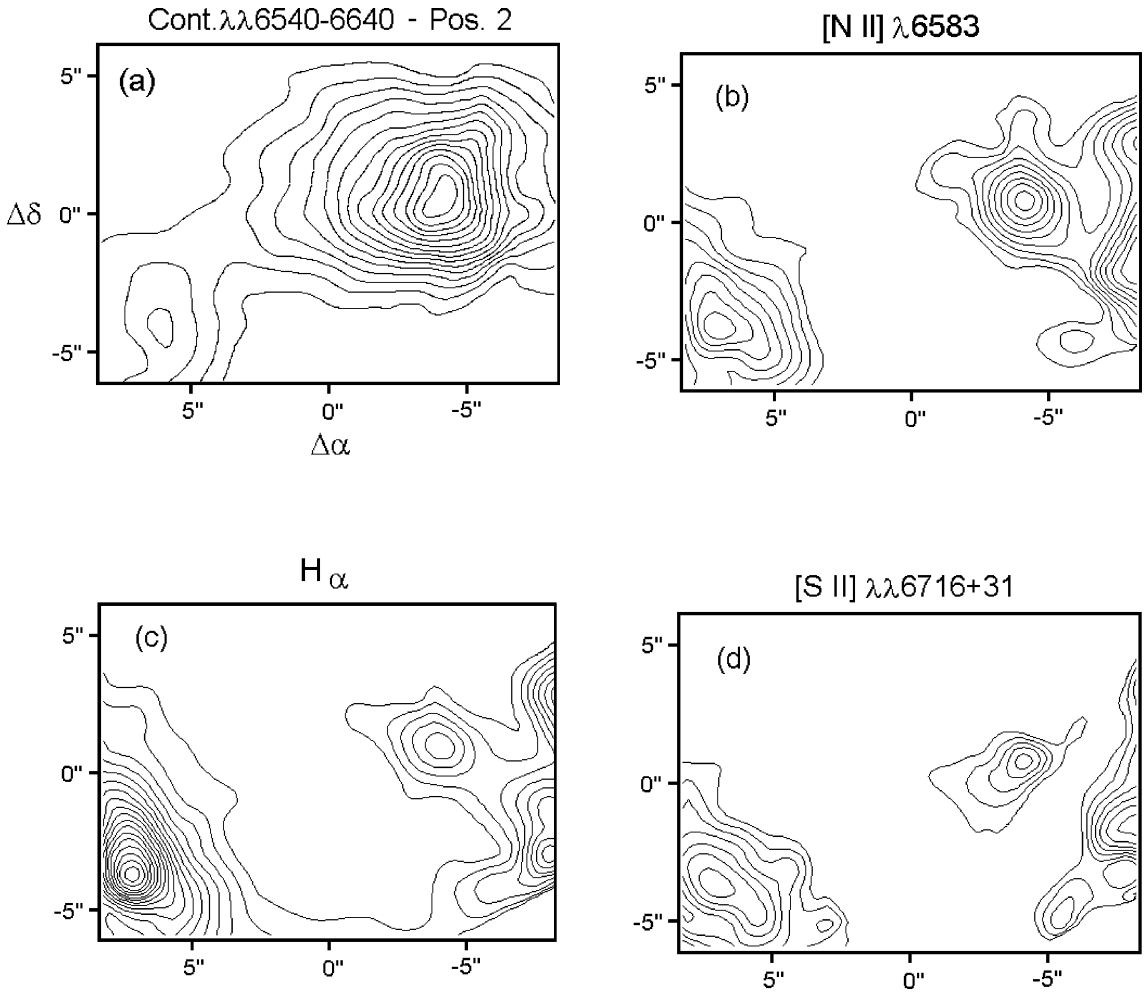

Figure 13. WHT + INTEGRAL maps of the nuclei region of NGC 5514 (position 2) for (a) a narrow continuum adjacent to Hα; (b), (c) and (d) pure [N II], Hα, and [S II] emission lines, respectively (the continuum was subtracted). The position of the centre of the fibre bundle was defined as the zero (0,0) value. North is up, and east to the left.

Fig. 26 and Tables 5 and 7 show the following main features and data:

(i) In the main nucleus the emission-line ratios show the following mean values: [N II] λ6583/Hα = 1.70, [S II] λ6717 + 31/Hα = 0.95, [O I] λ6300/Hα = 0.71, and [O III] λ5007/Hβ = 2.00. In general, these are typical values of emission-line ratios of LINERs associated with shock heating (Heckman et al. 1990; Dopita & Sutherland 1995).

In the [O I] λ6300/Hα versus [N II] λ6583/Hα diagram, the emission-line ratios of the main nucleus of NGC 5514 are consistent with LINERs and shock-heating regions (Heckman 1987).

For this nucleus, the FWHM–[N II] λ6583 2D map shows values in the range 230–250 km s^{-1}.

(ii) In the second nucleus the emission-line ratios show the following mean values: [N II] λ6583/Hα = 0.53, [S II] λ6717 + 31/Hα = 0.48, [O I] λ6300/Hα = 0.14, and [O III] λ5007/Hβ = 0.90. These values are consistent with those of transition objects, between LINER and H II regions (Ho 1996; Barth & Shields 2000).

For the second nucleus, the FWHM–[N II] λ6583 2D map shows low values, in the range 150–180 km s^{-1}.

Thus, both nuclei show emission-line properties and FWHM values consistent with LINER processes associated with OF + shocks events (plus a contribution of H II regions, in the case of the second nucleus).

3.6.3 The emission-line ratios and widths of the extended complex of giant H II regions

Fig. 27 displays detailed 2D maps (for position 3), for the emission-line ratios [N II] λ6583/Hα, [S II]λ 6717 + 31/Hα, and the FWHM of the [N II] λ6583 emission line. These maps were constructed mainly for the single main-body component (and for the red 'bubble' system, in the area of the ejection).

Fig. 27 and Tables 5 and 7 show interesting features and data; and we note the following:

(i) In this area the emission-line ratio maps show – for the main ELC – the typical values of giant H II regions (Kennicutt et al. 1989; Terlevich et al. 1991; and references therein).

(ii) Probably the most interesting emission-line ratio feature in this area is the circular structure observed in [S II]/Hα associated with a similar OF structure (detected in the kinematic map of this area, Section 3.5.3), with a radius $r \sim 3$ kpc. We note that again the [S II] and the [S II]/Hα ratio are the best tracers of OF process (see Section 4.4, for a discussion of this point).

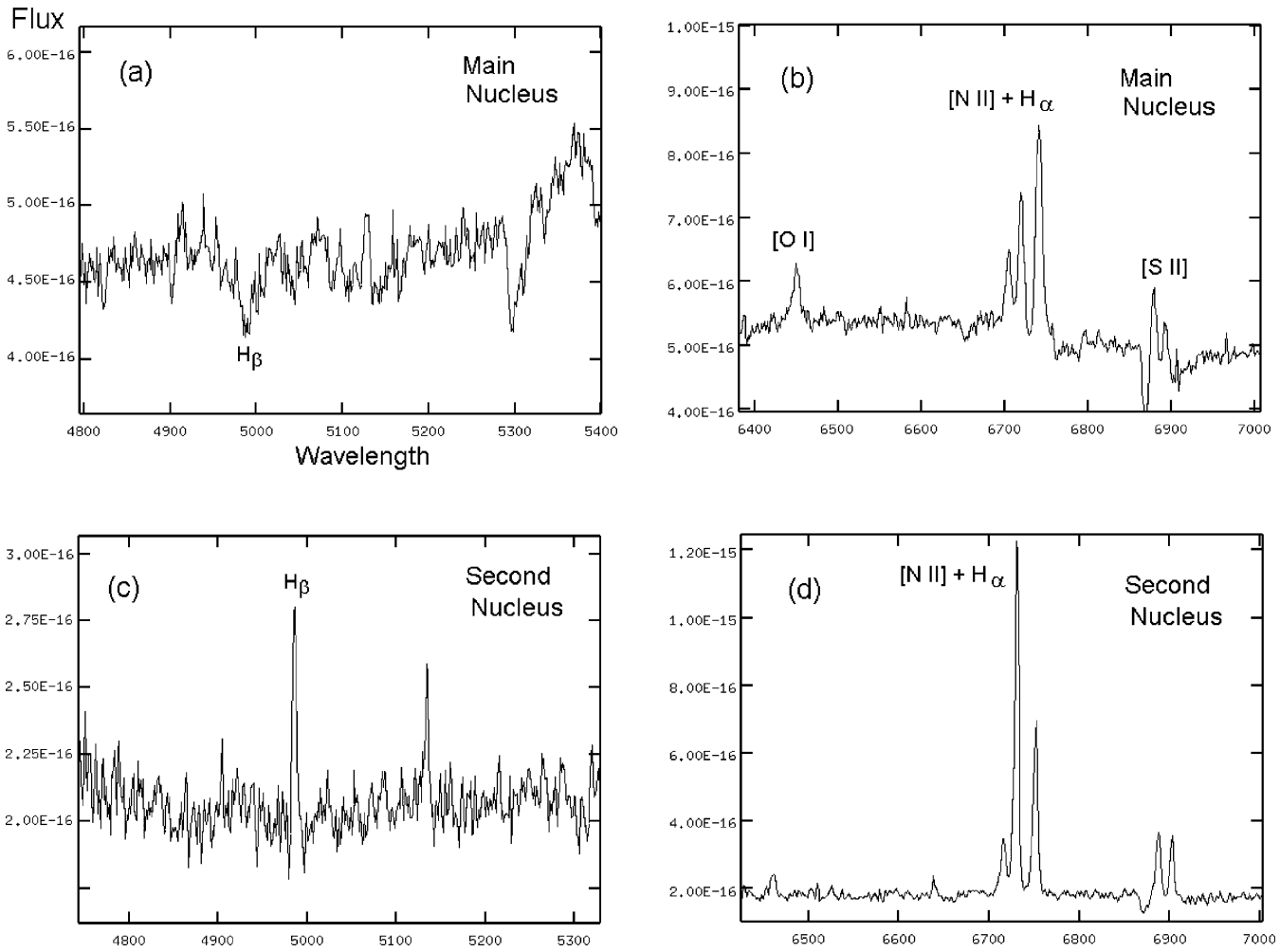

Figure 14. WHT + INTEGRAL spectra of the nuclei region in NGC 5514 (position 2) in the blue and red wavelength regions.

(iii) The area of emission-line peak (in the H II complex) shows emission-line ratios consistent with transition objects between LINER and H II regions (Ho 1996; Barth & Shields 2000).

This result is similar to that found for the second nucleus, and both are probably associated with OF processes, plus superposition with H II regions.

(iv) We have already depicted that at the border of this H II region complex, the spectra show weak OF components. These OF and the corresponding main components present LINER properties (see Tables 5 and 7).

(v) For this complex of H II regions low values of FWHM–[N II] λ6583 were found, in the range ∼150–240 km s^{-1}. However, at the border (of this complex, where we found OFs) the FWHM reaches values of 300–400 km s^{-1}.

In the next sections we will discuss mainly the properties of these two extranuclear starburst areas, with young outflow processes and LINER and LINER/H II properties (probably generated by the ongoing merger event).

4 DISCUSSION

In this section mainly the properties of the pre-merger process and the two extranuclear starbursts with outflow + supergalactic bubble and LINER activity will be discussed. In addition, the probable association between galactic winds and LINERs will be analysed. Finally, the properties and the role of the galactic winds in NGC 5514, IR mergers and IR QSOs will be considered.

4.1 The colliding galaxies in NGC 5514

4.1.1 The pre-merger process in NGC 5514

Fig. 28 shows a schematic diagram of the likely orbital plane geometry, of the NGC 5514 merger; indicating the probable location of our point of view. This diagram was performed according to the kinematics and morphological results obtained in Sections 3.1 and 3.5.

From Section 3 and FL88, the main properties of the original galaxies that collide can be summarized as follows: (i) the main galaxy has a diameter $d_1 \sim 50$ arcsec (∼24 kpc), mass $M_1 \sim 1.8 \times 10^{11}$ M$_\odot$, velocity $V_1 = 7280$ km s^{-1}, magnitude $V = 15.9$, colour $(B - V) = 1.2$, $(V - R) = 0.8$, $(V - I) = 1.6$ (for $r < 5$ arcsec); and (ii) the second galaxy has a $d_2 \sim 30$ arcsec (∼15 kpc), $M_2 \sim 0.9 \times 10^{11}$ M$_\odot$, $V_2 = 7680$ km s^{-1}, $V = 17.1$ mag, $(B - V) = 1.1$, $(V - R) = 0.8$, $(V - I) = 1.7$. These values are consistent with those measured in early Sa and Sb spiral galaxies. We note that in the NASA Extragalactic Data Base, the main and the second galaxies are associated with Sa (NGC 5514 – NED1) and Sb (NGC 5514 – NED2) spirals, respectively.

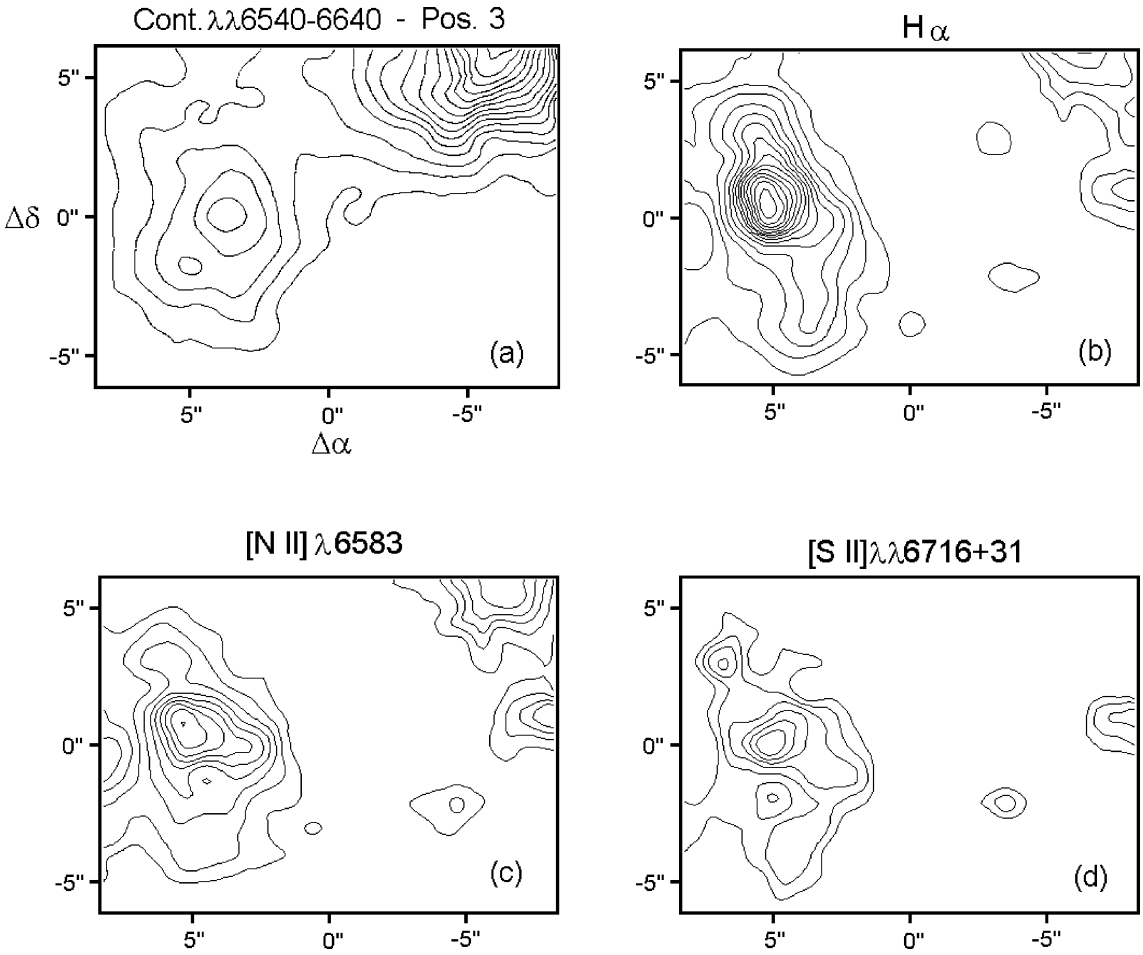

Figure 15. WHT + INTEGRAL maps of the complex H II region in NGC 5514 (position 3) for (a) a narrow continuum adjacent to Hα; (b), (c) and (d) pure Hα, [N II] and [S II] emission lines, respectively (the continuum was subtracted). The position of the centre of the fibre bundle was defined as the zero (0,0) value. North is up, and east to the left.

The size of the east tail in NGC 5514 (83 kpc) can give us a first estimation of the age of the merger. If an escape velocity of 100 km s^{-1} is assumed for the material in the tails (Colina, Lípari & Macchetto 1991; Murphy et al. 2001) a value of the age of $t_{\rm merger} \sim 8 \times 10^7$ yr was obtained.

A high percentage of the simulation of mergers was performed mainly for collision of equal-mass spirals and with disc/halo components (see, for references, Barnes & Hernquist 1992, 1996). However, there are several detailed simulations using different initial conditions in the merger process (including different values for the mass ratio). For example, Howard et al. (1993) published a Simulation Atlas of Tidal Features in Galaxies, with more than 1700 images, obtained from a wide range of initial conditions. On the other hand, Hernquist (1993), Mihos & Hernquist (1994a,b, 1996), Barnes & Hernquist (1996) and others already analysed the collisions between spirals with disc/halo/bulge components. Furthermore, Hernquist (1993) already suggested that mergers between bulge-dominant galaxies are the main type of collisions, that more probably could evolve into ellipticals. Using the atlas of Howard et al. (1993) we found that several types of unequal-mass galaxy collisions could generate a pre-merger morphology similar to that of NGC 5514, with only one bright tail. From this comparison, and as a new approximation, an age for the merger $t_{\rm merger} \leqslant 10^8$ yr (after the first encounter) was derived. Thus, these results suggest that this merger has an intermediate age.

This Simulation Atlas of Tidal Features in Galaxies also depicts interesting structures inside the main body of the mergers, associated with the formation and the beginning of the tidal tails. In Section 3.1, this type of structure was probably detected, superposed on the main body of this pre-merger.

FL88 suggested that this pre-merger is similar to the 'Antennae' and IRAS 23128–5919: i.e. similar to the collision between two giant spirals, with two bright tails. However, the results obtained in Section 3 suggest that the pre-merger is more similar to those systems that evolve from collision of bulge-dominant galaxies with unequal mass, which generate mainly one bright tail. In addition, it is interesting to note that in our Survey of Warm *IRAS* Galaxies we found an IR merger with very similar morphology to that observed in NGC 5514. More specifically, in IRAS 03109–5131 (de Grijp et al. Catalogue N–076, ESO 199–IG 023; $z_{\rm sys} = 0.078\,23$, $L_{\rm IR[8-1000\ \mu m]} = 1.0 \times 10^{11}$ $L_\odot$, Lípari et al. 1991b) we also found a pre-merger system between two disc galaxies of unequal mass (with $M_1/M_2 \sim 2$) that also shows only a bright tail. This system depicts two compact nuclei of different sizes ($R_1/R_2 \sim 2$) with a projected separation of $d \sim 11$ kpc, and both with Seyfert 2 properties (Lípari et al. 1991b; Fehmers et al. 1994). Thus, these two Seyfert nuclei could

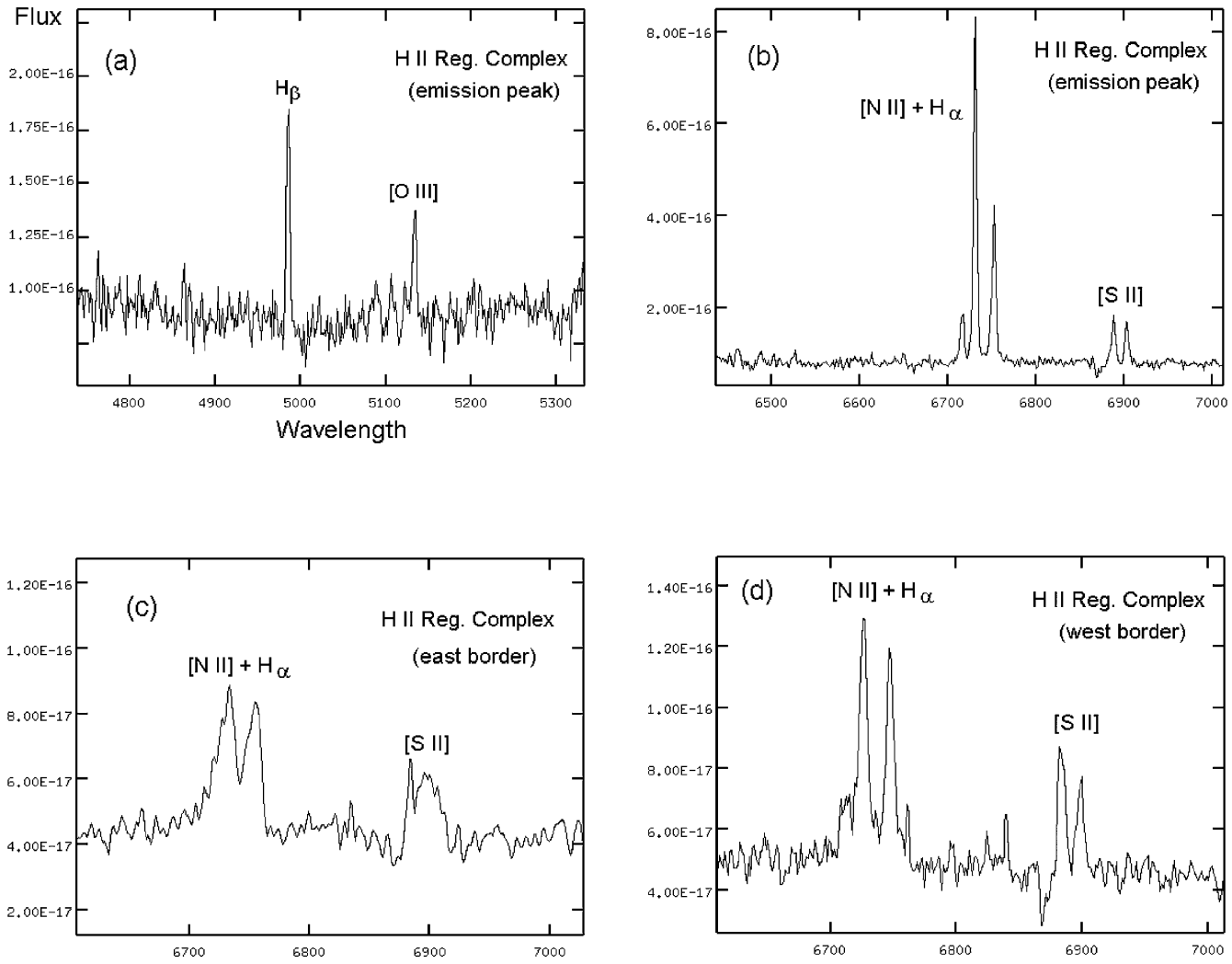

Figure 16. WHT + INTEGRAL spectra of the complex of H II region in NGC 5514 (position 3).

be generated in the early phases of the merger process (or these AGN were already formed in the original galaxies that collided, before the merger event). For NGC 5514, we found that at least two extranuclear starbursts were probably generated by the merger event, according mainly to the ages derived for the starbursts and the merger (see Sections 4.2 and 4.4). In addition, this proposition is also supported by observational and theoretical results, which suggest that the merger process frequently drives large amounts of molecular and ionized gas to the central regions leading to massive star formation events (see Section 1.1 for references).

4.1.2 A multiple-merger model for NGC 5514

Probably, the two spiral + bulge galaxies (that collide) have satellites, thus the multiple-merger scenario needs to be considered. In order to explore this type of event it is required to perform detailed numerical simulations, which are now in progress (Lípari et al., in preparation).

The first results of this kind of simulation suggest that the two massive spiral galaxies are the main components of the merger event, and that the satellite generally merges later (Taniguchi 2004, private communication). This type of composite-merger model (main plus minor mergers) could give a good explanation for the stretching of the isovelocity lines in the VF, detected at the north-east border of the field/mosaic (which is normally indicative of the presence of a significant concentration of mass).

In NGC 3256, we found that the best model or simulation that explains the interesting morphology observed (with three nuclei connected with three blue asymmetrical spiral arms) is a multiple-merger model between two gas-rich massive spiral + bulge galaxies plus a satellite (Lípari et al. 2000, 2004c).

4.1.3 The NGC 5514 small group of galaxies

It is important to study the properties of NGC 5514 in relation to NGC 5519, since these two systems are very close (in space and velocities) and could evolve in the future to a multiple merger. Probably, in the past the two original colliding galaxies (of NGC 5514) plus NGC 5519 formed a small group.

The Sa spiral galaxy NGC 5519 is located at 13.6 arcmin ∼390 kpc and at PA 130°, from NGC 5514. Their heliocentric velocity is $V = 7480 \pm 30$ km s^{-1} (FL88). Therefore, NGC 5514 and 5519 – with $\Delta V = 120$ km s^{-1} – are probably associated. We note that Mould et al. (1993, 1995) included NGC 5519 in their study of nearby groups and clusters of galaxies, within 100 Mpc.

In NGC 3256 we also found a similar result: i.e. this merger is part of a small group, which could evolve to a multiple merger (or even to a merger between mergers; Lípari et al. 2000).

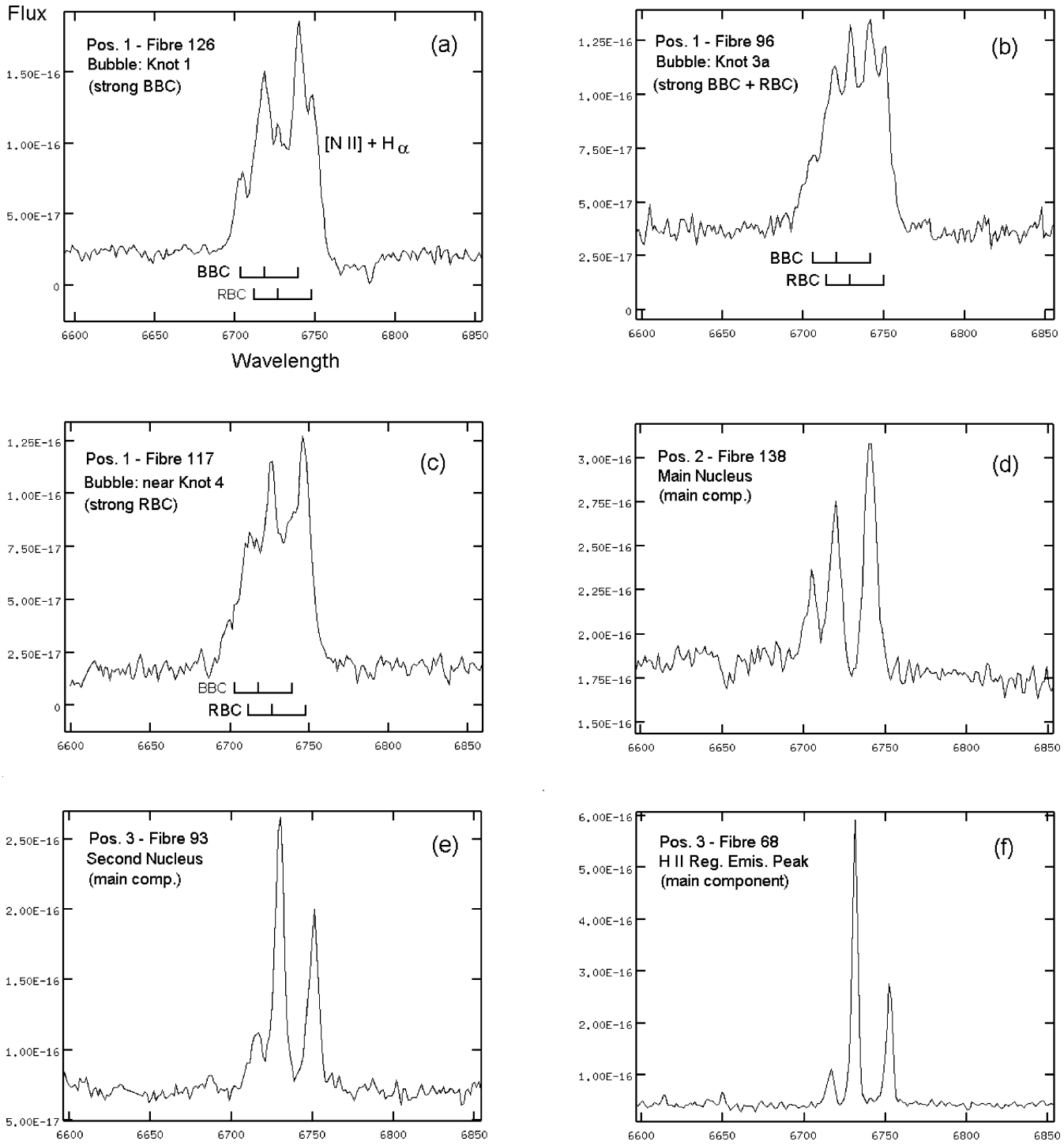

Figure 17. WHT + INTEGRAL spectra for individual fibres (in the wavelength region of the Hα + [N II] emission lines), showing examples of multiple emission-line components. The scales of flux are given in units of [erg × cm^{-2} × s^{-1} × Å^{-1}].

4.2 The starbursts in NGC 5514

In Section 3 two extranuclear areas with interesting starburst + OF + LINER properties, plus two nuclei with LINER plus shock characteristics, were found. These results will now be discussed.

(i) *Bubble region.* The extranuclear supergiant galactic bubble found in NGC 5514 is probably one of the few young bubbles clearly associated with a starburst, since this type of 'supergiant' object was previously detected mainly in the dense nuclear environment and in the post-blowout phase.

Thus the extranuclear starburst that originates the bubble, probably associated with knot 1, is at least similar to a powerful nuclear starburst. In Section 3, for this knot 1 a value of Hα luminosity $L_{\rm H\alpha} = 3.0 \times 10^{40}$ erg s^{-1} was measured. This luminosity value is consistent with those of strong starburst regions (Kennicutt et al. 1989).

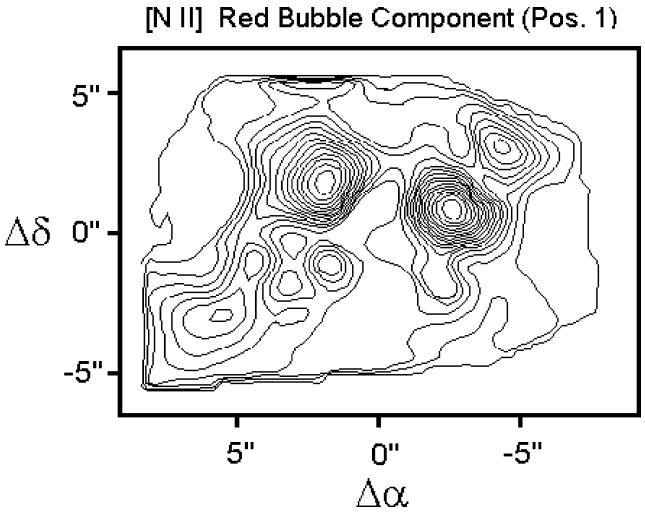

Figure 18. WHT + INTEGRAL map of the red bubble components (RBC), for the [N II] λ6583 emission line (at position 1). The centre of the fibre bundle defines the zero (0,0) position. North is up, and east to the left.

The presence of Wolf–Rayet features detected in three main knots of the bubble is clearly indicative of a large number of massive stars, probably in young SSCs with ages less than 6–8 × 10^6 yr (see Armus, Heckman & Miley 1988; Conti 1991). In Table 4, the fluxes and luminosities of the WR lines (measured in the bubble knots) were presented. This table shows medium/high WR luminosity values (between 1.4 × 10^{39} and 6.5 × 10^{39} erg s^{-1}), when they are compared with the range found even for WR galaxies (see Armus et al. 1988, their table 3; Conti 1991; Schaerer, Contini & Pindao 1999): 1.0 × 10^{38} (for Mrk 724), and 2.9 × 10^{41} (for IRAS 01003–2238) erg s^{-1}. It is interesting to note that one of the highest values of WR emission-line luminosity known was detected in an extreme velocity OF IR QSO.

In addition, it is important to discuss the general structure of the bubble, including the knots, in NGC 5514. The emission-line maps show: probably a central SSC or an association of SSCs, which are surrounded by knots/'arcs' of new star formation events (at the border of the shocked bubble). This type of structure was already observed in several nearby starbursts as '30 Dor, and the extranuclear bubble in NGC 6946' (Meaburn 1980; Larsen et al. 2002; Redman et al. 2003). Furthermore, this type of structure was detected even in starbursts in distant IR QSOS, as Mrk 231, and IRAS 01003–2238 (Lípari et al. 1994, 2003; Surace et al. 1998).

In general, we are investigating in IR mergers and IR QSOs – using WHT + INTEGRAL 2D maps – whether in these shells giant galactic shocks could generate new star formation episodes by compressing the ISM (see, for references, Larsen et al. 2002). These mechanisms could produce the 'dense shell of star-forming knots' detected in the arc of Mrk 231 (a BAL + Fe II IR merger/QSO), and also the chain/arc of 'extremely blue star-forming knots' in the Wolf–Rayet QSO IRAS 01003−2238 (both IR QSOs are systems with extreme velocity OF; Lípari et al. 1994, 2003).

Furthermore, at larger scale the presence of chain galaxies at high redshift was recently explained by mergers of subgalactic gas clumps plus SN explosions that generate GW + hyper-giant shells (of several hundred kpc), in which by gravitational instability intense star formation occurs. Then these systems collapse gravitationally into spheroid systems (Taniguchi & Shioya 2001). Thus, this is a similar process to that proposed for the origin of the external knots in the bubble of NGC 5514, but at megaparsec scales.

(ii) *Complex of H II regions*. In this extended complex there is clear evidence that the starburst and the OF process (which probably started to generate the cavity) are in a young/early state. More specifically, this complex is probably in the first starburst phase (0–3 × 10^6 yr), which is dominated by hot main-sequence stars with H II region spectra. This phase is also associated with the presence of dust and IR emission (Terlevich et al. 1993; Franco 2004, private

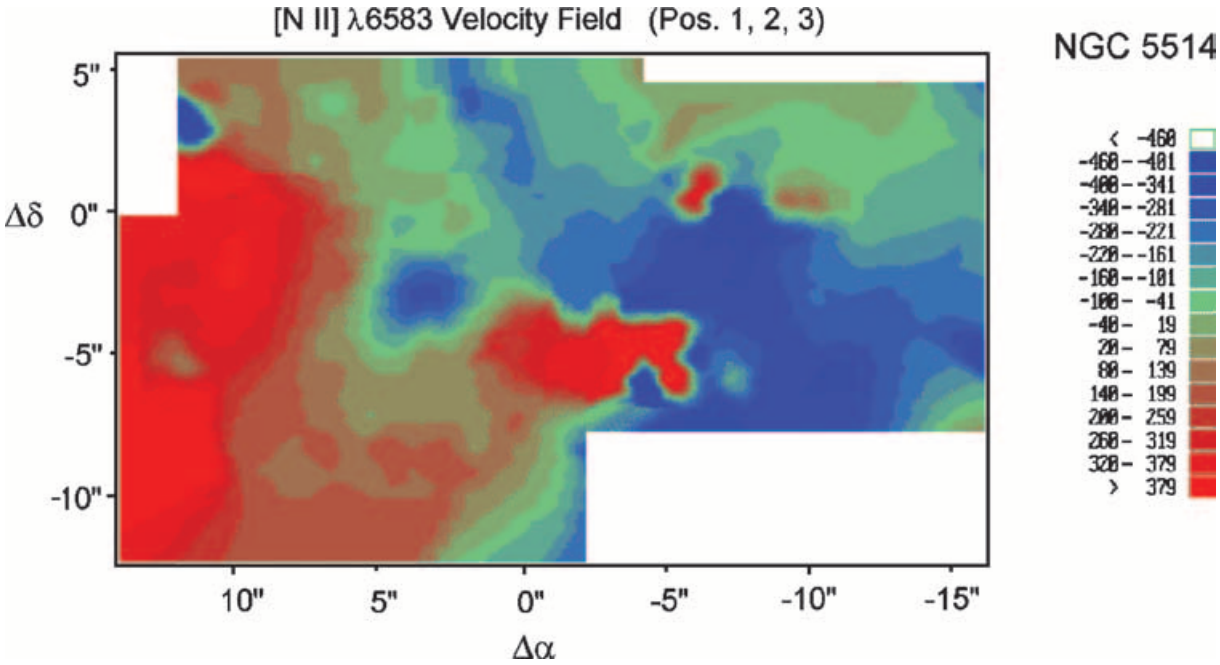

Figure 19. WHT + INTEGRAL velocity field mosaics, for the [N II] λ6583 emission line, of the ionized gas. The position of the main nucleus was defined as the zero (0,0) point. North is up, and east to the left. The scales and ranges of velocity are given in units of [km × s^{-1}].

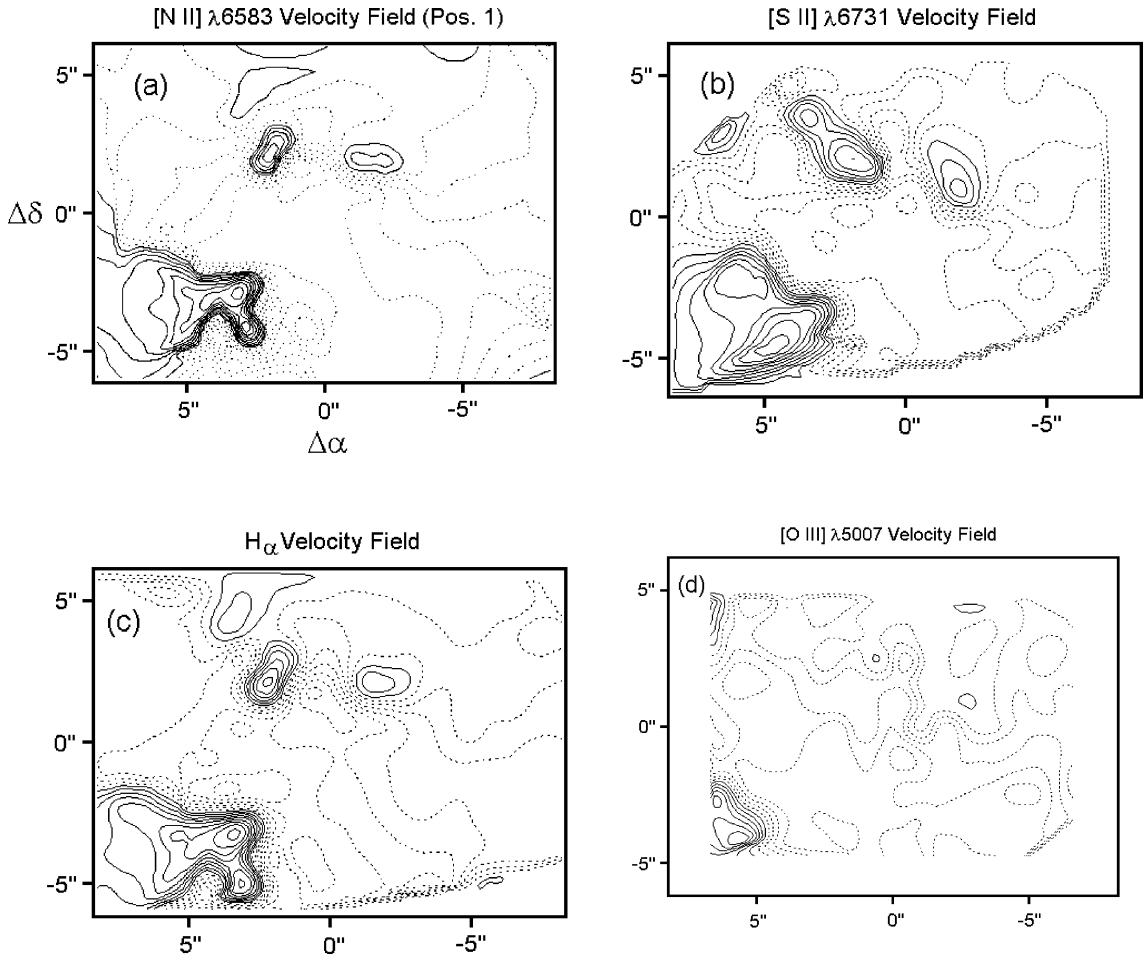

Figure 20. Contour of WHT + INTEGRAL emission-line velocity fields of the ionized gas, at position 1 (i.e. centred in the bubble), for: (a) [N II] λ6583; (b) [S II] λ6731; (c) Hα; (d) [O III] λ5007. The dashed lines show negative values. The centre of the fibre bundle defines the zero (0,0) position. The ranges of the contours are: (a) from −630 to 560, step 70 km s^{-1}; (b) from −515 to 600, step 70 km s^{-1}; (c) from −630 to 650, step 80 km s^{-1}; (d) from −400 to 370, step 70 km s^{-1}. North is up, and east to the left.

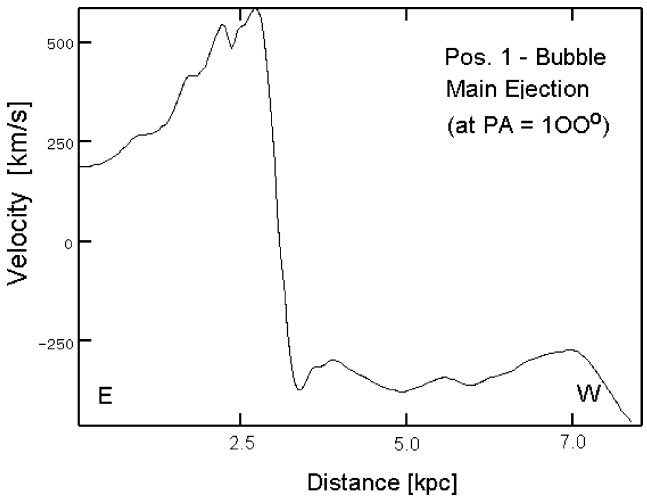

Figure 21. Profile of [N II] λ6583 velocity, through the main ejection at PA = 100° (obtained from the velocity field of Fig. 20a). The distance is from the east border of the INTEGRAL 2D field (position 1).

communication). This last point is due to the dust present in any star formation region and also to the large amount of dust synthesized by the most massive stars (during the η Carinae phase before becoming a WR star; Terlevich et al. 1993).

(iii) *Nuclei regions.* Since both nuclei depict values in the emission-line maps which are consistent with LINERs associated with OF/shock processes, their properties will be discussed in detail in the next section.

The starburst activity detected in this merger must have occurred at intermediate age in the history of the interaction, since the age of the pre-merger is $\sim 10^8$ yr, and the age of the older extranuclear starburst is 6–8 $\times$ 10^6 yr.

In the last few decades, special attention was devoted to studying the relation between starburst and merger processes, mainly in collision of equal-mass galaxies (i.e. in major mergers; Mihos & Hernquist 1994b, 1996; Barnes & Hernquist 1996). However, the process of starburst associated with mergers/collisions of unequal-mass galaxies is also an important and frequent event (Bernlohr 1993; Mihos & Hernquist 1994a; Taniguchi & Wada 1996). In particular, Bernlohr (1993) studied the starburst in 29 interacting galaxies, mainly with unequal mass (fitting synthetic starburst spectra to the observed one). He found that the starburst

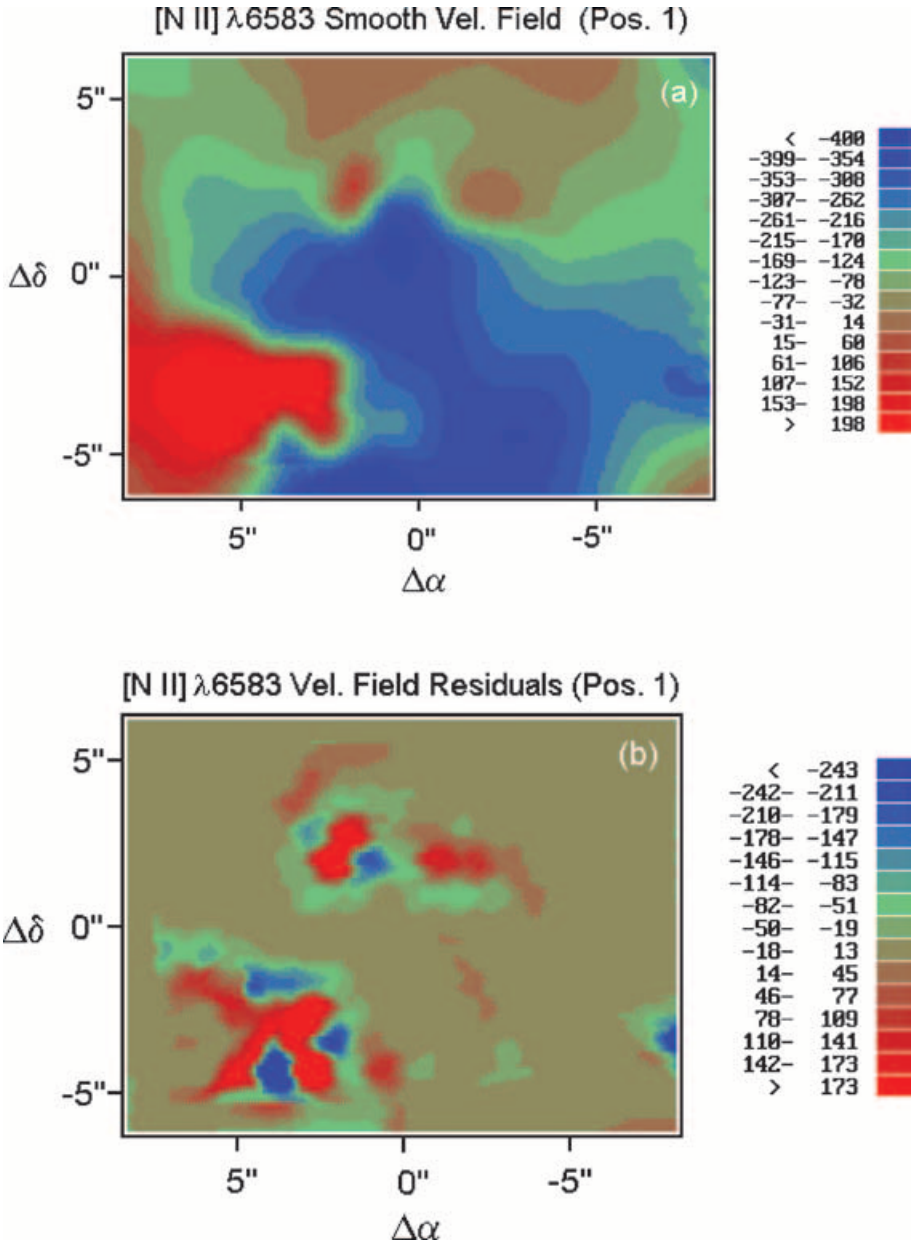

Figure 22. Smooth [N II] λ6583 velocity field (a) and the residuals of the subtraction of the smooth model from the observed [N II] λ6583 velocity field (b). North is up, and east to the left. The scales and ranges of velocity are given in units of [km × s^{-1}].

in the minor galaxies started earlier than in the major galaxies; and that the delay between the burst of the components can be significantly larger. In NGC 5514 it was found that both extranuclear starburst started almost at the same time, or even earlier in the major galaxy.

From detailed simulations of starbursts in major and minor mergers between disc/bulge/halo galaxies, Mihos & Hernquist (1994a,b, 1996) proposed that: (1) in mergers of bulge-dominant galaxies there is a significant increase in the star formation rate, in relation to mergers of disc/halo systems; (2) the central bulges act to stabilize the collision against radial inflow and associated starbursts, until the galaxies merged. In other words, they proposed – in the last point – that in mergers between bulge-dominant galaxies massive star formation occurred very late in the history of the interaction. Our 2D studies of starbursts and GWs in IR mergers/QSOs suggest that this proposition is probably true for the cases of NGC 2623, Mrk 231, NGC 3256, Arp 220, and others (Lípari et al. 1994, 2000, 2004a). For NGC 5514 (where we verified that this system is a collision of two bulge-dominant galaxies) two young extranuclear starburst processes were found with ages of ∼3–8 × 10^6 yr, then the starburst activity was delayed until well after the tails were launched, as would be expected for systems with substantial bulges. Probably the gas was concentrated in the central areas earlier.

In conclusion, this work presents the first, physical, morphological and kinematic evidence that the two strong extranuclear emission areas in NGC 5514 are associated with starbursts + OF + LINERs, with a supergiant galactic bubble. In Section 4.4 other properties of these starburst structures will be discussed.

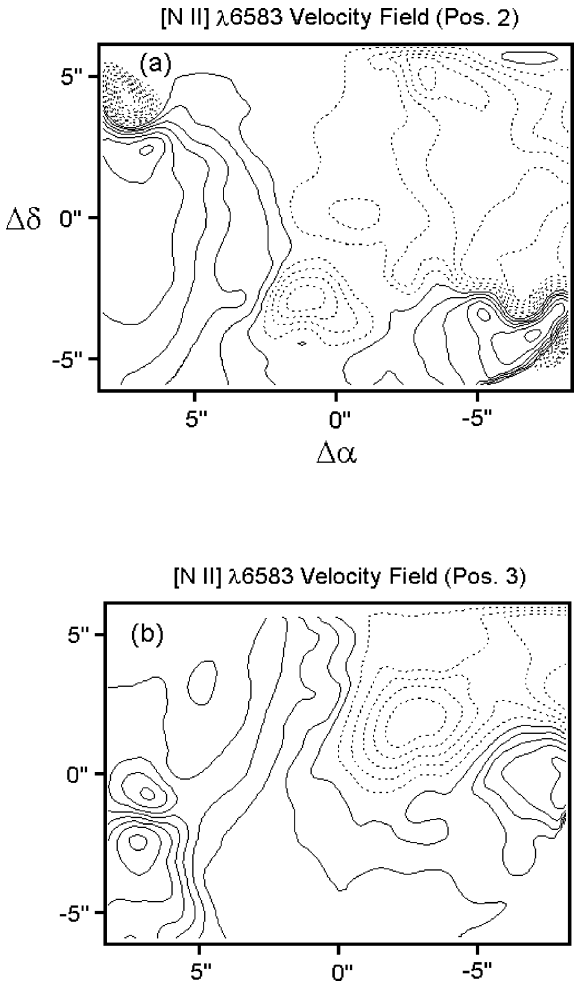

Figure 23. WHT + INTEGRAL emission-line velocity fields of the ionized gas, for: (a) [N II] λ6583 at position 2 (i.e. centred in the nuclei); (b) [N II] λ6583 at position 3 (i.e. centred in the H II region complex). The dashed lines show negative values. The centre of the fibre bundle defines the zero (0,0) position. The ranges of the contours are: (a) from −640 to 480, step 70 km s^{-1}; (b) from −375 to 605, step 70 km s^{-1}. North is up, and east to the left.

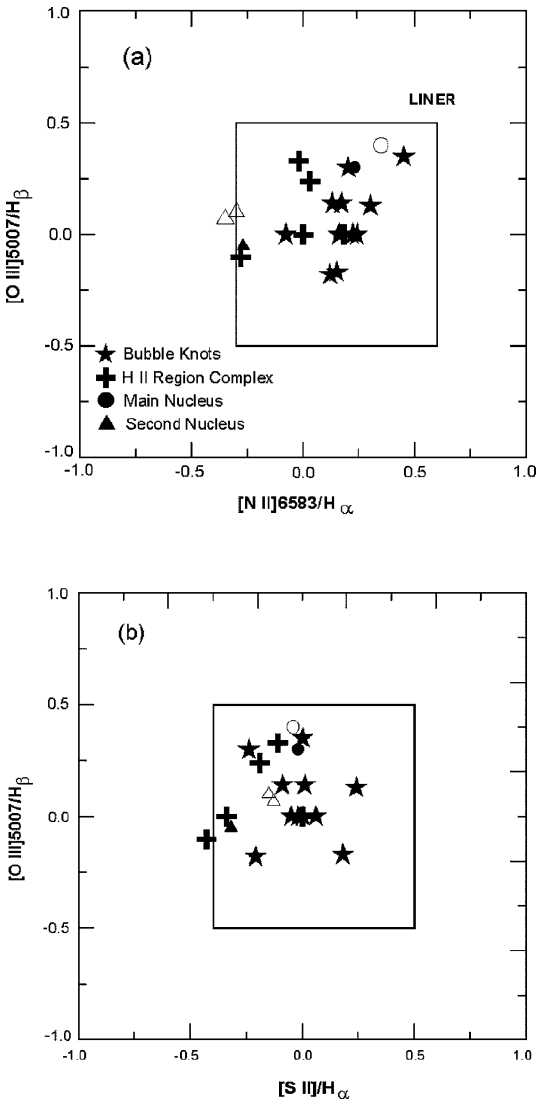

Figure 24. Emission-line ratio diagnostic diagram, of NGC 5514, for the data of 2D spectra of the knots in the bubble, the nuclei, and the east complex of H II regions (from Table 5). The open symbols show the emission-line ratios of 1D long-slit spectra (from Table 3). The regions of LINERs were adapted from the BPT diagrams published by Filippenko & Terlevich (1992) and Filippenko (1996).

4.3 LINERs in NGC 5514 and IR mergers/QSOs

4.3.1 LINER properties in the extranuclear starbursts and the nuclei in NGC 5514

The LINER properties found in the main nuclear and extranuclear regions of NGC 5514 (obtained from the emission-line maps/tables) will now be discussed.

(i) *Bubble region.* We found LINER characteristics in all the supergiant galactic bubble structures, in particular in all the knots and in the BBC and RBC emission-line systems (Tables 5 and 7).

Furthermore, in the bubble 100 per cent of the field shows very high [N II]/Hα and [S II]/Hα (>0.8). These ratios for the supergiant galactic bubble of NGC 5514 are located in the area of 'fast shock velocities' (of ∼300–500 km s^{-1}), in the superior end part of the [N II] λ6583/Hα versus [S II] λ 6717 + 31/Hα diagram (published by Dopita & Sutherland 1995, their fig. 3a). These results could be associated mainly to the effects of shock ionization when the outflowing gas collides with the ISM (Shull & McKee 1979; Heckman 1980; Heckman et al. 1987, 1990; Dopita 1994; Dopita & Sutherland 1995; Heckman 1996).

Similar results were obtained in the 2D studies of the bubble of NGC 3079 (Veilleux et al. 1994) and the OF nebula of NGC 2623 (Lípari et al. 2004a). They found that the ratios [N II] λ6583/Hα and [S II] λ6717 + 31/Hα are >1, in almost all the bubble and the nebula. They associated these results to the presence of large-scale OF + shocks.

Furthermore, it is important to note that Lutz (1990, 2004, private communication) found an interesting additional feature in NGC 5514: a strong radio continuum emission [about an order of magnitude above the radio–far-infrared (FIR) correlation], again mainly arising in the off-nuclear regions. This feature has implications for the interpretation in the LINER + shocks scenario. In particular, Lutz (1990) interpreted this as a signature of direct particle acceleration in galaxy-wide shocks (favouring this explanation over other

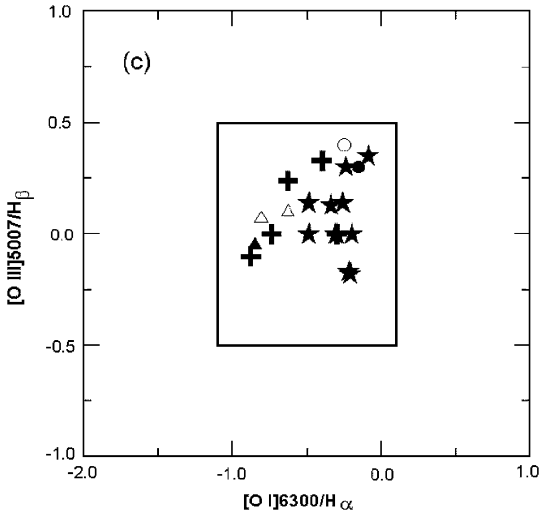

Figure 24 – *continued*

interpretations, like an unusual AGN or the signature of sharply decaying star formation with far-IR flux already down, radio lagging behind).

(ii) *Complex of H II regions.* At the border of this complex was also found OF and LINER properties (Sections 3.3, Tables 5 and 7). Again these LINER characteristics are probably associated with giant shocks in the compressed ISM (by the OF clouds).

For the emission peak in the main/central knot of this H II complex, the observed emission-line ratios (Tables 5 and 7) are consistent with transition objects between LINER and H II regions (Heckman 1996; Ho 1996). This transition characteristic, similar to that found for the second nucleus, is probably associated with OF process, plus superposition with H II regions.

(iii) *Main nucleus.* For this nuclear region, the optical emission-line maps and spectra show values consistent with a weak LINER/shocks plus an old stellar population. In addition, surveys at X-ray wavelengths found no evidence of a strong emitter or an AGN.

However, using the NRAO VLA Radio Sky Survey (Condon et al. 1998) and the *IRAS* Faint Source Catalogue (Moshier et al. 1992) for the galaxies in the Uppsala Catalogue, Condon, Cotton & Broderick (2002) derived for NGC 5514/UGC 9102 a value of $q = \log[F_{\rm FIR}/S_{1.4\,\rm GHz}] = 1.96$, where $F_{\rm FIR}$ and $S_{1.4\,\rm GHz}$ are the far-IR flux and the radio flux density, respectively. This low value of q suggests that the dominant energy source for the radio emission is from an AGN. They associated this value of q with the main spiral galaxy (Sa, NGC 5514 – NED1) of the merger.

These results suggest that the nuclear source of bolometric energy in the main nucleus is probably dominated by an AGN plus shocks. Thus, their LINER properties could also be associated mainly with AGN + shock processes.

(iv) *Second nucleus.* It is important to analyse the nature of this nucleus where properties of transition LINER/H II object were detected.

In particular, it is interesting to discuss the result obtained using Tables 5 and 7 for this second nucleus: if we study the properties of the emission peak, in only one fibre (of diameter of ∼1 arcsec ∼476 pc) mainly LINER characteristics were observed. However, if the circumnuclear region is included (in a diameter of ∼2 arcsec around this nucleus) their spectrum depicts transition LINER/H II

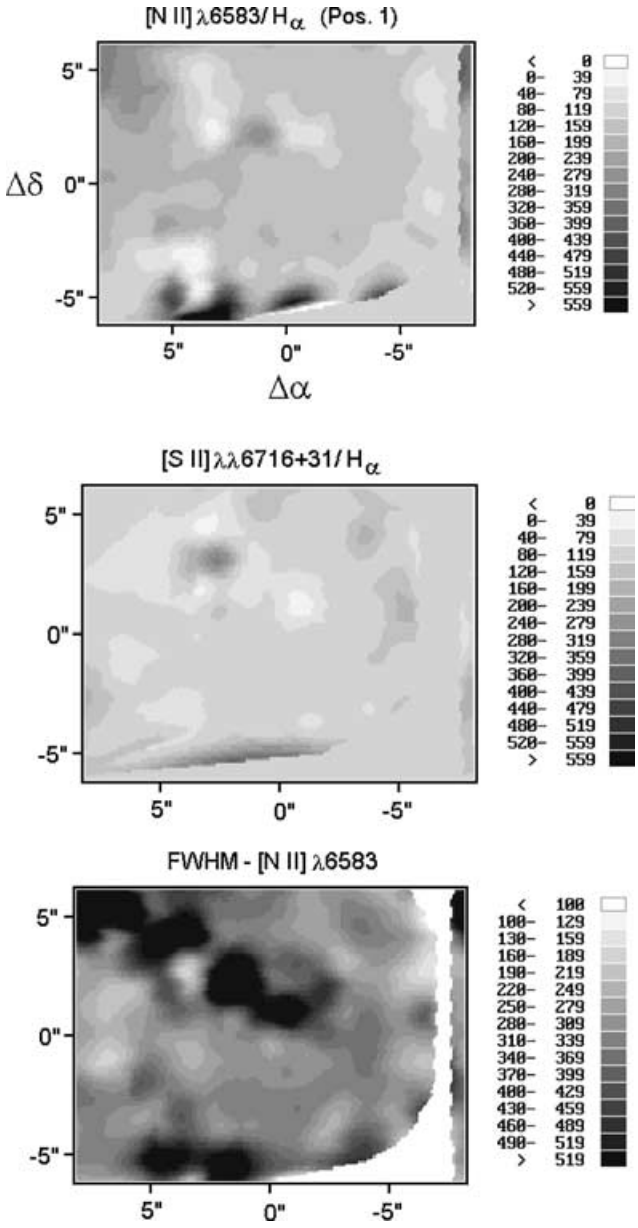

Figure 25. WHT + INTEGRAL maps of emission-line ratios and width of NGC 5514, for position 1 (i.e. centred in the bubble). The scale of the emission-line ratio includes a factor of 100. The FWHM are in units of km s^{-1}. The position of the centre of the fibre bundle was defined as the zero (0,0) value. North is up, and east to the left.

properties. Thus, for at least this case the transition characteristics could be associated mainly to a spatial superposition of LINER plus H II regions (see Heckman 1996; Ho 1996; Barth & Shields 2000).

Finally, we note that the ELR of both nuclei (Tables 5 and 7) are located in the [O I] λ6300/Hα versus [S II] λ6717 + 31/Hα diagram, in the same area as that found by Heckman et al. (1990) for the extranuclear region of a sample of 14 IR galaxies with galactic winds (their fig. 14). Furthermore, the ELR of both nuclei of NGC 5514 are located (in this plot) in the small area of Herbig–Haro objects and supernova remnants, i.e. 'the shocks region'.

Therefore, with the data available for the second nucleus (of NGC 5514), their LINER properties could be associated mainly to star formation and shock processes.

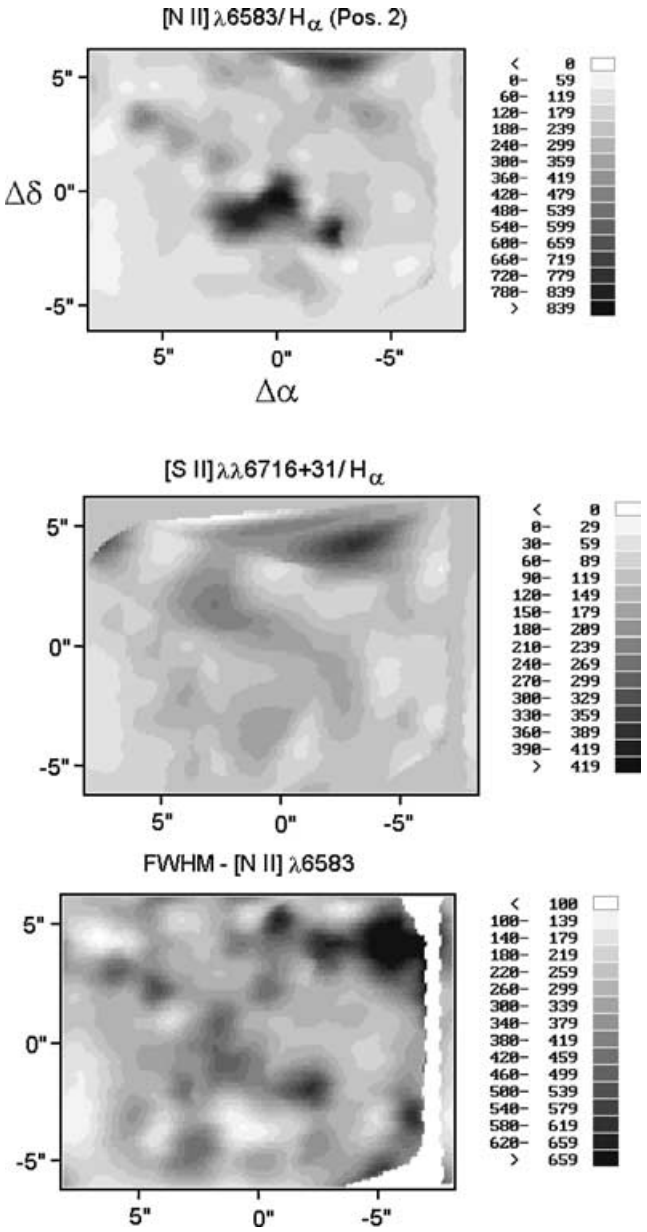

Figure 26. WHT + INTEGRAL maps of emission-line ratios and width of NGC 5514, for position 2 (i.e. centred in the nuclei regions). The scale of the emission-line ratio includes a factor of 100. The FWHM are in units of km s^{-1}. The position of the centre of the fibre bundle was defined as the zero (0,0) value. North is up, and east to the left.

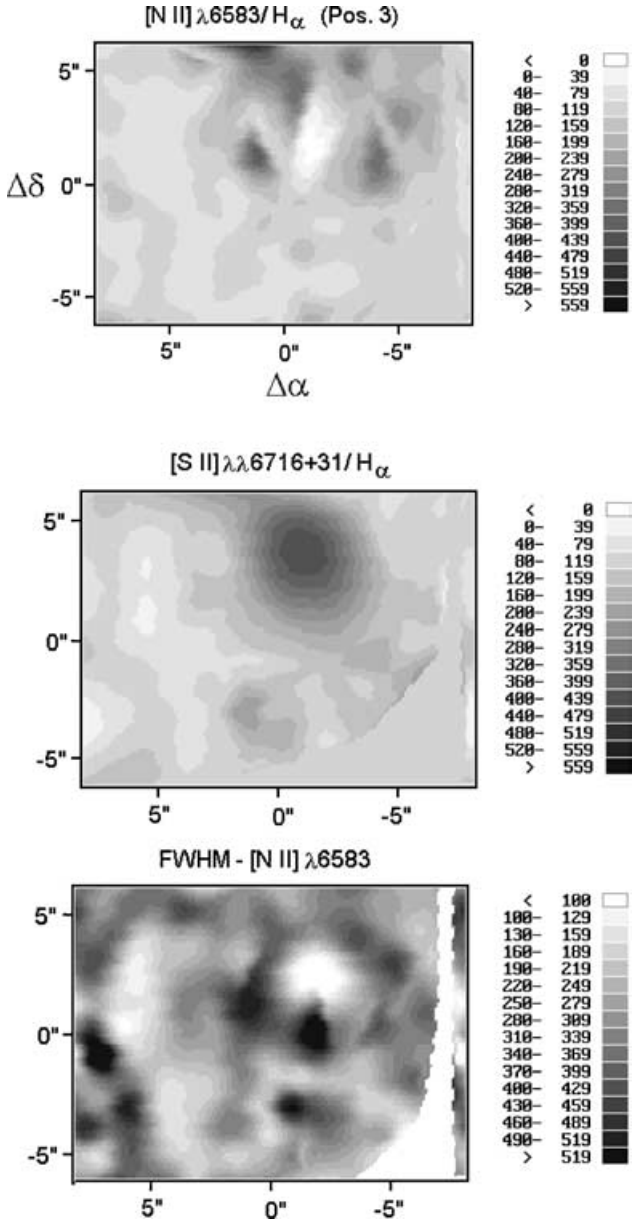

Figure 27. WHT + INTEGRAL maps of emission-line ratios and width, for position 3 (i.e. centred in the complex of H II regions). The scale of the emission-line ratio includes a factor of 100. The FWHM are in units of km s^{-1}. The position of the centre of the fibre bundle was defined as the zero (0,0) value. North is up, and east to the left.

4.3.2 LINER properties associated with starburst and galactic winds in IR mergers/QSOs

In the present programme of 2D spectroscopic study of IR mergers and IR QSOs with galactic winds – and associated nebula or bubbles – we found a relatively high number of objects that have LINER properties, associated mainly with nuclear starburst and large-scale shocks (see Section 4.5 and Lípari et al. 2004a: their table 1). Furthermore, in NGC 5514 LINER properties in the nuclear regions, and very strong LINER activity in the extranuclear OF areas (Section 3) were observed.

In addition, this new result for NGC 5514 confirms an interesting previous result (obtained by Lípari et al. 2003, 2004a): mainly starbursts and LINERs are the sources of ionization in 'low velocity OF' IR mergers (LVOF, $V_{\rm LVOF} < 700\,{\rm km\,s^{-1}}$; Lípari et al. 2003, 2004a). According to the results obtained from this and previous detailed 2D spectroscopic studies of NGC 5514, 2623, 3256 and similar IR mergers, we already suggested that three processes could be the main sources of ionization and energy in these LVOF IR systems: (1) in nuclear and circumnuclear regions, the gas could be photoionized by the diffuse radiation field of metal-rich dusty starbursts, showing 'starburst or LINER' spectra (Terlevich & Melnick 1985; Filippenko & Terlevich 1992; Shields 1992; Heckman 1996; Ho 1996; Wang et al. 1997; Barth & Shields 2000); (2) in very extended areas, the source of ionization could be large-scale shocks in clouds accelerated outwards by starbursts + galactic winds, which produce LINER properties, especially at the periphery of the OF areas (Heckman 1987, 1996; Heckman et al. 1987, 1990; McCarthy,

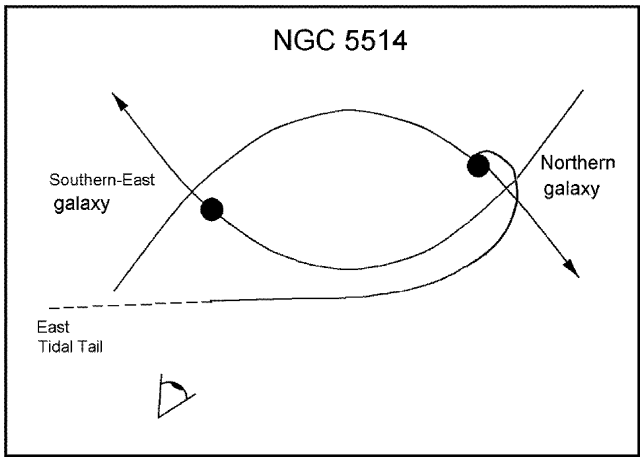

Figure 28. Schematic diagram of the likely orbital plane geometry of the NGC 5514 merger (adapted from Murphy et al. 2001).

Heckman & van Breugel 1987; Lípari et al., in preparation); and (3) in several regions, including the nuclei, these two previous processes could be superposed. These subclasses of LINER associated with nuclear starburst + shocks, and with large-scale shocks, are clearly different from the 'AGN-related LINER' subgroup (Heckman 1996; Ho 1996; Wang et al. 1997).

The new results obtained from our programme could help us to understand the nature of LINERs and the strong IR emission, in some LIRGs and ULIRGs, where LINERs are almost the dominant spectral types (∼30–40 per cent; Sanders & Mirabel 1996, their fig. 5). Specifically, our results are consistent with those of Lutz, Veilleux & Genzel (1999) and Veilleux, Kim & Sanders (1999): they suggested that the nature of LINERs in LIRGs and ULIRGs is associated mainly with starbursts and shocks originated in galactic winds.

4.4 Galactic winds in NGC 5514

4.4.1 The supergiant galactic bubble

Fig. 29 depicts a schematic diagram of the supergiant galactic bubble. This plot shows the emission-line morphology plus the main ejections detected in NGC 5514 (Sections 3.5 and 3.3). We note that these results are in agreement with the general scenario proposed for the OF process by hydrodynamic GW models (e.g. Suchkov et al. 1994; Strickland & Stevens 2000). In particular, the results obtained in Section 3 agree with the 'pre-blowout' or rupture phase of the bubble (see the summary of GW phases, presented in Section 1.2).

Following the study of the superbubble in NGC 3079 (Veilleux et al. 1994) the dynamical time-scale of the bubble in NGC 5514 was derived, using the relation

$$t_{\rm dyn} = 1.0 \times 10^6 \; R_{\rm bubble,\ kpc} \; V^{-1}_{\rm bubble,\ 1000} \ {\rm yr}$$

where $R_{\rm bubble,\ kpc}$ and $V^{-1}_{\rm bubble,\ 1000}$ are the linear dimension of the bubble and the velocity of the entrained material, in units of kpc and 1000 km s^{-1}, respectively. A value of $t_{\rm dyn} \sim 8.5 \times 10^6$ yr was obtained.

A second age can be estimated if the bubble has not reached the blowout phase (as the case of NGC 5514), and can be approximately like an adiabatic structure with a radiative shell that expands through a uniform medium (Koo & McKee 1992). Then by using the relations for the radius and expansion velocity of the shell (from Castor et al. 1975; Veilleux et al. 1994) they derived

$$t_{\rm bubble} = 6.0 \times 10^5 \; R_{\rm bubble,\ kpc} \; V^{-1}_{\rm bubble,\ 1000} \ {\rm yr}$$

and a value $t_{\rm bubble} \sim 5.2 \times 10^6$ yr was found, very similar to the dynamical age. This derived age for the bubble allows the formation of the SSCs in the external/compact knots, with ages less than 6×10^6 yr.

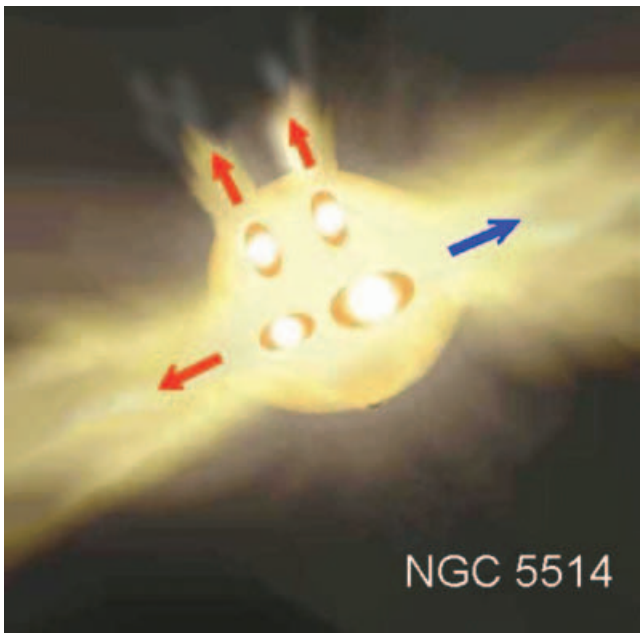

Figure 29. Schematic diagram for the outflow geometry in the galactic bubble of NGC 5514 (adapted from Richichi & Paresce 2003). The line of sight to the system is approximately in the foreground of the drawing. The axis of the bubble forms an angle of approximately 45° (a mean value) with the line of sight. The west (right) side of the bubble is probably the nearest part, since we detected in this area a blueshifted or approaching OF/ejection (see the text).

In Section 3.5 the following OF velocities were measured close to the centre of this supergiant galactic bubble: $V_{\rm OF\,blue} = (-320 \pm 20)$ km s^{-1} and $V_{\rm OF\,red} = (+265 \pm 25)$ km s^{-1}. These velocities measured for the strong blue and red bubble components are consistent with expansion of the shell, and together with the clear ejections suggest that the OF will reach the blowout phase. The velocities measured in the ejection areas and even for the expansion of the shell are higher than or similar to the escape velocity in extranuclear regions (e.g. the escape velocity for the solar neighbourhood is $V_{\rm escape} = 350$ km s^{-1}; Binney & Tremaine 1987).

From the 2D spectra, for the blue and red bubble emission-line components a Hα flux of 1.1×10^{-13} erg cm^{-2} s^{-1} was derived. Assuming a mean value $E(B-V) = 0.44$ (from Tables 4 and 6) and using the relations given by Colina et al. (1991) and Mendes de Olivera et al. (1998) we found a value for the ionized gas mass, in the OF, of 4.2×10^6 M$_\odot$. In IR galaxies, different studies have found that the range of ionized gas mass ejected by the OF is $\sim 10^6$ –10^8 M$_\odot$ (Colina et al. 1991; Veilleux et al. 1994; Lípari et al. 2004a). Using the value of ionized gas mass, we derived the kinetic energy of the OF, $E_{\rm KIN-OF} \sim 0.5 \times M_{\rm OF-IG} \times \langle V_{\rm OF} \rangle^2 = 4.0 \times 10^{54}$ erg. This result is within the range obtained for the OF in luminous IR mergers, M82 and NGC 3079 (Lípari et al. 2004a).

Finally, it is important to note that from our 2D INTEGRAL study (Sections 3.3 and 3.5) direct evidence of a very high number of massive WR stars was found, in the OF knots of the NGC 5514

broken bubble. These WR stars are progenitors of core-collapse super- or even hypernovae. Thus, as suggested by theoretical work, SNe from massive progenitors are probably the objects that generated the rupture phase of the bubble, in the OF knots (for references see Section 4.5.2).

4.4.2 The outflow in the H II region complex

The general morphology and the spectra of this H II region complex clearly suggest that the star formation and the OF process are very young: with an age less than 3–4 $\times$ 10^6 yr (i.e. in the first phase of the starburst process, which is dominated by hot main-sequence stars with H II region spectra; Terlevich et al. 1993).

In the external areas of the complex of H II regions, we derived for the OF a Hα flux of 2.0×10^{-14} erg cm^{-2} s^{-1} (which is $\sim$25 per cent of the total flux in this area). Assuming a mean value $E(B-V) = 0.48$ (from Tables 4 and 6) and using also the relations given by Colina et al. (1991) and Mendez de Olivera et al. (1998) a value for the ionized gas mass, in the OF, of 1.0×10^6 $M_\odot$ was found. Using this value of ionized gas mass, we derived for the kinetic energy of the OF, $E_{\rm KIN-OF} \sim 0.5 \times M_{\rm OF-IG} \times \langle V_{\rm OF} \rangle^2 = 0.8 \times 10^{54}$ erg.

In Section 3.5 for the weak OF components (detected at the border of this complex of H II regions), the following OF velocities were measured: $V_{\rm OF\,blue} = (-240 \pm 25)$ km s^{-1} and $V_{\rm OF\,red} = (+100 \pm 30)$ km s^{-1}. We note that this young OF process depicts some properties similar to those observed in the OF process associated with the supergiant galactic bubble (e.g. a major axis of $\sim$5 kpc, LINER + shocks properties at the border/shell, etc.). Thus, this young OF could generate a new giant galactic bubble, in NGC 5514. However, the Hα luminosity in the main knot (of this complex) is less – by almost one order of magnitude – than the luminosity in knot 1 of the bubble.

One of the more interesting features in this area is the circular structure observed in [S II]/Hα, and the velocity field map (see Sections 3.5 and 3.6). This structure is probably associated with the interaction of OF processes detected in this merger. Probably this OF – which we are looking at blushifted and face on – could be generated in the far side of the OF process detected in the west area. In other words, the west bubble could be the nearest part of a bipolar OF. This type of structure, with double bubble, was already detected in NGC 3079, 30 Dor, NGC 2782, 2623, etc. (Meaburn 1980; Ford et al. 1986; Jogee et al. 1998; Redman et al. 2003; Lípari et al. 2004a).

Finally, it is important to note another interesting result found in Section 3 (for NGC 5514) and in our programme (for NGC 3256 and 2623): the [S II] and [S II]/Hα are probably the best tracers of GW and OF processes. We recall that good evidence of shock processes and SN events (in ionized nebulae) is the intensity enhancement of low-excitation lines, in particular [S II] and [O I]. In fact, the [S II]/Hα and [O I]/Hα ratios have been used as the best tracer of shock ionization mechanisms (Heckman 1980; Canto 1984; Binette 1985; Heckman et al. 1990; Masegosa, Moles & del Olmo 1991; and others). Specifically, in Herbig–Haro objects the OFs and shock processes were detected mainly/first in [S II] emission and the [S II]/Hα ratio (Canto 1984). In IR mergers and IR QSOs, different workers already proposed that giant galactic shocks are associated with extreme starburst + galactic winds, induced by the merger events (Joseph & Wright 1985; Rieke et al. 1985; Heckman et al. 1987, 1990; Armus et al. 1988; Lípari et al. 1993, 1994, 2000, 2003, 2004a; Lutz et al. 1999; Veilleux et al. 1999).

4.5 Galactic winds in IR mergers and IR QSOs

Strong evidence of two extranuclear galactic winds in the IR merger NGC 5514, plus an AGN in the main nucleus, was found in this work. Thus this object is a new example of IR merger with composite activity: extreme starburst plus AGN. It is important to note that two of the main goals of our programme are to study this type of composite IR system, and the possible links – or evolutionary paths – among IR mergers, extreme starburst + GW, and AGN/QSOs. In this section these two main points are discussed. In addition, interesting results obtained from the last update of the data base of our programme are presented.

4.5.1 Galactic winds in IR mergers

The low-velocity OF (LVOF, $V_{\rm EVOF} < 700$ km s^{-1}) observed in the extranuclear starbursts of NGC 5514 is consistent with the results found in IR mergers with dominant massive starburst processes – e.g. in NGC 2623, 3256, 4039/38, and others – where mainly LVOF were detected (Lípari et al. 2000, 2003, 2004a). This fact also suggests the importance of studying, as a group, the general properties of these IR systems.

Lípari et al. (2004a) found that a high proportion of IR mergers develop galactic winds: at least $\sim$75 per cent. This interesting result was found comparing their data base of OF in IR mergers/QSOs with two samples of nearby IR mergers. Thus, this result strongly suggests, or confirms, that: (a) GWs are 'frequent events' in IR mergers; (b) extreme starbursts + GW and extreme IR emission could be simultaneous processes induced by merger events.

This last conclusion is also supported by a clear trend found in the plot of OF velocity versus log $L_{\rm IR}$ (for 28 IR mergers/QSOs with confirmed GW), in the sense that extreme OF velocities are detected only in extreme IR emitters (ULIRGs). The proposed explanation for this observed trend is that high values of OF velocity and $L_{\rm IR}$ are both associated mainly with the same process: 'starburst + QSO' events, probably induced by mergers (Lípari et al. 2004a).

4.5.2 Galactic winds in IR QSOs

In previous works we stressed the fact that it is important to study whether 'some' IR mergers (like NGC 5514) with starbursts and low-velocity OFs could evolve into IR QSOs with composite nuclear nature and extreme-velocity OF, or to bulge/elliptical galaxies. This possible evolutionary path is supported by several facts; in particular the presence of a correlation between the mass of the galactic bulge and the mass of a supermasive black hole candidate (or supermasive dark object; Kormendy & Richstone 1995; Laor 1998; Merrit & Ferrarese 2001) strongly suggests that the formation and evolution of bulges, supermasive black holes, and QSOs are physically related to each other (Kawakatu, Umemura & Mori 2003).

Recently, for IR QSOs we found the following:

(i) extreme-velocity OF (EVOF, $V_{\rm EVOF} > 700$ km s^{-1}) objects with a composite nuclear source: starbursts + AGN/QSOs; for example, in Mrk 231, IRAS 19254−7245, 01003−2230, 13218+0552, 11119+3257, 14394+5332, and others (Lípari et al. 2003);

(ii) high-resolution *HST* WFPC2 images of IR + BAL + Fe II QSOs show in practically all of these objects arcs or shell features probably associated with galactic winds or merger processes (Lípari et al. 2003).

Our evolutionary model for young/composite IR QSOs suggests that part of the BAL systems and extreme Fe II emission could be

linked to violent supermassive starbursts (probably generated by mergers), which can lead to a large-scale expanding shell, often obscured by dust.

Therefore it is important to analyse different types of evidence for OF in IR QSOs. Recently, Zheng et al. (2002) reported a very interesting new result: they measured the offset between the broad and narrow Hβ and [O III] λ5007 emission-line components in a sample of 25 IR QSOs; and they found a clear offset in ~76 per cent of their sample. They associated this offset to OF processes. We note that previously Taniguchi et al. (1994) performed a similar study for the broad and narrow Paα emission line in the IR QSO IRAS 07598+6508; and they already suggested that this type of offset could be associated to OF events. We have verified that for Mrk 231 the results using the offset method (by Zheng et al. 2002) gave the same value of OF, –1000 km s^{-1}, as that already obtained from the detection of two emission-line systems in [O II] λ3727 (by Lípari et al. 1994). Therefore we followed this offset method (OSM) to study our OF IR QSO candidates.

We recall that this OSM requires two important steps: first, for objects with Fe II emission we need to subtract a Fe II template (using for example the Boroson & Green 1992 procedure). Then, a careful deblending of the broad and narrow emission-line components is required (using for example the detailed SPECFIT software package; for details see Zheng et al. 2002; Lípari et al. 2003, 2004a, and Section 2).

Table 8 presents the updated values of our data base of OF in IR QSOs, including 12 new values of OF obtained by using this offset method and applied to our OF IR QSO candidates (from Lípari et al. 2004a: table 1). Table 8 also includes the offset–OF values for 15 IR QSOs reported by Zheng et al. (2002). We selected objects with |offset–OF| > 200 km s^{-1}. In addition, a new column was included, with the values of the emission-line ratio of Fe II λ4570/Hβ (RF). We recall that this table presents the main properties of IR mergers/QSOs with galactic wind or candidates (including the results obtained for NGC 5514).

From Table 8 we note three interesting results:

(i) All the measured offsets – from objects with and without Fe II emission – show that the Hβ broad emission lines are blueshifted, in relation to the Hβ narrow component.

(ii) Plotting Fe II λ4570/Hβ versus offset–OF (Fig. 30), including our eight new objects with measured values of offset and Fe II emission, we confirm the trend found in this plot (already published by Zheng et al. 2002), in the sense that extreme OF velocities are detected only in strong and extreme Fe II emitters. Lípari et al. (1993) already defined strong and extreme Fe II emitters as objects with the ratio Fe II λ4570/Hβ > 1 and 2, respectively.

(iii) It is clear in this table that, as already noted by Taniguchi et al. (1994), in cold ULIRGs there is an absence of Fe II emission. Thus it is interesting to analyse if this fact means the absence of Type II SN or starbursts. In relation to this last point, Terlevich, Lípari & Sodre (in preparation) note that ULIRGs are very dusty objects with mainly LINER and Seyfert 2 spectra. However, when the broad-line region (BLR) is observed in ULIRGs, Fe II emission is also frequently observed.

The observation in all our OF IR QSO candidates that the Hβ broad-line component is blushifted in relation to the narrow one, is clearly consistent with the result obtained from the study of strong Fe II + BAL emitters, by Boroson & Meyer (1992). They proposed that blueshifted offset/asymmetry detected in the Hα broad components – of IR QSOs with strong Fe II + BAL systems – is probably due to the emission of the outflowing material, associated with the BAL process. Furthermore, our measurements are also consistent with the results of the study of multiple emission-line components, in some starburst nuclei of galaxies (Taniguchi 1987). Thus, a possible explanation for at least part of these blushifted broad-line systems in IR QSOs is the high-speed OF/GW generated in a burst of SN events near the nuclear region (Heckman et al. 1990; Perry & Dyson 1992; Terlevich et al. 1992; Lípari et al. 1994, 2003, 2004a; Taniguchi et al. 1994; Scoville & Norman 1996; Lawrence et al. 1997; Collin & Joly 2000; and others).

In relation to the clear trend found (or confirmed) in this paper, between the extreme offset–OF and Fe II emission, it is important to recall the following:

(i) We suggested that IR QSOs could be young IR-active galaxies at the end phase of an extreme starburst, i.e. composite and transition IR QSOs. At the final stage of an 'extreme starburst', i.e. Type II SN phase [(8–60) $\times 10^6$ yr from the initial burst; Terlevich et al. 1992, 1993] powerful galactic winds, giant galactic arcs, BAL systems and extreme Fe II emission can appear (see, for references, Lípari et al. 2004a).

(ii) In the shell or arc model proposed for Fe II + BAL + IR QSOs, the high fraction of IR QSOs showing properties of low-ionization BAL + Fe II systems (Low et al. 1989; Boroson & Meyer 1992; Lípari 1994) could be explained by the high fraction of arcs, shells and giant SN rings present in these IR systems (probably originated in the starburst Type II SN phase).

(iii) Recently, several studies have confirmed the 'composite nuclear nature' and the presence of merger features in several IR QSOs. In particular, using Keck spectroscopy, Canalizo & Stockton (2001) have studied mainly IR QSOs defined as transition/composite objects between ULIRGs and standard QSOs (Lípari 1994: fig. 5). They found clear spectroscopic evidence of strong young stellar populations, in the host galaxies of these systems. They also detected that, out of the nine transitional or composite IR QSOs studied, eight are major mergers.

(iv) Type II SNe are highly concentrated in space and time and arise from massive stars ($m \geqslant 8$ M$_\odot$) in young stellar clusters and associations (of tens or hundreds of massive stars; Heiles 1987). Thus, the presence of associations of Type II SN as a result of the evolution of massive stars should be expected (Hillebrand 1986; Woosley & Weaver 1986; Norman & Ikeuchi 1989). In particular, WR massive stars are progenitors of core-collapse SNe.

Theoretical and observational work suggests that Type II SNe are the main galactic objects capable of generating the blowout phase of the galactic winds (see, for references, Norman & Ikeuchi 1989).

It is important to note that the presence of *strong* Fe II emission requires 'very specific physical conditions', in the clouds of the broad and narrow line regions. In particular, Joly (1987) found, for the BLR, that a high Fe II/Hβ ratio could be explained mainly with purely collisional models showing low temperature ($T < 8000$ K), very high density ($N_e > 10^{11}$ cm^{-3}), and high column density ($N_H > 10^{22}$ cm^{-2}). For the narrow-line region, Verner et al. (2002, 2000) and Veron, Joly & Veron (2004) have shown that the presence of permitted (and forbidden) Fe II requires high or intermediate density ($10^6 < N_e < 10^8$ cm^{-3}) and intermediate ionization parameter ($10^{-6} < U < 10^{-5}$). Thus, these results suggest that the 'strong' Fe II emission could be detected in a relatively low percentage of objects or cases. However, it is very interesting to note that η Carinae, the nearest object with a strong OF, also has strong Fe II emission (see Gaviola 1953; Verner et al. 2002; Veron et al. 2004). More specifically, the core (0.3 arcsec) of η Carinae was resolved by

Table 8. IR mergers and IR QSOs/AGNs with low and high/extreme-velocity outflow.

Object	V_{OF1} km s^{-1}	V_{OF2} km s^{-1}	z	L_{FIR} log $L/L_{\odot}$	L_{IR}/L_B	Nuclear activity	Morph type	RF	OF type	OF reference
Low-velocity OF										
Arp 220	−450	–	0.01825	12.18	87	L+SB	PM	–	EL	Heckman (1987)
IRAS 00182−7112	−450	–	0.3270	12.90	(200)	L+SB	(M)	–	EL	Heckman et al. (1990)
IRAS 03250+1606	−431	–	0.129	12.06	–	L	M	–	AL	Rupke et al. (2002)
IRAS 03514+1546	−200	–	0.02100	11.10	–	SB	M	–	AL	Heckman et al. (2000)
IRAS 09039+0503	−656	–	0.125	12.07	–	L	M	–	AL	Rupke et al. (2002)
IRAS 11387+4116	−511	–	0.149	12.18	–	SB	OM	–	AL	”
IRAS 23128−5919	−300	–	0.04490	12.60	8	L+SB	M	–	EL	Lípari et al. (2003)
Mrk 266	−300	–	0.02900	11.37	8	SB	PM	–	EL	Wang et al. (1997)
Mrk 273	−600	–	0.03850	12.14	36	L+SB	PM	–	EL	Colina et al. (1999)
NGC 1614	−400	–	0.01550	11.61	18	L+SB	M	–	EL	Ulrich (1972)
NGC 2623	−405	–	0.01846	11.55	17	L+SB	M	–	EL	This paper
NGC 3256	−370	–	0.00940	11.57	9	SB	MM	–	EL	Lípari et al. (2000)
NGC 3690	−300	–	0.01025	11.91	23	SB	PM	–	EL	Heckman et al. (1990)
NGC 4039	−365	–	0.00560	10.99	6	L+SB	PM	–	EL	Lípari et al. (2003)
NGC 5514	−320	–	0.02453	10.70	1	L+SB	PM	–	EL	This programme
High/extreme OF										
IRAS 01003−2238	−770	−1520	0.1180	12.24	67	QSO+SB	OM	–	EL	Lípari et al. (2003)
IRAS 05024−1941	−1676	–	0.192	12.43	–	S2	M	–	AL	Rupke et al. (2002)
IRAS 05024−1941	−1150	−2127	0.192	12.43	–	S2	M	–	EL	This paper
IRAS 05189−2524	−849	–	0.042	12.07	–	S2	M	–	AL	Rupke et al. (2002)
IRAS 10378+1108	−1517	–	0.136	12.26	–	L	M	–	AL	”
IRAS 11119+3257	−1300	(−2120)	0.1873	12.58	–	S1+SB	M	–	EL	Lípari et al. (2003)
IRAS 13218+0552	−1800	(−3438)	0.2048	12.63	96	QSO+SB	OM	–	EL	”
IRAS 14394+5332	−880	(−1650)	0.1050	12.04	–	S2	MM	–	EL	”
IRAS 15130−1958	−780	(−1200)	0.1093	12.09	–	S2	M	–	EL	”
IRAS 15462−0450	−1000	(−1760)	0.1001	12.16	–	S1	M	–	EL	”
IRAS 19254−7245	−800	–	0.05970	12.04	30	QSO+SB	PM	–	EL	Colina et al. (1991)
Mrk 231	−1000	–	0.04220	12.53	32	QSO+SB	M	1.83	EL	Lípari et al. (1994)
Mrk 231	−1100	–	0.04220	12.53	32	QSO+SB	M	1.83	OSM	Zheng et al. (2002)
NGC 3079	−1600	–	0.00400	10.49	2	L+SB	Sp	–	EL	Heckman et al. (1990)
NGC 6240	−930	–	0.02425	11.83	15	L+SB	PM	–	EL	”
IR QSO offset-OF										
IRAS 00275−2859	−730	–	0.2792	12.64	9	QSO+SB	PM	1.47	OSM	Zheng et al. (2002)
IRAS 00509+1225	−1110	–	0.060	11.87	20	QSO+SB	PM	1.40	OSM	This paper
IRAS Z01373+0604	−1660	(−3100)	0.3964	12.30	3	QSO+SB	–	2.33	OSM	”
IRAS 02054+0835	−1355	–	0.345	12.97	–	QSO	–	2.42	OSM	Zheng et al (2002)
IRAS 02065+4705	−500	–	0.132	12.27	–	QSO	–	1.65	OSM	”
IRAS 04415+1215	−875	–	0.089	12.41		QSO	–	1.74	OSM	”
IRAS 04505−2958	−1700	–	0.2863	12.55	20	QSO+SB	PM	1.33	OSM	This paper
IRAS 06269−0543	−550	–	0.117	12.49	–	QSO	–	0.57	OSM	Zheng et al. (2002)
IRAS 07598+6508	−2030	–	0.1483	12.45	5	QSO+SB	M	2.75	OSM	”
IRAS 07598+6508	−1920	–	0.1483	12.45	5	QSO+SB	M	2.75	OSM	This paper
IRAS 09427+1929	−1640	–	0.284	12.61	–	QSO	–	2.98	OSM	Zheng et al. (2002)
IRAS 10026+4347	−650	–	0.178	12.20	–	QSO	–	2.07	OSM	”
IRAS 11119+3527	−950	–	0.189	12.64	–	QSO	M	1.12	OSM	”
IRAS Z11598−0112	−970	–	0.151	11.91	–	QSO	–	1.71	OSM	”
IRAS 13305−1739	−730	–	0.148	12.21	–	S2	OM	–	OSM	This paper
IRAS 13342+3932	−920	–	0.179	12.49	–	QSO	–	0.73	OSM	Zheng et al. (2002)
IRAS 13451+1232	−1210	–	0.122	12.28	–	S2	PM	–	OSM	This paper
IRAS 14026+4341	−1500	–	0.320	12.55	40	QSO	M	1.12	OSM	”
IRAS 15462−0450	−1110	–	0.101	12.35	–	QSO	M	1.32	OSM	Zheng et al. (2002)
IRAS 17002+5153	−1050	–	0.2923	12.58	5	QSO+SB	PM	1.56	OSM	This paper
IRAS 18508−7815	−1250	–	0.162	12.0	8	QSO	M	2.40	OSM	”
IRAS 20036−1547	−400	–	0.193	12.70	–	QSO	–	2.74	OSM	Zheng et al. (2002)
IRAS 20520−2329	−660	–	0.206	12.52	–	QSO	–	2.02	OSM	”
IRAS 21219−1757	−460	–	0.110	11.98	89	QSO	OM	1.82	OSM	This paper
IRAS 22419−6049	−390	–	0.1133	11.30	–	QSO+SB	M	–	OSM	”
IRAS 23389+0300	−1640	–	0.145	12.09	–	S2	PM	–	OSM	”

Notes. Cols. 2 and 3: OF values obtained from the references included in Col. 9. Values between parentheses are possible detections. [O III] MC indicates emission line [O III] λ5007 with multiple components.Col. 5: The L_{IR} were obtained for [8–1000 μm], using the relation given by Sanders & Mirabel (1996).Col. 7: The properties of the nuclear activity were obtained from Veilleux et al. (1999), Canalizo & Stockton (2001) and Lípari et al. (2003). S1: Seyfert 1, S2: Seyfert 2, L: Liners and SB: starburst.Col. 8: For the morphological or interaction type we used the classification criteria of Kim & Sanders (2002) and Sourace (1998); PM: pre-merger, M: merger, OM: old merger, MM: multiple merger, Sp: spirals.Col. 9: RF is the ratio of the emission line Fe II λ4570/HβCol. 10: EL, AL and OSM indicate the OF derived from emission and absorption lines, and the offset emission-line method (see the text), respectively.

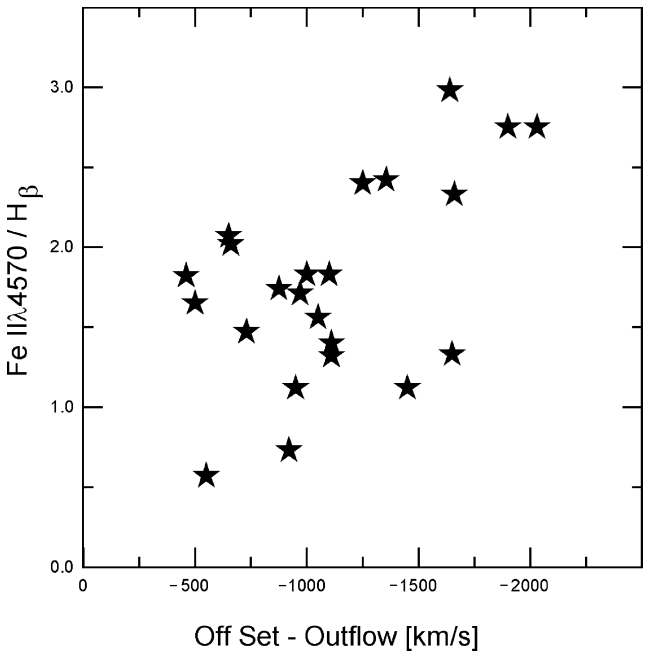

Figure 30. Plot of the ratio Fe II λ4570/Hβ versus offset of the Hβ broad and narrow emission-line components (probably associated with outflow; see the text). The data were obtained from Table 8, and for IR QSOs.

speckle interferometry into A, B, C and D components (Weigelt & Ebersberger 1986). *HST* observations found that the brightest component A is the central massive star + wind and the other objects (B, C and D) are slow-moving ejecta (Davidson et al. 1995, 1997; Gull, Ishibashi & Davidson 1999). The *HST*/STIS spectrum of source A is rich in broad permitted Fe II lines, with many P Cygni absorption components (Hillier et al. 2001). Narrow permitted and forbidden Fe II dominated in the B–D spectrum. The gaseous B, C and D blobs have low temperature $T_e \sim 6500$ K and relatively high density $N_e \sim 10^6$ cm^{-3}, in agreement with the results of the Fe II models.

In conclusion, the presence of starbursts + GWs/OFs + Type II SNe in IR QSOs could be a possible explanation for 'part' of the trend found in the plot of Fe II/Hβ versus offset–OF (Fig. 30). More specifically, this trend (in the sense that in IR QSOs extreme offset–OF velocities are detected only in strong and extreme Fe II emitters) could be explained by the fact that in IR QSOs a combination of the following three processes is at work: (1) large-scale giant ionizing OF-shocks; (2) association of massive stars that probably end their evolution as Type II SNe, and this process can enrich the ISM and the BLR with Fe; (3) obscured QSOs that gradually ionize part of the BLR (as suggested by the standard models of photoionization, by a supermasive black hole). Previously, we found clear evidence that extreme OF events are associated with these three 'main processes' (Lípari et al. 1994, 2003, 2004a).

Finally, we note that the results of the present 2D spectroscopic study of IR mergers and IR QSOs with galactic winds will be used in a second part of this programme, which is devoted to the study of galactic winds in Lyα emitters at high redshift. This study is based on a very deep imaging and spectroscopic survey for Lyα emitters at $z = 5.7$ using the Suprime-Cam and GMOS on the Subaru and Gemini telescopes (Ajiki et al. 2002, 2003; Taniguchi et al. 2003; Lípari et al. 2004b). This survey gave us a well-defined sample of 20 Lyα emitter (LAE) candidates at $z = 5.7$ and two of them were confirmed as LAEs at $z = 5.7$ (Ajiki et al. 2002; Taniguchi et al. 2003). Furthermore, Ajiki et al. (2002) found in the optical Keck II spectrum of J1044–0130 (at $z = 5.687$) the typical line profile of a galactic wind; thus this object is probably the more distant GW observed to date. Therefore, it will be interesting to compare the results of the present 2D spectroscopic/imaging study of galactic winds at low redshift (for NGC 2623, 5514, 3256, Mrk 231, Arp 220, and others) with those obtained from the imaging and 1D spectroscopic analysis of galactic winds at high redshift (when the galaxies and QSOs formed).

In part, this type of study and comparison has already started. For example, Hibbard & Vacca (1997) used rest-frame *B* and *V* images of nearby interacting/mergers and starburst galaxies (e.g. NGC 1614, 1741, 3690, He 2-10) to simulate *Hubble Deep Field* observations in F606W and F814W filters of starburst galaxies in the redshift range $z \sim 0.5$–2.5.

It is important to recall that the same problem of lack of spatial resolution in the analysis of galaxies/QSOs at high redshift is present in studies of the BLRs and supermassive black holes in galaxies/QSOs at low redshift. Therefore, it is interesting to answer a simple question: how will NGC 5514 look at redshift $z > 3$? (with two extranuclear regions with strong LINER activity). Probably, this merger could be detected mainly as a point source with multiple or broad emission-line systems, and properties of a transition LINER/H II object. These characteristics are attributed frequently to the nuclear region and the BLR.

5 SUMMARY AND CONCLUSIONS

In this paper a study of the morphology, kinematics and ionization structure of the IR merger NGC 5514 is presented. The study is based on 2D INTEGRAL spectroscopy (obtained on the 4.2-m WHT, at La Palma Observatory) and long-slit spectroscopy plus broad-band images (obtained on the CASLEO and CTIO 2.15-m and 1.0-m telescopes, respectively). The main results and conclusions may be summarized as follows:

(i) Clear evidence of two extranuclear starburst regions with young outflows and LINER activity are reported. One of these OFs generated a supergiant galactic bubble detected just in the rupture and pre-blowout phase and the other one is associated with an extended complex of giant H II regions.

(ii) For the galactic bubble: (1) the [S II], Hα, [N II], [O I] and [O III] emission-line maps show clearly a supergiant bubble with ellipsoidal shape, with major and minor axes of ~6.5 kpc (13.6 arcsec; at PA = 120° ± 10°) and ~4.5 kpc (9.6 arcsec); (2) the centre is located at 8.5 arcsec ~4.1 kpc to the west of the main nucleus; (3) there are four main knots, one very strong/extended and three more compact at the border; (4) the WHT spectra show two strong components, (blue and red emission-line systems), probably associated with the emission from the near and far side of the external shell of the bubble; (5) these two components depict LINER properties, probably associated with large-scale OF + shocks; (6) at the east border, the kinematics and the [S II] emission-line maps show a strong and extended ejection of ionized gas, aligned with the PA of the major axis; (7) another three ejections from the bubble were found; two of them are perpendicular to the extended one. These results strongly suggest that the GW/OF process is in the rupture of the bubble and in the beginning of the blowout phase.

(iii) In knots (of the bubble) 1, 2a, 2b, 3a and 3b Wolf–Rayet features/bump at λ4560 were detected. In addition, the [N I] λ5199 emission line was also found only in these knots (where we detected

the WR bump). Similar behaviour, i.e. strong WR and [N I] emission, was observed in the spectra of the prototype WR galaxy, NGC 6754.

(iv) For the extended complex of giant H II regions: (1) the Hα, [N II] λ6583 and [S II] $\lambda\lambda$6717 + 31 emission-line maps show a compact strong emission-line area (with a peak of emission located at 1.7 arcsec ~810 pc to the east of the second nucleus), and a faint extended emission with elongated shape, major and minor axes of ~5.1 kpc (10.8 arcsec; at PA ~ 20°) and ~2.9 kpc (6.0 arcsec); (2) inside this complex, the spectra show H II region and H II/LINER characteristics; (3) however at the border of this extended area the spectra have outflow components and LINER properties (similar to those observed in the OF of the galactic bubble).

(v) INTEGRAL 2D [N II], Hα, [S II] and [O III] velocity fields (VFs) for the main body of the merger are presented (mosaics covering the area ~30 × 20 arcsec^2; 14.3 × 9.5 kpc^2). These VF maps show results consistent with an expansion of the bubble, plus several strong and weak ejections.

(vi) The U, B, V, J, H and K_S images show a pre-merger morphology, from which faint filaments (~2.8 kpc) of emission emerge from the bubble position.

(vii) The ionization structure and the physical conditions were analysed, using 2D emission-line ratios and width maps: [S II]/Hα, [N II]/Hα, [O I]/Hα, [O III]/Hβ and FWHM–[N II]. In the region of the bubble, 100 per cent of the field shows very high [N II]/Hα and [S II]/Hα (>0.8).

Thus the properties observed in these two extranuclear regions of NGC 5514 are consistent with two 'early' galactic wind processes, which are powered mainly by two starbursts (probably generated in the ongoing merger process). These new results for NGC 5514 confirm our previous proposition that extreme nuclear and extranuclear galactic wind processes are important events in the evolution of IR mergers and IR QSOs.

Finally, the updated values of our data base of OF in IR QSOs/mergers were presented, including 12 new values of OF obtained by using an offset method (for the narrow and broad Hβ emission line), applied to our OF IR QSO candidates. In addition, in this data base were included the offset–OF values for 15 IR QSOs reported by Zheng et al. (2002). All the measured offsets show that the broad emission lines are blueshifted, in relation to the narrow component of the same emission line. Plotting Fe II λ4570/Hβ versus offset–OF we confirm the trend previously found in this plot (Zheng et al. 2002), in the sense that extreme OF velocities are detected only in strong and extreme Fe II emitters. This trend could be explained by the fact that a combination of the following three processes is probably working in IR QSOs: (1) large-scale giant ionizing OF–shocks; (2) association of massive stars that probably end their evolution as Type II SNe, and this process can enrich the ISM and the BLR with Fe; (3) obscured QSOs that gradually ionize part of the BLR (as suggested by the standard models of photoionization, by a supermasive black hole). Previously, we found clear evidence that extreme OF events are associated with these three 'main processes'.

ACKNOWLEDGMENTS

The authors thank M. Ajiki, J. J. Claria, J. C. Forte, L. Hernquist, J. Laborde, B. Madore, T. Mahoney, X. Y. Xia, W. Zheng, for useful discussions and assistance. We also wish to thank T. Boroson, R. Green, D. Kim, D. Macchetto, D. Sanders, S. Veilleux, M. Veron, and B. Wilkes for their spectra of IR QSOs, kindly made available to us. This paper is based on observations obtained at the William Herschel Telescope (Canary Island of La Palma, Spain), CASLEO (San Juan, Argentina) and CTIO (La Serena, Chile) with the 4.2-m, 2.15-m and 1.0-m telescopes. The 4.2-m WHT is operated by the Isaac Newton Group at the Observatorio de Roque de los Muchachos of the Instituto de Astrofísica de Canarias (IAC). The authors thank all the staff at the Observatories and the Instituto for their kind support (SL and RD also thank the IAC for financial support). This research was made using the NASA Extragalactic Data Base, NED, which is operated by the Jet Propulsion Laboratory, California Institute of Technology, under contract with NASA. This paper was supported in part by grants from CONICET, SeCyT-UNC, and Fundación Antorchas (Argentina). Finally, we wish to thank the referee for constructive and valuable comments.

REFERENCES

Ajiki M. et al., 2002, ApJ, 576, L25
Ajiki M. et al., 2003, AJ, 126, 2091
Akima H., 1978, Trans. Math. Software (ACM), 4, 148
Alton P., Davies J., Bianchi S., 1999, A&A, 343, 51
Armus L., Heckman T. M., Miley G., 1988, ApJ, 326, L45
Arribas S. et al., 1998, Proc. SPIE, 3355, 821
Axon D., Taylor K., 1978, Nat, 274, 37
Barnes J., 1989, Nat, 338, 123
Barnes J., Hernquist L., 1992, ARA&A, 30, 705
Barnes J., Hernquist L., 1996, ApJ, 471, 115
Barth A., Shields J., 2000, PASP, 112, 753
Bernlohr K., 1993, A&A, 268, 25
Bevington P., 1969, Data Reduction and Error Analysis for the Physical Sciences. McGraw-Hill, New York
Bingham R., Gellatly D., Jenkins C., Vorswick S., 1994, Proc. SPIE, 2198, 56
Binette L., 1985, A&A, 143, 334
Binney J., Tremaine S., 1987, Galactic Dynamics. Princeton Univ. Press, Princeton, NJ
Bland J., Tully R., 1988, Nat, 334, 43
Bland J., Taylor K., Atherton P., 1987, MNRAS, 228, 591
Boroson T., Green R., 1992, ApJS, 80, 109
Boroson T., Meyer K., 1992, ApJ, 397, 492
Canalizo G., Stockton A., 2001, ApJ, 555, 719
Canto J., 1984, in Peimbert M., ed., Temas Selectos en Astrofisica. UNAM, Mexico, p. 115
Castor R., McCray R., Weaver R., 1975, ApJ, 200, L107
Cecil G., Bland-Hawthorn J., Veilleux S., Filippenko A., 2001, ApJ, 555, 338
Chevalier R., Clegg A., 1985, Nat, 317, 44
Clements D., Sutherland W., Saunders W., Efstathiou G., McMahon R., Maddox S., Lawrence A., Rowan-Robinson M., 1996, MNRAS, 279, 459
Colina L., Lípari S. L., Macchetto F., 1991, ApJ, 379, 113
Colina L., Arribas S., Borne K. D., 1999, ApJ, 527, L13
Collin S., Joly M., 2000, New Astron. Rev., 44, 531
Condon J., Cotton W., Greiser, E., Yin Q., Perley R., Taylor G., Broderick J., 1998, AJ, 115, 1693
Condon J., Cotton W., Broderick J., 2002, AJ, 124, 675
Conti P. S., 1991, ApJ, 377, 115
Davidson K., Ebberts D., Weigelt G., Humphreys R., Hajioan A. Walborn N., Rosa M., 1995, AJ, 109, 1784
Davidson K., Ebbets D., Johansson S., Morse J., Hamann F., 1997, AJ, 113, 335
de Grijp M., Miley G., Lub J., Jong T., 1987, A&AS, 70, 95
Dopita M., 1994, in Bicknell G., Dopita M., Quin P., eds, ASP Conf. Ser. Vol. 54, The Physics of Active Galaxies. Astron. Soc. Pac., San Francisco, p. 287
Dopita M., Sutherland R., 1995, ApJ, 455, 468
Duric M., Seaquist E., 1988, ApJ, 326, 574
Efremov Y. et al., 2002, A&A, 389, 855
Fabbiano G., 1988, ApJ, 330, 672

Fehmers G., de Grijp M., Miley G., Keel W., 1994, A&AS, 108, 61
Feinstein C., Vega I., Mendez M., Forte J. C., 1990, A&A, 239, 90
Filippenko A., 1996, in Eracleous M., Koratkar A., Ho L., Leitherer C., eds, ASP Conf. Ser. Vol. 103, The Physics of LINERS in View of Recent Observations. Astron. Soc. Pac., San Francisco, p. 17
Filippenko A., Sargent W., 1992, AJ, 103, 28
Filippenko A., Terlevich R., 1992, ApJ, 397, L29
Fried J., Lutz D., 1988, A&A, 197, 52 (FL88)
Ford H., Dahari O., Jacobi G, Crane P., Giardullo R., 1986, ApJ, 311, L7
Garcia-Burillo S., Martin-Pintado J., Fuente A., Neri R., 2001, ApJ, 563, L27
Garcia-Lorenzo B., Acosta-Pulido J., Mejias-Fernandez E., 2002, in Rosado M., Binette L., Arias L., eds, ASP Conf. Ser. Vol. 282, Galaxies: The Third Dimension. Astron. Soc. Pac., San Francisco, p. 501
Gaviola E., 1953, ApJ, 118, 234
Guerrero M., Manchado A., 1998, ApJ, 508, 262
Gull T., Ishibashi K., Davidson K., 1999, in Morse J., Humphreys R., Damineli A. M., eds, ASP Conf. Ser. Vol. 179, Eta Carinae at the Millennium. Astron. Soc. Pac., San Francisco, p. 144
Heckman T. M., 1980, A&A, 87, 152
Heckman T. M., 1987, in Khachikian E. Ye., Fricke K., Melnick J., eds, Observational Evidence of Activity in Galaxies. Reidel, Dordrecht, p. 421
Heckman T. M., 1996, in Eracleous M., Koratkar A., Leitherer C., Ho L., eds, ASP Conf. Ser. Vol. 103, The Physics of LINERs in View of Recent Observations. Astron. Soc. Pac., San Francisco, p. 241
Heckman T. M., Armus L., Miley G., 1987, AJ, 93, 276
Heckman T. M., Armus L., Miley G., 1990, ApJS, 74, 833
Heckman T. M., Dahalem M., Eales S., Fabbiano G., Weaver K., 1996, ApJ, 457, 616
Heckman T. M., Lehnert M., Strickland D., Armus L., 2000, ApJS, 129, 493
Heiles C., 1987, ApJ, 315, 555
Hernquist L., 1993, ApJ, 409, 548
Hernquist L., Mihos C., 1995, ApJ, 448, 41
Hibbard J. E., Vacca W., 1997, AJ, 114, 1741
Hillebrand R., 1986, Highlights of Astronomy, Vol. 17. Reidel, Dordrecht, p. 589
Hillier D. J., Davidson K., Ishibashi K., Gull T., 2001, ApJ, 553, 837
Ho L., 1996, in Eracleous M., Koratkar A., Ho L., Leitherer C., eds, ASP Conf. Ser. Vol. 103, The Physics of LINERS in View of Recent Observations. Astron. Soc. Pac., San Francisco, p. 255
Ho L., Filippenko A., Sargent W., 1993, ApJ, 417, 63
Ho L., Filippenko A., Sargent W., 1997, ApJS, 112, 315
Hodge P. W., 1967, PASP, 79, 29
Hodge P. W., Kennicutt R., 1983, ApJ, 268, L75
Howard S., Keel W., Byrd G., Burkey J., 1993, ApJ, 417, 502
Hummel E., van Gorkom J., Kotanyi C., 1983, ApJ, 267, L5
Hunter D., Gillett F., Gallagher J., Rice W., Low F., 1986, ApJ, 303, 171
Jarret T., Chester T., Cutri R., Schneider S., Skrutskie M., Huchra J., 2000, AJ, 119, 2498
Jogee S., Kenney J., Smith B., 1998, ApJ, 494, L185
Joly M., 1987, A&A, 184, 33
Joseph R. D., Wright G., 1985, MNRAS, 214, 87
Kawakatu N., Umemura M., Mori M., 2003, ApJ, 583, 85
Kennicutt R., Keel W., Blaha X., 1989, AJ, 97, 1022
Kim D., Sanders D., 2002, ApJS, 119, 41
Koo B., McKee C., 1992, ApJ, 388, 93
Kormendy J., Richstone D., 1995, ARA&A, 33, 581
Kormendy J., Sanders D., 1992, ApJ, 390, L53
Landolt A., 1992, AJ, 104, 340
Laor A., 1998, ApJ, 505, L83
Larsen S., Efremov Y., Elmegreen B., Alfaro E., Battinelli P., Hodge P., Richtler T., 2002, ApJ, 567, 896
Lawrence A., Elvis M., Wilkes B., McHardy I., Brandt N., 1997, MNRAS, 285, 879
Lehnert M., Heckman T. M., 1995, ApJS, 97, 89
Lehnert M., Heckman T. M., 1996, ApJ, 462, 651
Lípari S. L., 1994, ApJ, 436, 102
Lípari S. L., Macchetto F., 1992a, ApJ, 387, 522
Lípari S. L., Macchetto F., 1992b, ApJ, 397, 126
Lípari S. L., Macchetto F., Golombeck D., 1991a, ApJ, 366, L65
Lípari S. L., Bonatto Ch., Pastoriza M., 1991b, MNRAS, 253, 19
Lípari S. L., Terlevich R., Macchetto F., 1993, ApJ, 406, 451
Lípari S. L., Colina L., Macchetto F., 1994, ApJ, 427, 174
Lípari S., Tsvetanov Z., Macchetto F., 1997, ApJS, 111, 369
Lípari S. L., Diaz R., Taniguchi Y., Terlevich R., Dottori H., Carranza G., 2000, AJ, 120, 645
Lípari S. L., Terlevich R., Diaz R., Taniguchi Y., Zheng W., Tsvetanov Z., Carranza G., Dottori H., 2003, MNRAS, 340, 289
Lípari S. L., Mediavilla E., Diaz R., Garcia-Lorenzo B., Acosta-Pulido J., Agüero M., Terlevich R., 2004a, MNRAS, 348, 369
Lípari S. L. et al., 2004b, in Storchi Bergmann T., Ho L., Schmitt H., eds, Proc. IAU Symp. 222, ASP Conf. Ser., The Interplay among Black Hole Stars and IGM in Galactic Nuclei, p. 529
Lípari S. L. et al., 2004c, MNRAS, 354, L1
Lopez J., Meaburn J., Bryce M., Holloway A., 1998, ApJ, 493, 803
Low F., Cutri R., Kleinmann S., Huchra J., 1989, ApJ, 340, L1
Lutz D., 1990, PhD thesis, Univ. of Heidelberg
Lutz D., Veilleux S., Genzel R., 1999, ApJ, 517, L13
Lynds C., Sandage A., 1963, ApJ, 137, 1005
McCarthy P., Heckman T., van Breugel W., 1987, AJ, 93, 264
Mac Low M., McCray R., Norman M., 1989, ApJ, 337, 141
Manchado A., Stanghellini L., Guerrero M., 1996, ApJ, 466, L95
Masegosa J., Moles M., del Olmo A., 1991, A&A, 244, 279
Meaburn J., 1980, MNRAS, 192, 365
Melnick J., Mirabel I. F., 1990, A&A, 231, L19
Mendes de Olivera C., Plana H., Asram P., Bolte M., Bolesteix J., 1998, ApJ, 507, 691
Merrit D., Ferrarese L., 2001, MNRAS, 320, L30
Mihos C., Hernquist L., 1994a, ApJ, 431, L9
Mihos C., Hernquist L., 1994b, ApJ, 425, L13
Mihos C., Hernquist L., 1996, ApJ, 464, 641
Morganti R., Oosterloo T., Emonts B., van der Hulst J., Tadhunter C., 2003, ApJ, 593, L69
Moshier M. et al., 1992, Explanatory Supplement to the Faint *IRAS* Source Survey, Version 2. Jet Propulsion Laboratory, Pasadena
Mould J., Akeson R., Bothun G., Han M., Huchra J., Roth J., Schommer B., 1993, ApJ, 409, 14
Mould J., Martin S., Bothun G., Huchra J., Schommer B., 1995, ApJS, 96, 1
Murphy T., Soifer B., Matthews K., Armus L., 2001, ApJ, 559, 201
Murray N., Chiang J., Grossman S., Voit G., 1996, ApJ, 464, 641
Muthu C., Anandarao B., 2001, AJ, 121, 2106
Norman C., Ikeuchi S., 1989, ApJ, 395, 372
Oke J., 1990, AJ, 99, 1621
Oosterloo T., Morganti R., Tzioumis A., Reynold J., Kin E., McCullogh P., Tsvetanof Z., 2000, AJ, 119, 2085
Osterbrock D., Cohen R., 1982, ApJ, 261, 64
Perry J., Dyson R., 1992, in Holt S., Neff S., Urry M., eds, Testing the AGN Paradigm. Am. Inst. Phys., New York, p. 553
Plana H., Boulesteix J., 1996, A&A, 307, 391
Redman M., Al-Mostafa Z., Meaburn J., Bryce M., 2003, MNRAS, 344, 741
Richichi A., Paresce F., 2003, The Messenger (ESO), 114, 26
Rieke G., Lebofsky M., Thompson R., Low F., Tokunaga A., 1980, ApJ, 238, 24
Rieke G., Cutri R., Black J., Kailey W., McAlary C., Lebofsky M., Elston R., 1985, ApJ, 290, 116
Rupke D., Veilleux S., Sanders D., 2002, ApJ, 570, 588
Sanders D. B., Mirabel F., 1996, ARA&A, 34, 749
Sanders D. B., Soifer B. T., Elias J. H., Madore B. F., Matthews K., Neugebauer G., Scoville N. Z., 1988a, ApJ, 325, 74
Sanders D. B., Soifer B. T., Elias J. H., Neugebauer G., Matthews K., 1988b, ApJ, 328, L35
Sanders D. B., Scoville N., Soifer B. T., 1991, ApJ, 370, 158
Schaerer D., Contini T., Pindao M. 1999, A&AS, 136, 35

Scoville N. Z., Soifer B. T., 1991, in Leitherer C., Walborn N., Heckman T.M., Norman C., eds, Massive Stars in Starbursts. Cambridge Univ. Press, Cambridge, p. 233
Scoville N., Norman C., 1996, ApJ, 451, 510
Scoville N., Sargent A., Sanders D.B., Soifer B., 1991, ApJ, 366, L5
Seaquist E., Clark J., 2001, ApJ, 552, 133
Shields J., 1992, ApJ, 399, L27
Shull J., McKee C., 1979, ApJ, 227, 131
Soifer B. et al., 1984, ApJ, 278, L71
Stone R., Baldwin J., 1983, MNRAS, 204, 357
Strickland D., Stevens I., 2000, MNRAS, 314, 511
Suchkov A., Balsara D., Heckman T., Leitherer C., 1994, ApJ, 430, 511
Surace J., 1998, PhD thesis, Univ. of Hawaii
Surace J., Sanders D., Vacca W., Veilleux S., Mazzarela J., 1998, ApJ, 492, 116
Taniguchi Y., 1987, ApJ, 317, L57
Taniguchi Y., Shioya K., 2000, ApJ, 532, L12
Taniguchi Y., Shioya K., 2001, ApJ, 547, 146
Taniguchi Y., Wada K., 1996, ApJ, 469, 581
Taniguchi Y., Kawara K., Murayama T., Sato Y., 1994, AJ, 107, 1668
Taniguchi Y. et al., 2003, ApJ, 585, L97
Terlevich R., Melnick J., 1985, MNRAS, 213, 841
Terlevich R., Melnick J., Masegosa J., Moles M., Copetti M., 1991, A&AS, 91, 285
Terlevich R., Tenorio-Tagle G., Franco J., Melnick J., 1992, MNRAS, 255, 713
Terlevich R., Tenorio-Tagle G., Franco J., Boyle B., Rozyczka M., Melnick J., 1993, in Rocca-Volmerange B., Dennefeld M., Guiderdoni B., Tran Thanh Van, eds, First Light in the Universe: Stars or QSOs. Editions Frontières, Gif-sur-Yvette, p. 261
Toomre A., 1977, in Tinsley B., Larson R., eds, The Evolution of Galaxies and Stellar Population. Yale Univ. Observatory, New Haven, p. 401
Tomisaka K., Ikeuchi S., 1988, ApJ, 330, 695
Ulrich M., 1972, ApJ, 178, 113
Vader J. P., Chaboyer B., 1995, ApJ, 445, 691
Veilleux S., Osterbrock D.E., 1987, ApJS, 63, 295
Veilleux S., Bland-Hawthorn J., Tully R., Filippenko A., Sargent W., 1994, ApJ, 433, 48
Veilleux S., Kim D., Sanders D., 1999, ApJ, 522, 113
Veilleux S., Cecil G., Bland–Hawthorn J., Shopell P., 2002a, in Henney W., Steffe W., Raga A., Binette L., eds, Rev. Mex. Astron. Astrofis. Serie Conf. Vol. 13, Emission Lines from Jet Flows. UNAM, Mexico, p. 222
Veilleux S., Kim D., Sanders D., 2002b, ApJS, 143, 315
Verner E., Verner D., Baldwin J., Ferland G., Martin P., 2000, ApJ, 543, 831
Verner E., Gull T., Bruhweiler F., Johansson S., Ishiovashi K., Davidson K., 2002, ApJ, 581, 1154
Veron M., Joly M., Veron P., 2004, A&A, 417, 515
Wang J., Heckman T., Weaver K., Armus L., 1997, ApJ, 474, 659
Weigelt G., Ebersberger J., 1986, A&A, 163, L5
Wills K., Redman M., Muxlow W., Pedlar A., 1999, MNRAS, 309, 395
Woosley S., Weaver T., 1986, ARA&A, 24, 205
Zheng X., Xia X., Mao S., Deng Z., 2002, AJ, 124, 18

This paper has been typeset from a TEX/LATEX file prepared by the author.